

Thermal Physics of Asteroids

Charles University of Prague – Oct/Nov 2011

Marco Delbo

UNS-CNRS-Observatoire de la Côte d'Azur

Visiting: Astronomical Institute of the Charles University, Prague, CZ

October 26, 2011

Introduction

- ▶ Physics of **asteroids** and other small bodies.
- ▶ Thermal Physics of asteroids
 - ▶ How to determine, calculate/model, and use **temperatures** at the **surface** of asteroids
 - ▶ Why ?
 - ▶ How to model, and use **temperatures** in the **subsurface** of asteroids
 - ▶ Why ?

Outline

Introduction

Relevant physical parameters and their effects on temperatures

Models of temperature distribution and thermal emission

Application of thermal models: observations, surveys and results

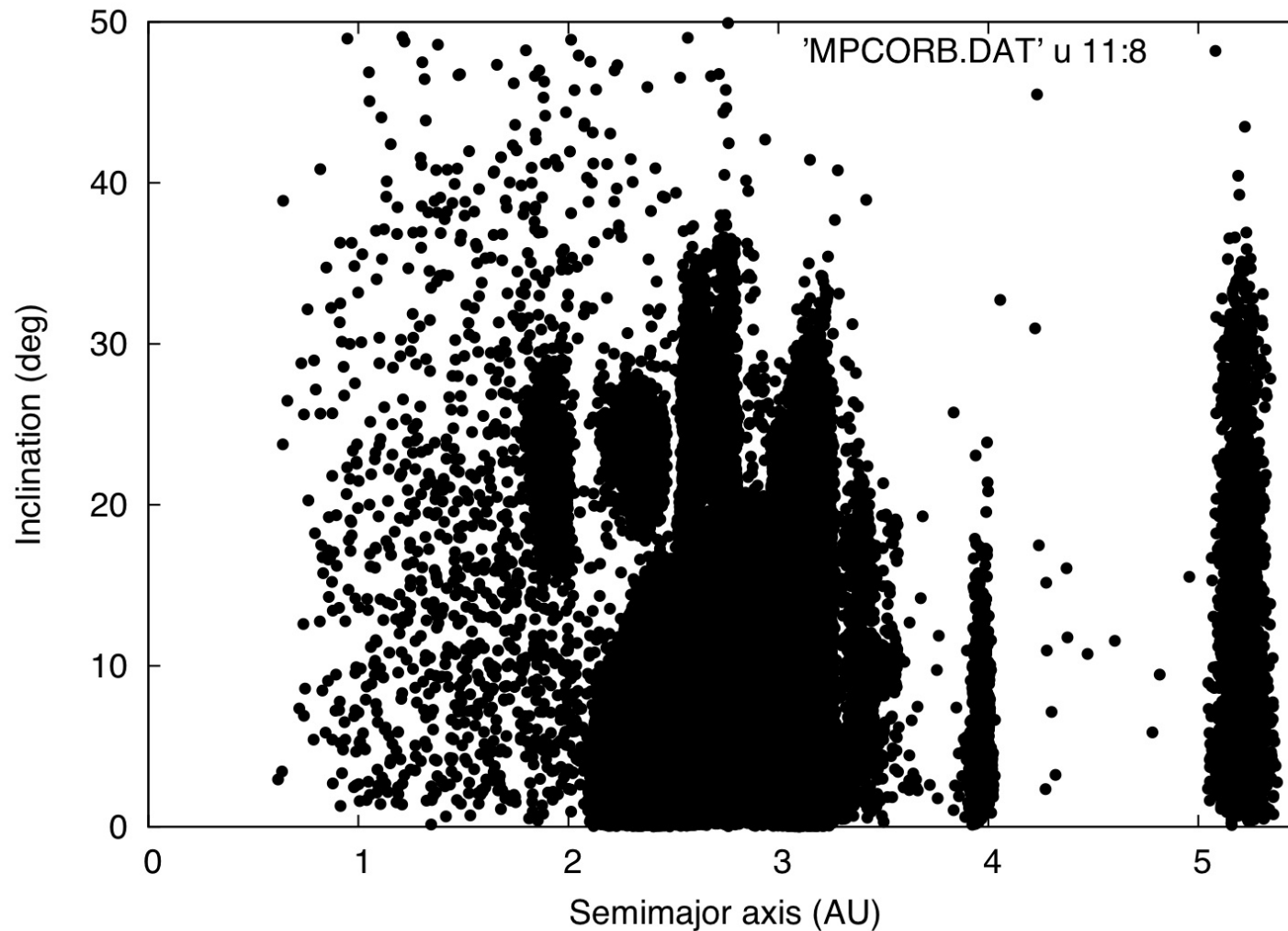
Cool problems and applications of everything

Why we study asteroids

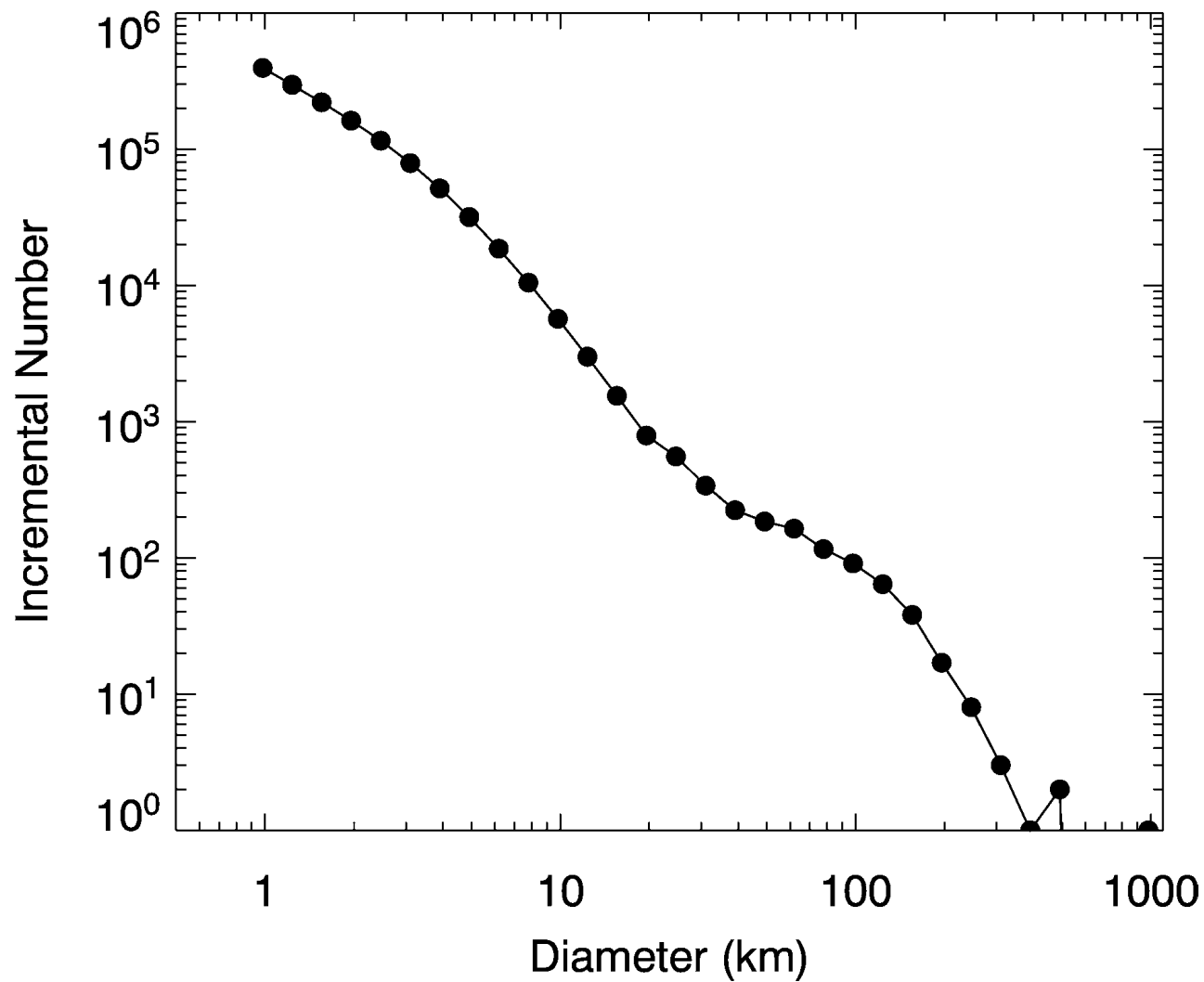
- ▶ remnant debris from the inner solar system formation process;
 - ▶ sources of most meteorites; many of these meteorites have already been subjected to detailed chemical and physical analyses.
but meteorites are like dead letter with no sender... if we can find to which asteroid(s) they come from...
- ▶ can collide with the Earth:
 - ▶ impact hazard
 - ▶ having significantly modified the Earth's biosphere in the past.
 - ▶ carbon-based molecules and volatile materials that served as the building blocks of life may have been brought to the Earth via asteroid and comet impacts
 - ▶ water may have been brought to Earth by asteroids and comets (?)

Where are the asteroids?

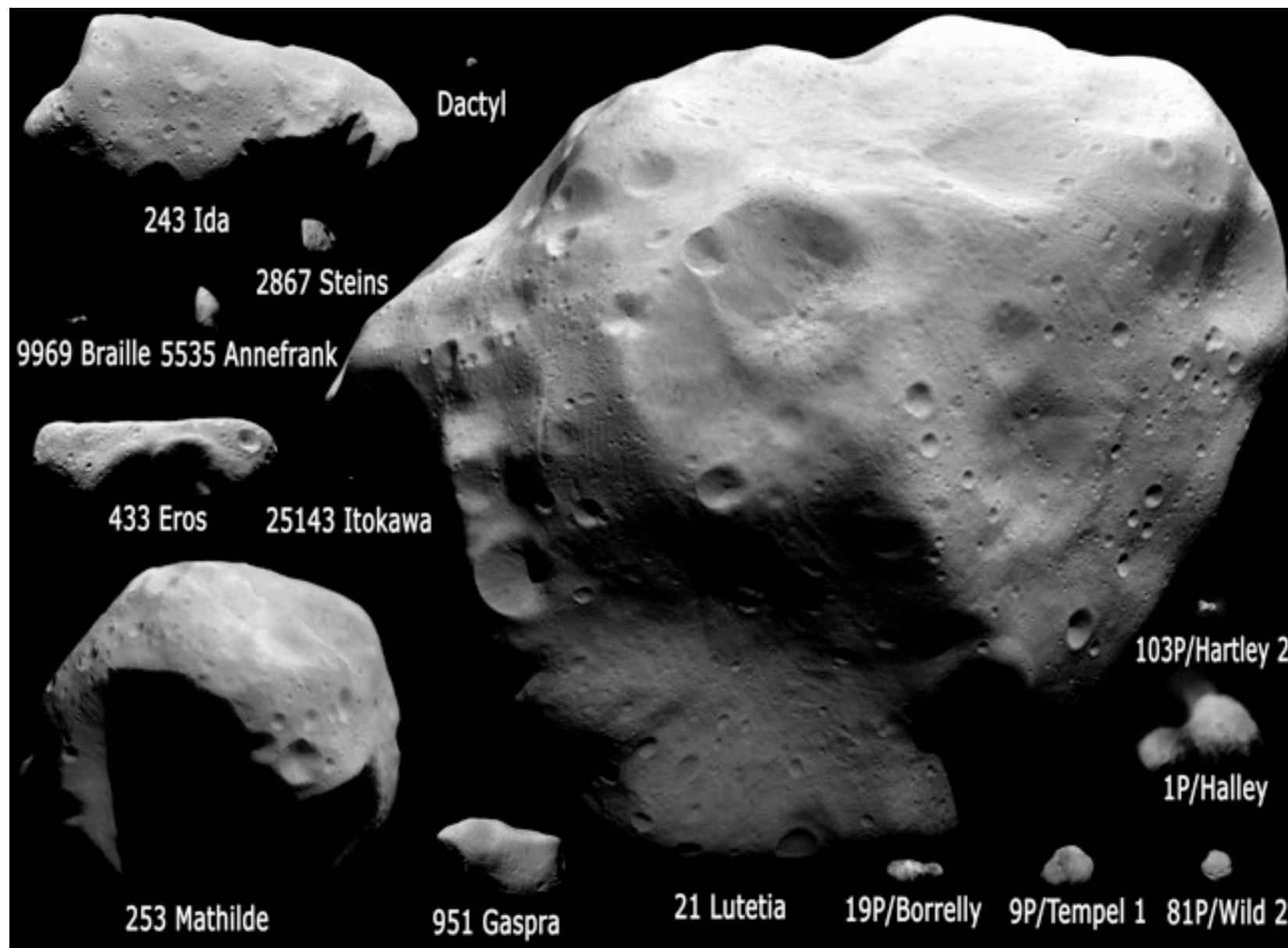
All numbered asteroids with $0 < a < 5.5 \text{ AU}$. Sept 2011

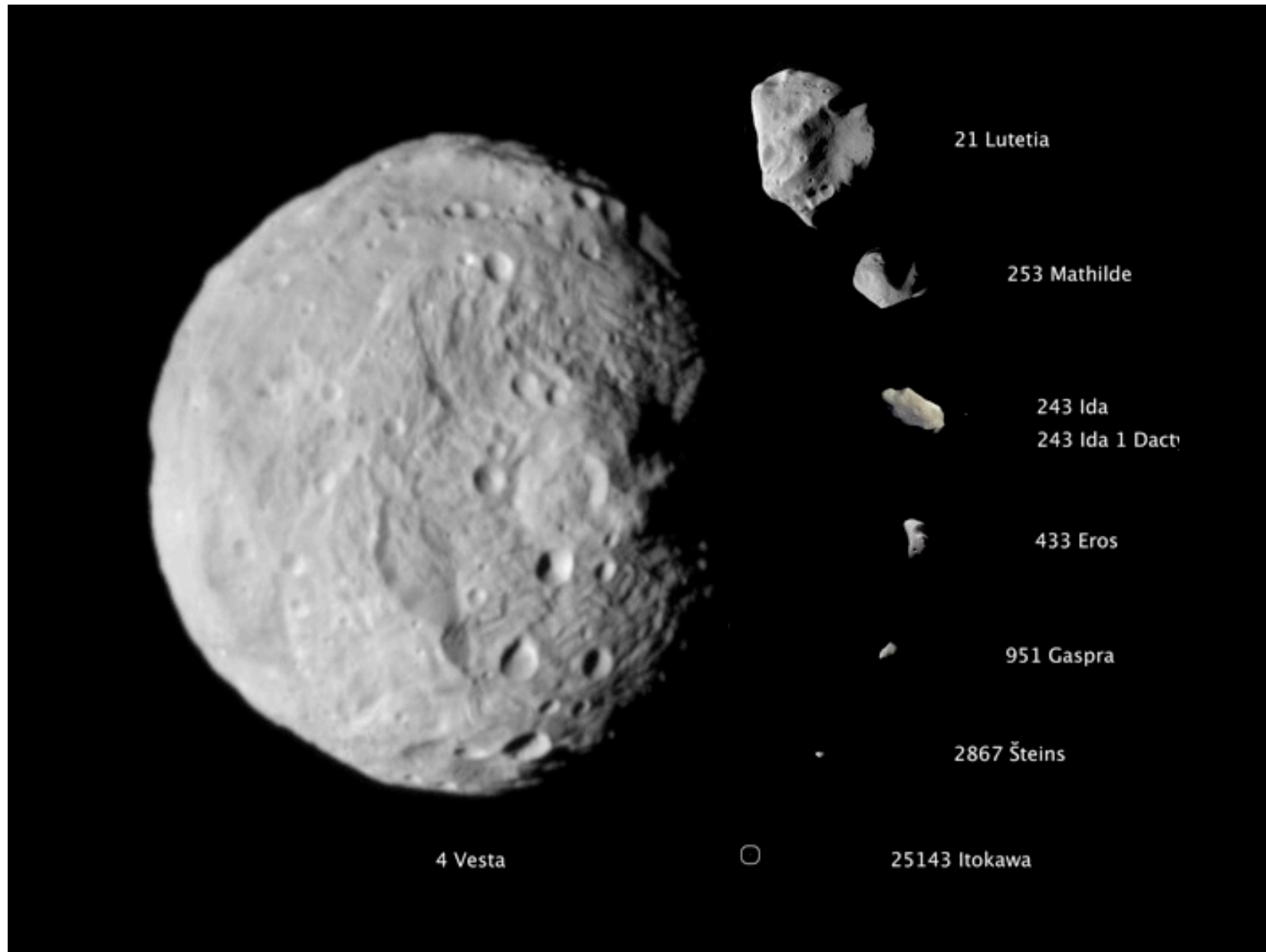


Size frequency distribution of asteroids



[BDN⁺05]







Physical Properties

- ▶ Size (Diameter, D)
 - ▶ Spherical Equivalent Diameter (D_s)
- ▶ Absolute Magnitude (H)

The magnitude of an asteroid extrapolated to $r = \Delta = 1$ AU and to phase angle (α) of zero.

- ▶ Albedo (Surface reflectivity)
 - ▶ Geometric Albedo (p)
$$p = \frac{I(\alpha=0)}{I_L(\alpha=0)}$$
 where I_L = brightness of an idealized flat, fully reflecting, diffusively scattering (Lambertian) disk with the same cross-section of the asteroid. [This is one method for measuring how closely the surface resembles a diffuse scattering surface.](#)
 - ▶ in the visible (p_V); R-band (p_R); etc etc..
 - ▶ in the near IR (p_{NIR})
 - ▶ Bolometric Bond's Albedo (A)























It is the fraction of power in the total electromagnetic radiation incident on an astronomical body that is scattered back out into space. It takes into account all wavelengths at all phase angles.
 - ▶ Photometric phase integral ($q = \frac{A}{p}$)
$$q = 2 \int_0^\pi \frac{I_\alpha}{I_0} \sin \alpha d\alpha$$

Link Diameter-Albedo-Absolute magnitude

$$D(km) = \frac{1329}{\sqrt{p_V}} 10^{-\frac{H}{5}} \quad (1)$$

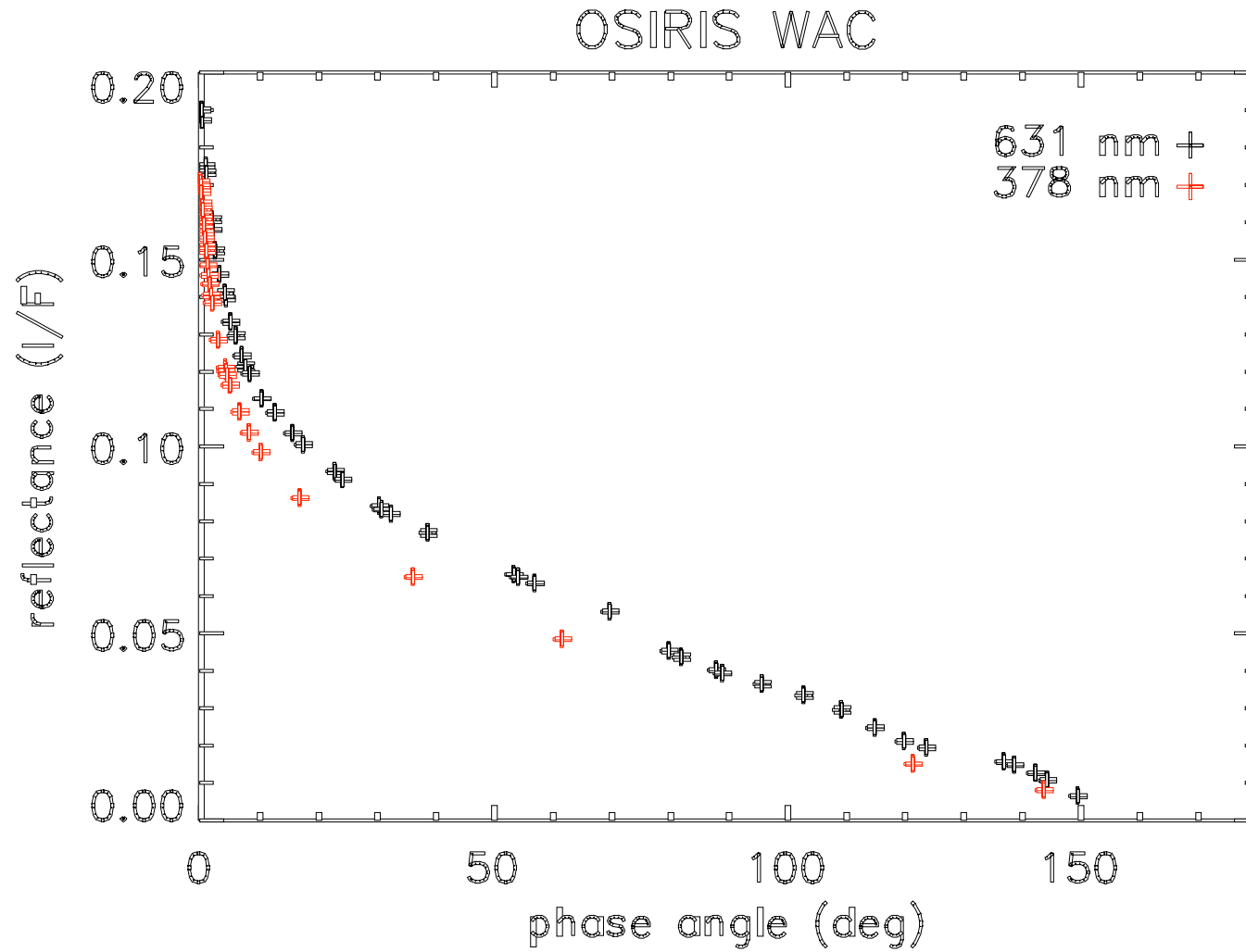
[DH02]

Geometric and Bond's albedo values of bodies

Name	Bond albedo	Visual geometric albedo
Mercury	0.119 	0.138 
Venus ^[2]	0.90 	0.67 
Earth ^[3]	0.306 	0.367 
Moon	0.123 	0.113 
Mars ^[4]	0.25 	0.15 
Jupiter ^[5]	0.343 	0.52 
Saturn ^[6]	0.342 	0.47 
Enceladus ^[7]	0.99 	1.4 
Uranus ^[8]	0.300 	0.51 
Neptune ^[9]	0.290 	0.41 
Pluto	0.4 	0.44–0.61 

http://en.wikipedia.org/wiki/Bond_albedo 18-Oct-2011

Phase integral of (21) Lutetia from OSIRIS

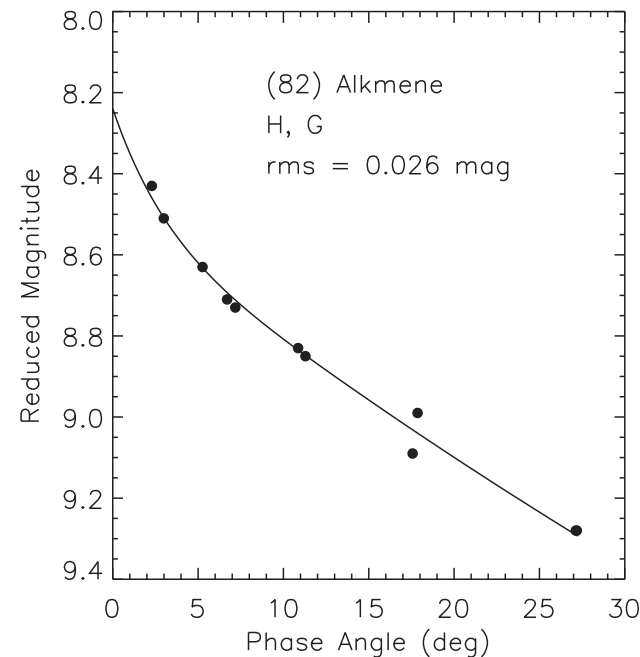
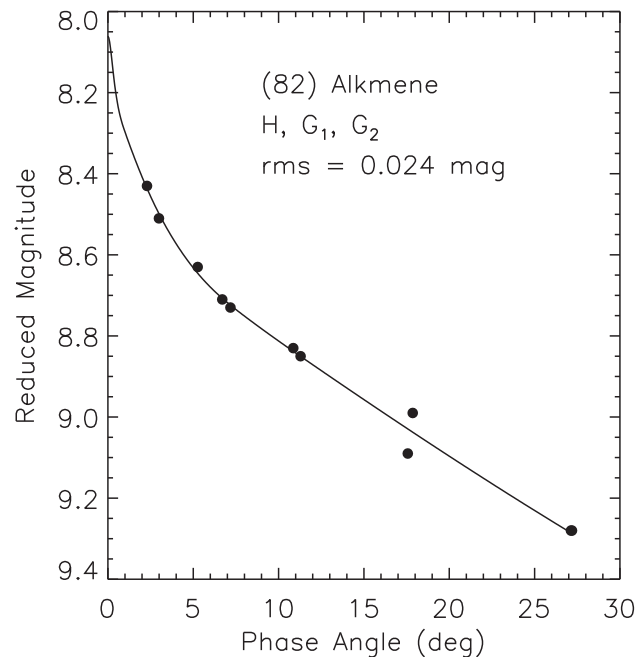


Caveats

The parameters above are well defined for spherical bodies with properties homogeneous all over their surfaces.

- ▶ the H magnitude is function of the aspect and rotational phase for an irregularly-shaped body

Extrapolation of measurements (photometry) to zero degree of phase angle can be source of error and model dependent.



[MBC⁺10]

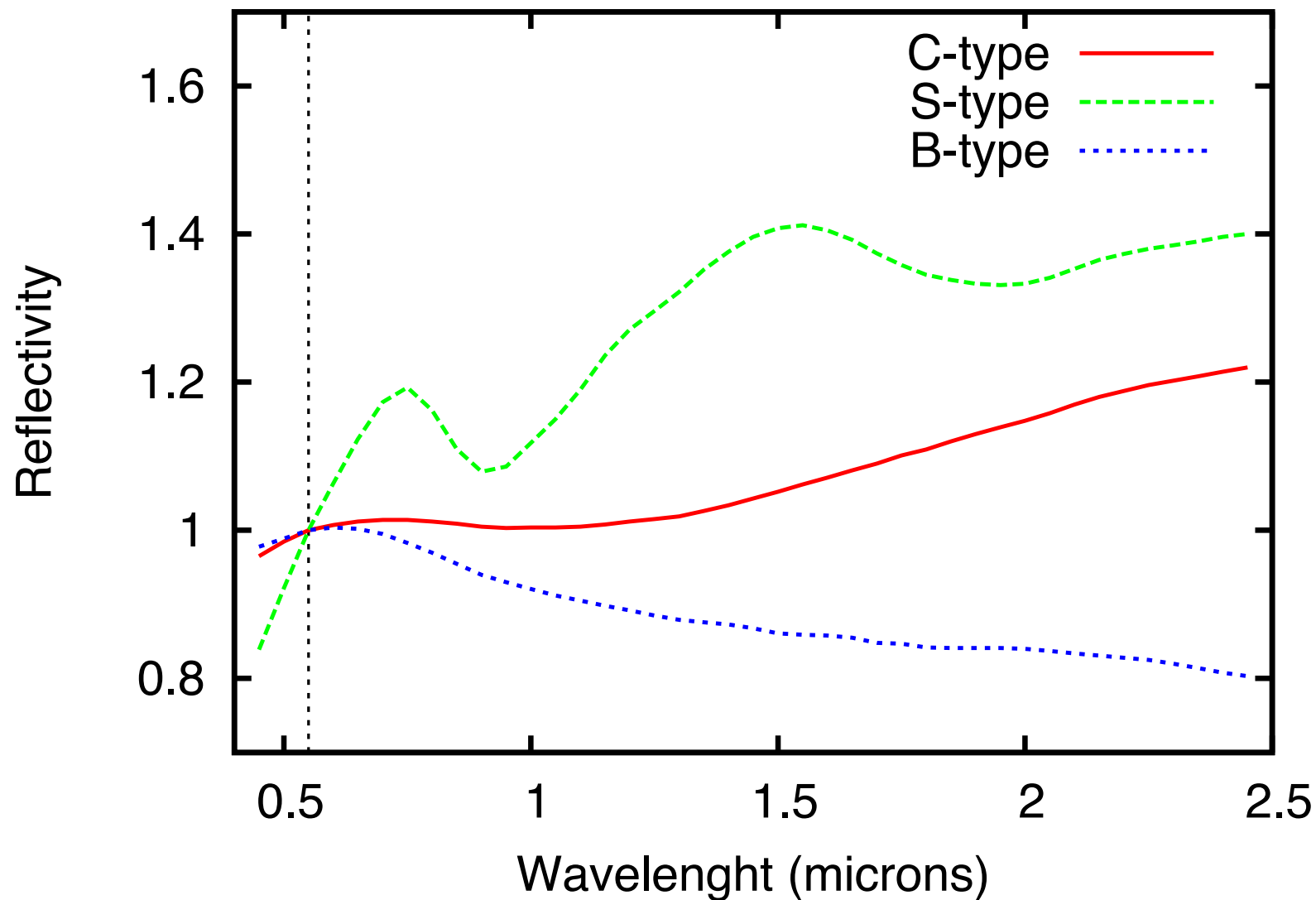
Caveat (continued). More on the case of (84) Alkmene

H	D (km)	p_V	Notes
8.00	61	0.299	Mags from accurate photometry, Fit of the H, G1, G2 system [MBC ⁺ 10]
8.25	61	0.238	Mags from accurate photometry, Fit of the H, G system [MBC ⁺ 10]
8.40	61	0.210	MPC H value (MPCORB.DAT of Nov, 2011)

Diameter from the SIMPS (IRAS) [TNNP02]

- Note that the error on the H value has a dramatic effect on the estimation of the albedo even for this large asteroid.

Albedo as a function of wavelength: normalized reflectivity



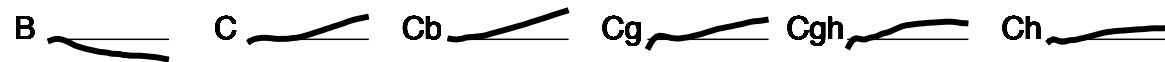
Normalized reflectivity: asteroid spectral classes

Bus-DeMeo Taxonomy Key

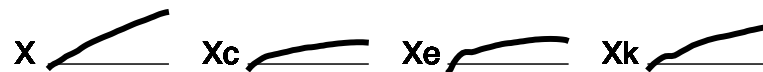
S-complex



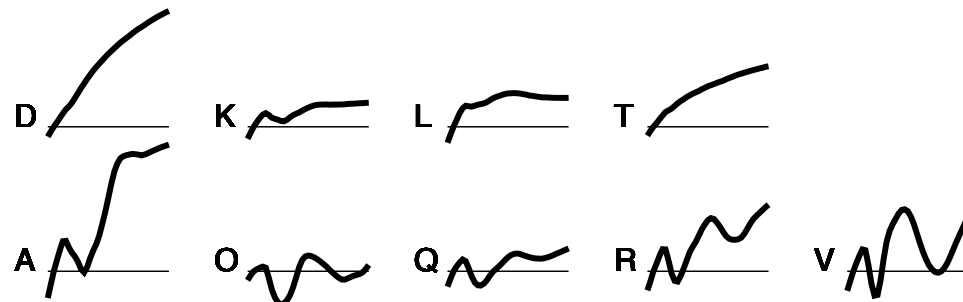
C-complex



X-complex



End Members



<http://smass.mit.edu/busdemeoclass.html>

2. Comparing meteorite and asteroid spectra and albedos

Ordinary Chondrites



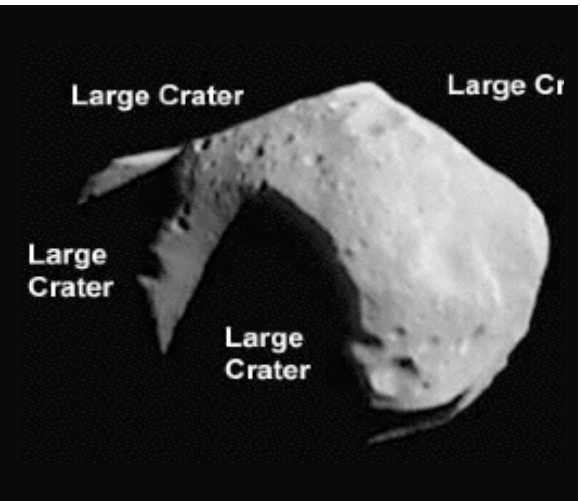
S - class asteroids

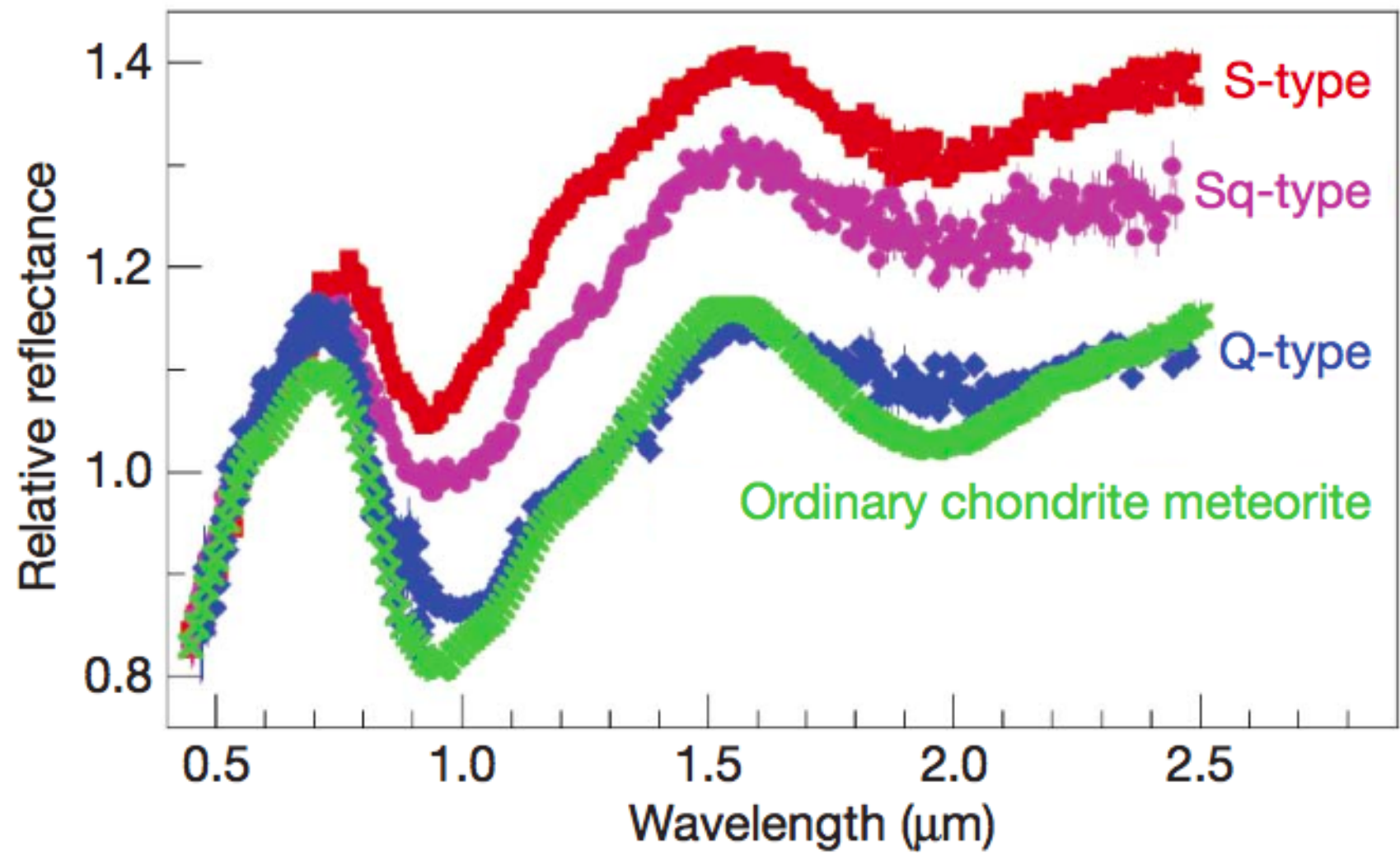


Carbonaceous Chondrites

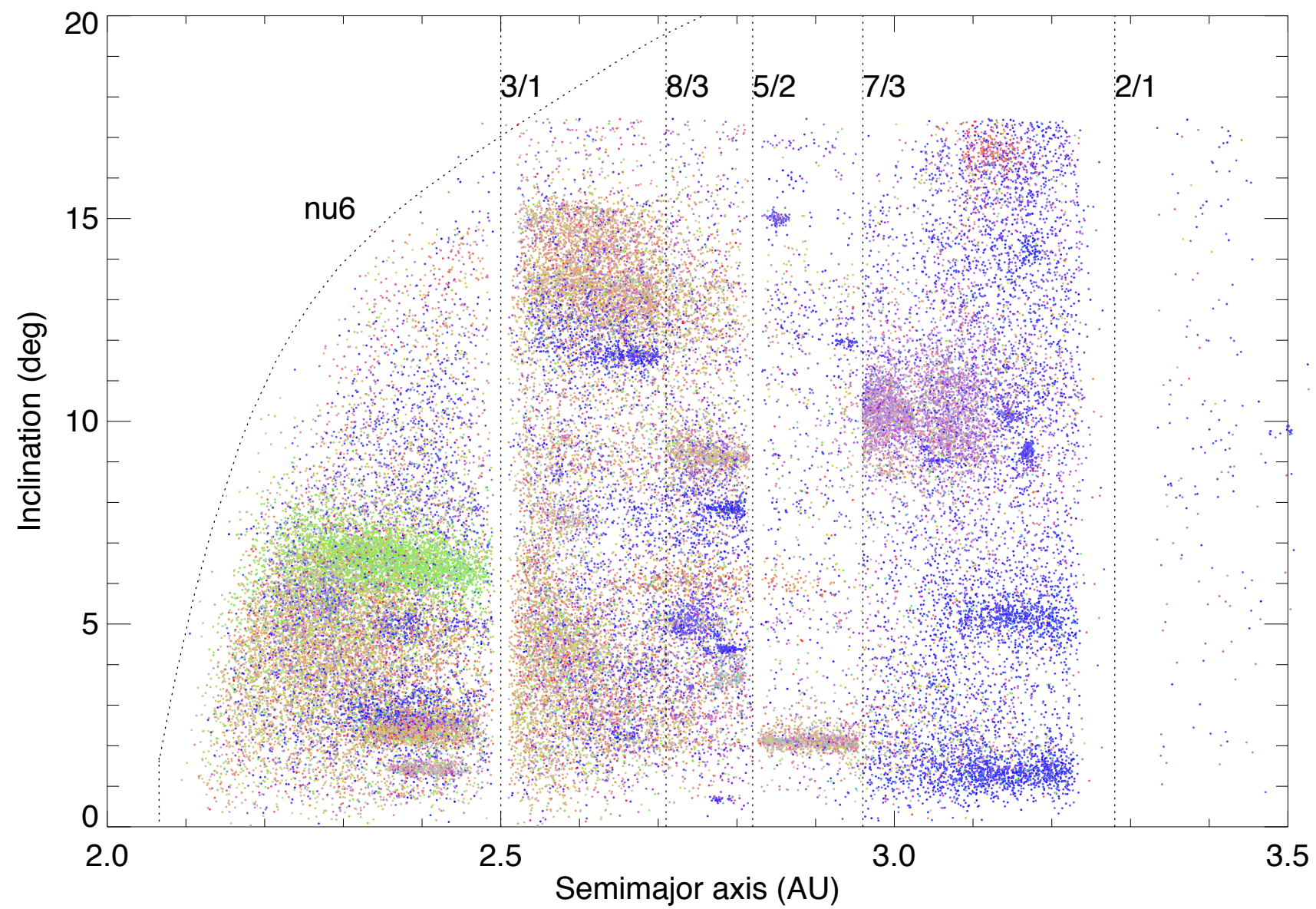


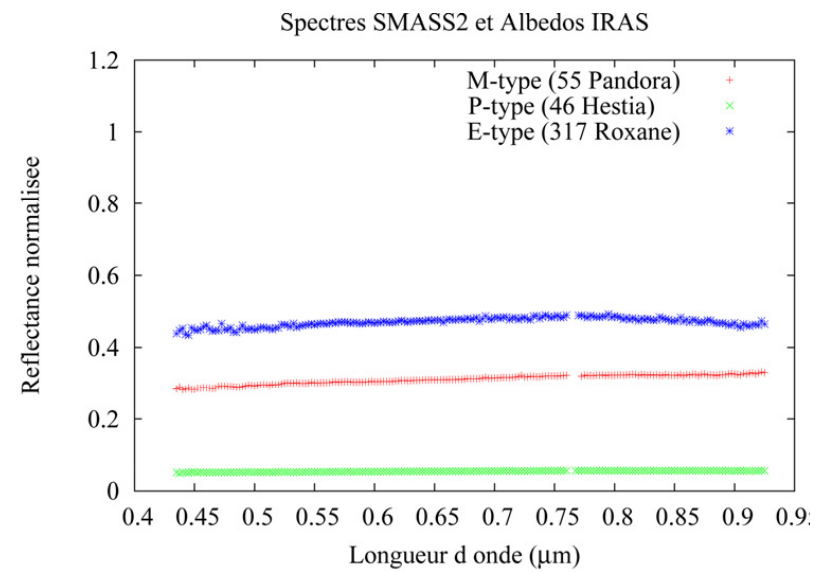
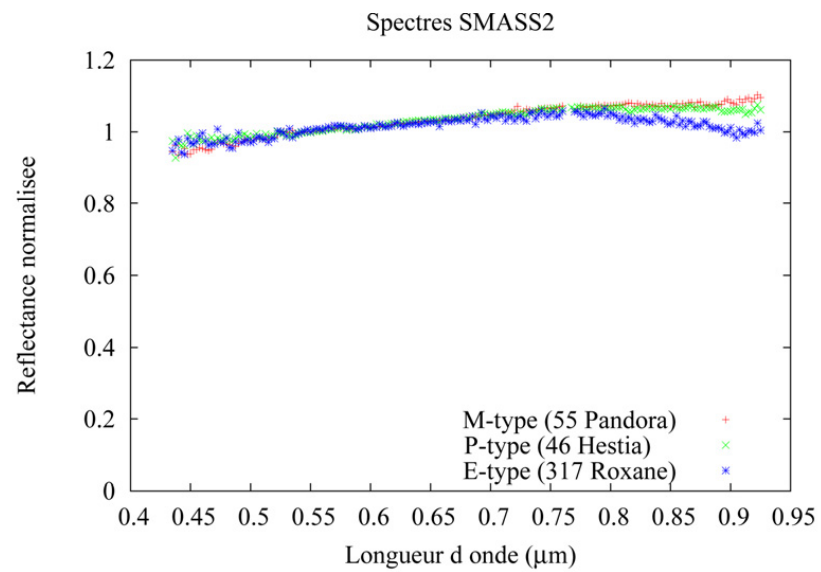
C- class asteroids





[BMM⁺10]



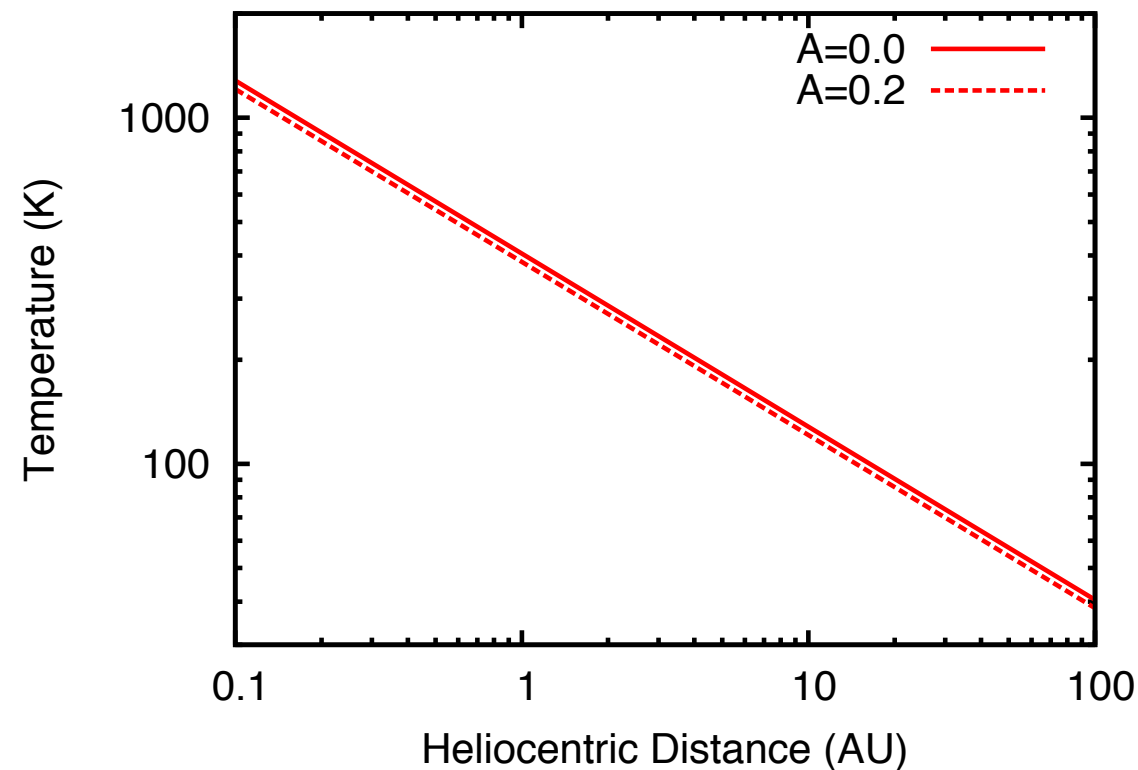


Albedo and input energy at the surface

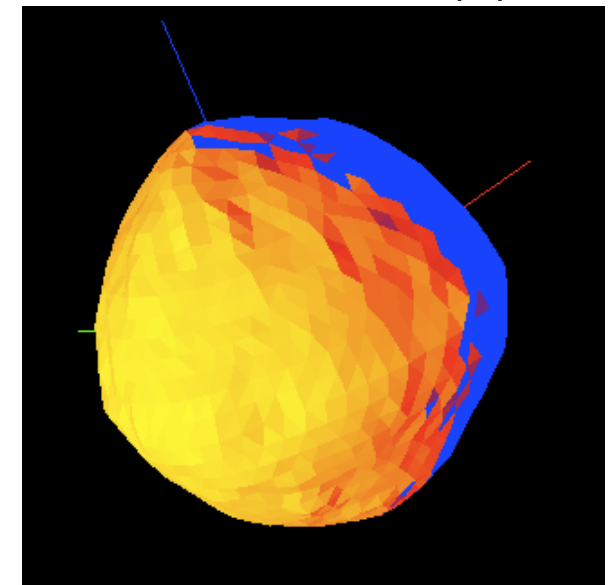
Instantaneous thermal equilibrium

$$(1 - A)S_{\odot}r^{-2}\mu = \epsilon\sigma T^4 \quad (2)$$

For $\mu = 1$ one obtains T_{SS}



$$T_{\mu} = T_{\mu=1} \mu^{1/4} \quad (3)$$



$T_{MAX} = 425K$; $T_{MIN} = 0K$

Albedo and input energy at the surface (2)

Thermal conductivity in the subsurface: Surface boundary condition

$$(1 - A)S_{\odot}r^{-2}\mu = \epsilon\sigma T^4 - \kappa \frac{\partial T}{\partial z} \quad (4)$$

Thermal conductivity in the subsurface: heat diffusion in the regolith

$$\rho C \frac{\partial T}{\partial t} = \frac{\partial}{\partial z} \kappa \frac{\partial T}{\partial z} \quad (5)$$

for κ independent of z

$$\rho C \frac{\partial T}{\partial t} = \kappa \frac{\partial^2 T}{\partial z^2} \quad (6)$$

Thermal conductivity in the subsurface: boundary condition at depth

$$\frac{\partial T}{\partial z} = 0 \quad (7)$$

Heat content in the subsurface

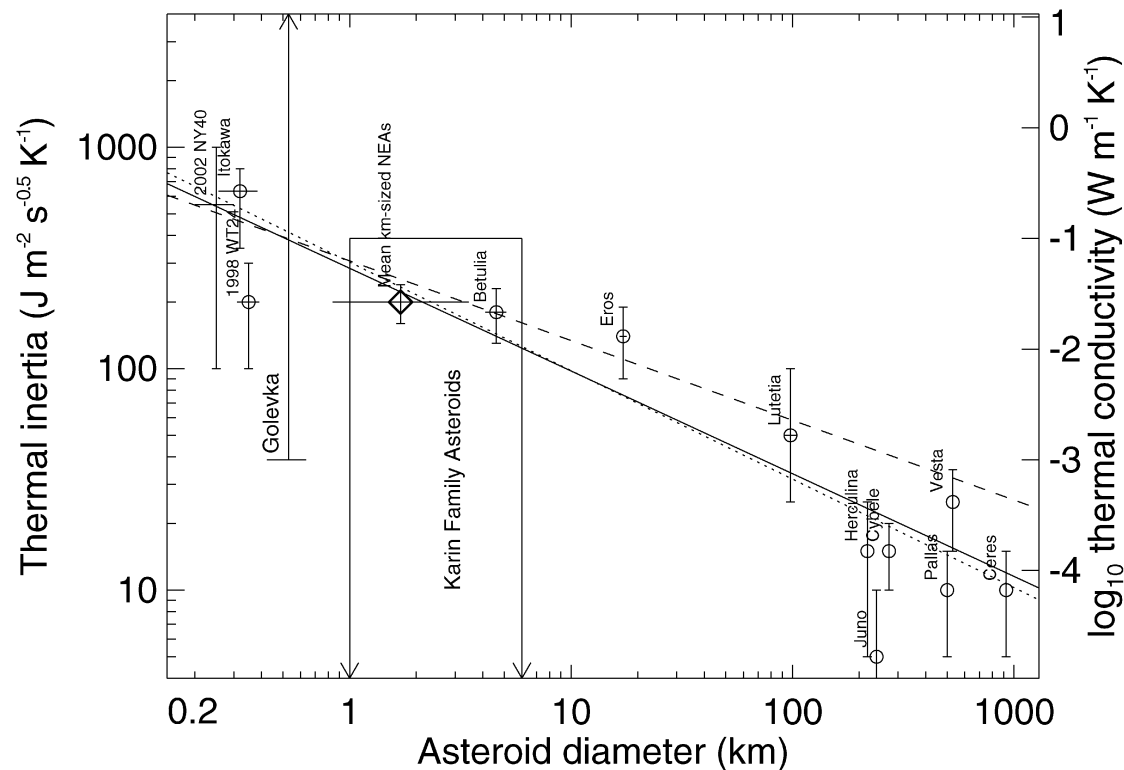
Assume a body is rotating with an angular rotation rate $\omega = \frac{2\pi}{P}$. Diurnal temperature changes propagates in the subsurface with a characteristic length scale l_s (skin depth) given by:

$$l_s = \sqrt{\frac{\kappa}{\rho C \omega}} = \sqrt{\frac{\kappa P}{2\pi \rho C}} \quad (8)$$

At $z = l_s$ the amplitude of the temperature variation is dumped by $e^{-2\pi}$ or about 0.002 of those at the surface. [Wes48]

Heat scale lengths for asteroids and meteoroids

Thermal inertia and thermal conductivity of asteroid surfaces



Assuming $C=600 \text{ J/Kg/K}$ and $\rho=2500 \text{ Kg m}^{-3}$;
[DDH⁺07]

κ	P	I_s
W/m/K		
Diurnal		
10^{-4}	5 h	0.5 mm
10^{-3}	5 h	1.5 mm
10^{-2}	5 h	5.0 mm
1.0	5 h	5.0 cm
Annual		
10^{-2}	1 y	20 cm
10^{-2}	4 y	36 cm
Orbital Evolution		
10^{-2}	10^4 y	18 m
10^{-2}	10^6 y	180 m

Subsurface heat content and thermal inertia

A characteristic heat content per unit area of the subsurface, H_D , can be given by:

$$H_D = l_s T \rho C = \sqrt{\kappa \rho C} \frac{T}{\sqrt{\omega}} = \Gamma \frac{T}{\sqrt{\omega}} \quad (9)$$

where $\Gamma = \sqrt{\kappa \rho C}$ is the thermal inertia [SLS89]

A characteristic time scale, t_R , for radiating this amount of heat is obtained by dividing H_D by the radiated power per unit area $\epsilon \sigma T^4$

$$t_R = \frac{\Gamma}{\sqrt{\omega} \epsilon \sigma T^3} \quad (10)$$

[SLS89]

Thermal parameter

The ratio of t_R to the rotation rate of the body $1/\omega$ measures the ability of the surface to keep up with diurnal insolation changes

$$t_R/\omega = \Theta = \frac{\Gamma\sqrt{\omega}}{\epsilon\sigma T^3} \quad (11)$$

[SLS89]

- ▶ $\Theta = 0 \rightarrow$ instantaneous thermal equilibrium
- ▶ $\Theta \rightarrow \infty \rightarrow$ perfectly flat temperature distribution (independent of longitude).

Thermal parameter vs Heliocentric distance

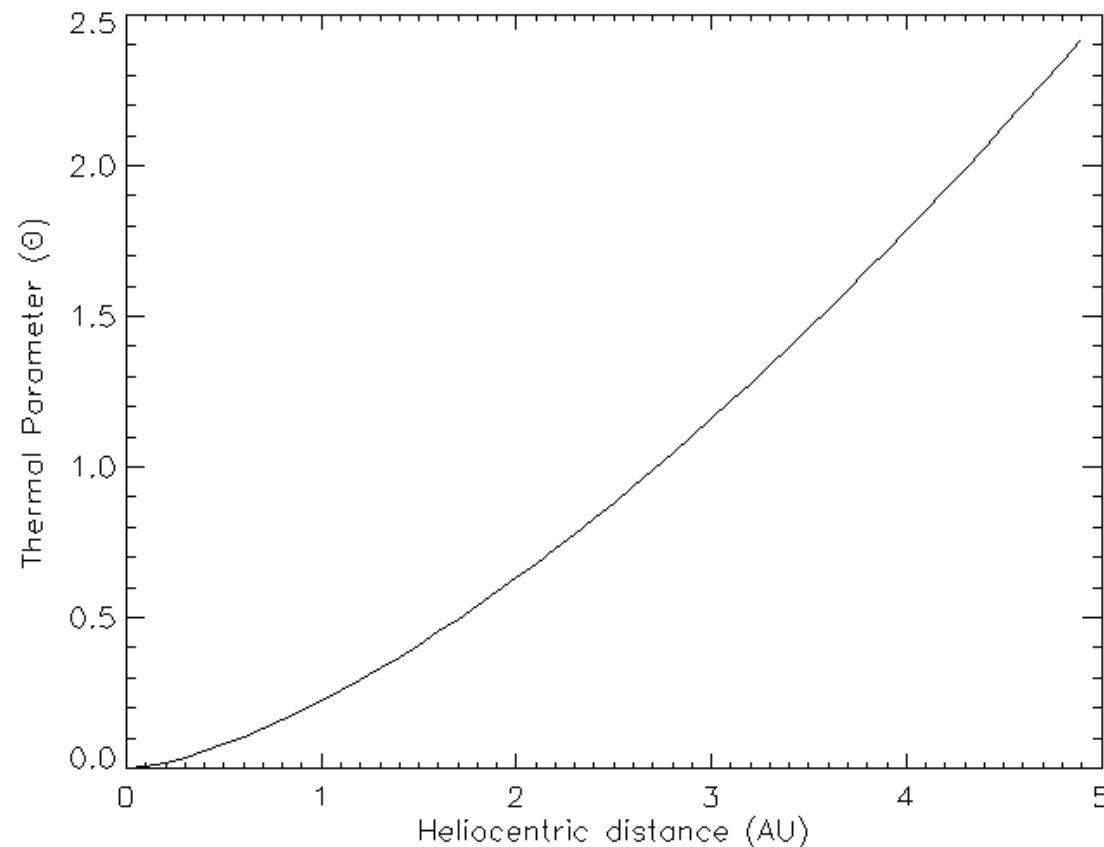
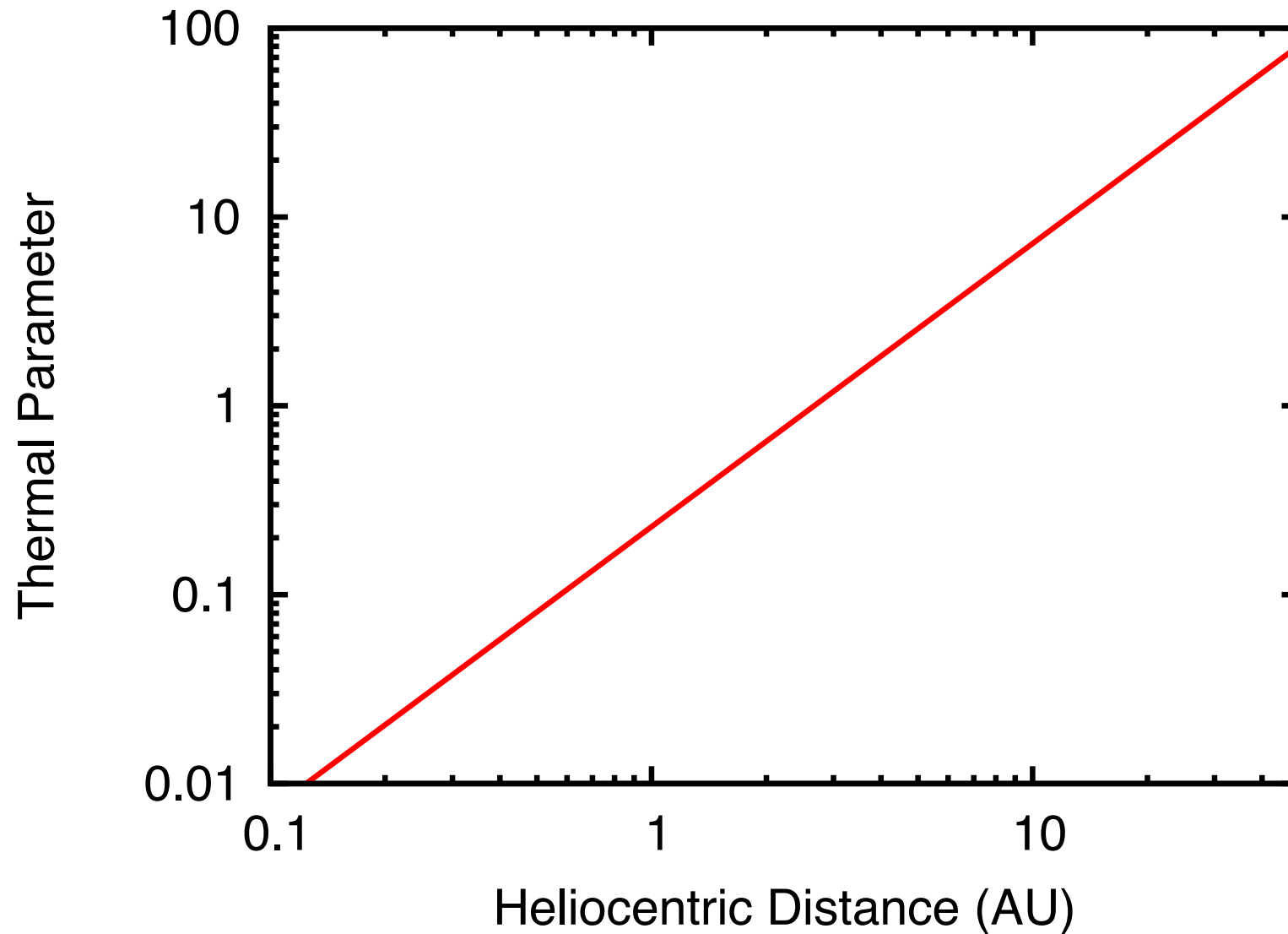


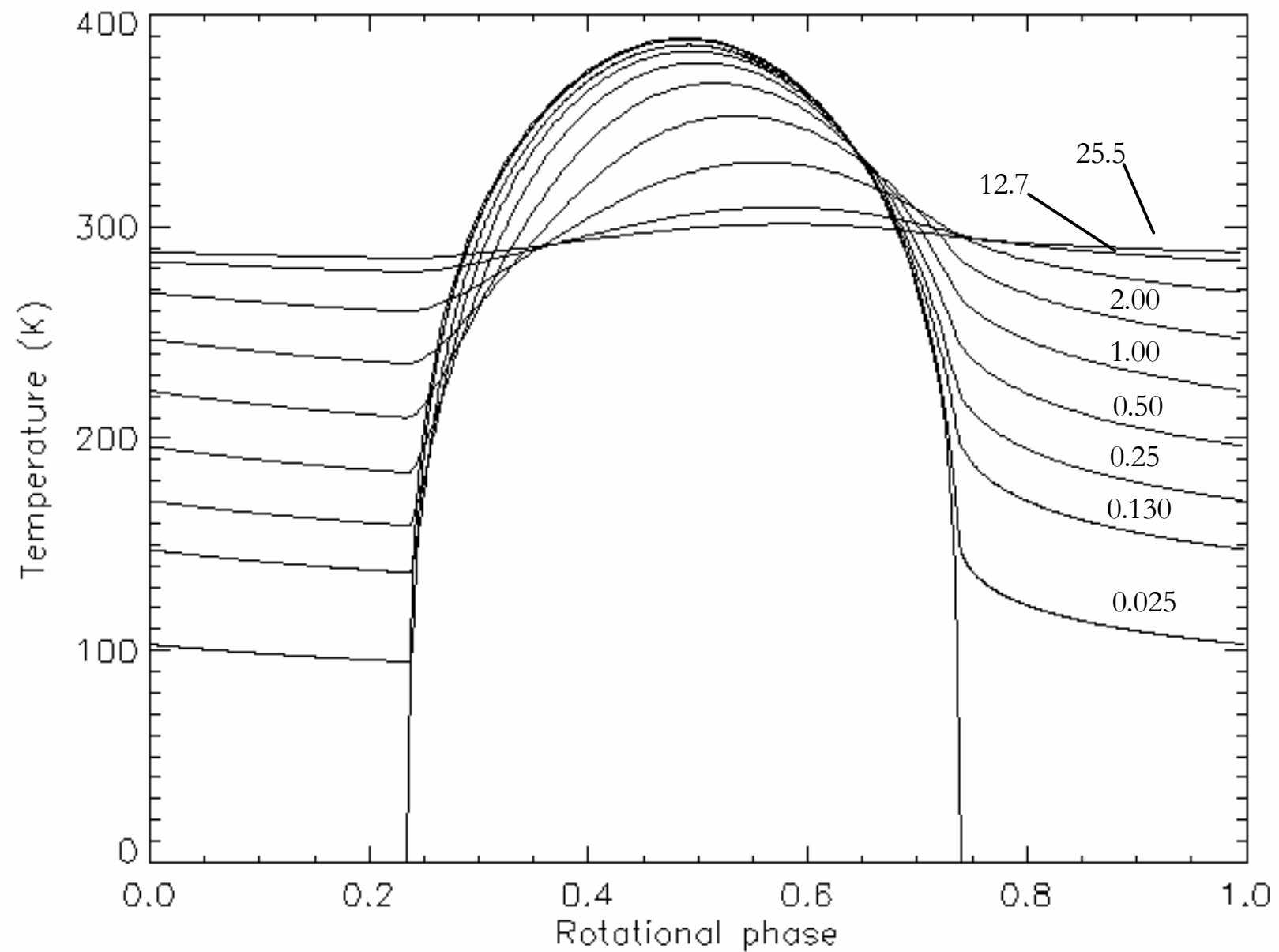
Fig. 6.2 Plot of the thermal parameter Θ as a function of the heliocentric distance. The thermal inertia, $\Gamma = 40 \text{ J m}^{-2} \text{ s}^{-1} \text{ K}^{-1}$, has a quasi-lunar like value. The bolometric bond albedo $A = 0.05$; emissivity $\epsilon = 1$ and asteroid sidereal rotation period $T_{\text{SID}} = 5$ hours. Note that for a given value of Γ and T_{SID} , NEAs have smaller values for Θ than objects more distant from the Sun.

[Del04]

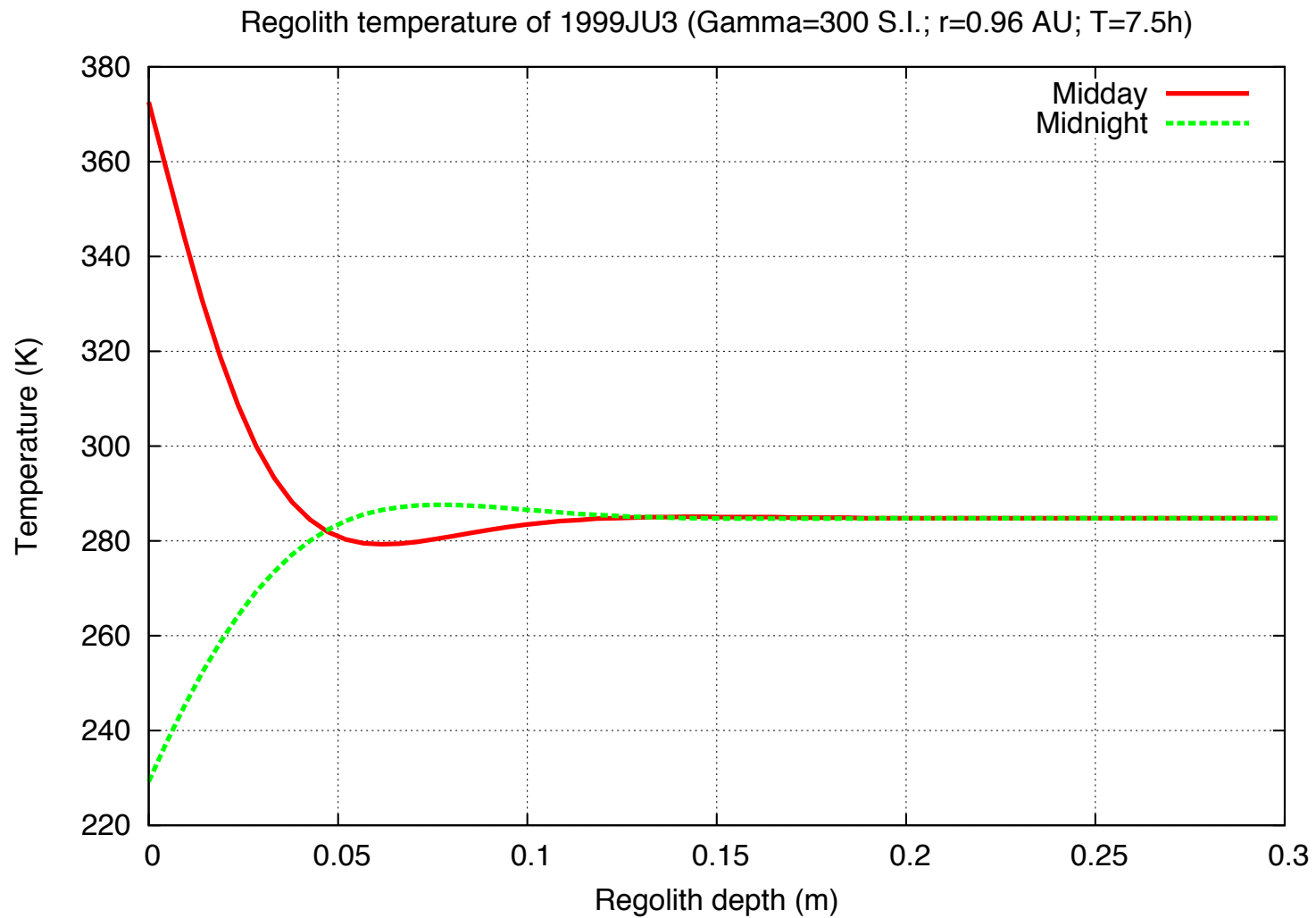
Thermal parameter vs Heliocentric distance (2)



Surface temperature distribution


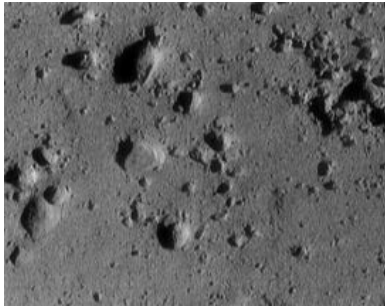

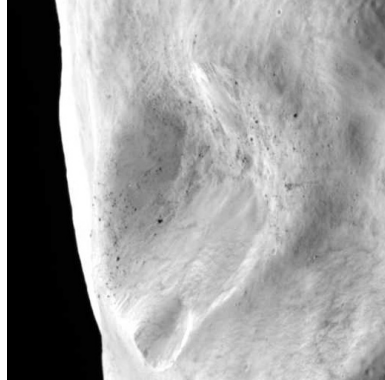


Subsoil temperature (1999 JU₃): $\Gamma = 300 Jm^{-2}s^{-0.5}K^{-1}$



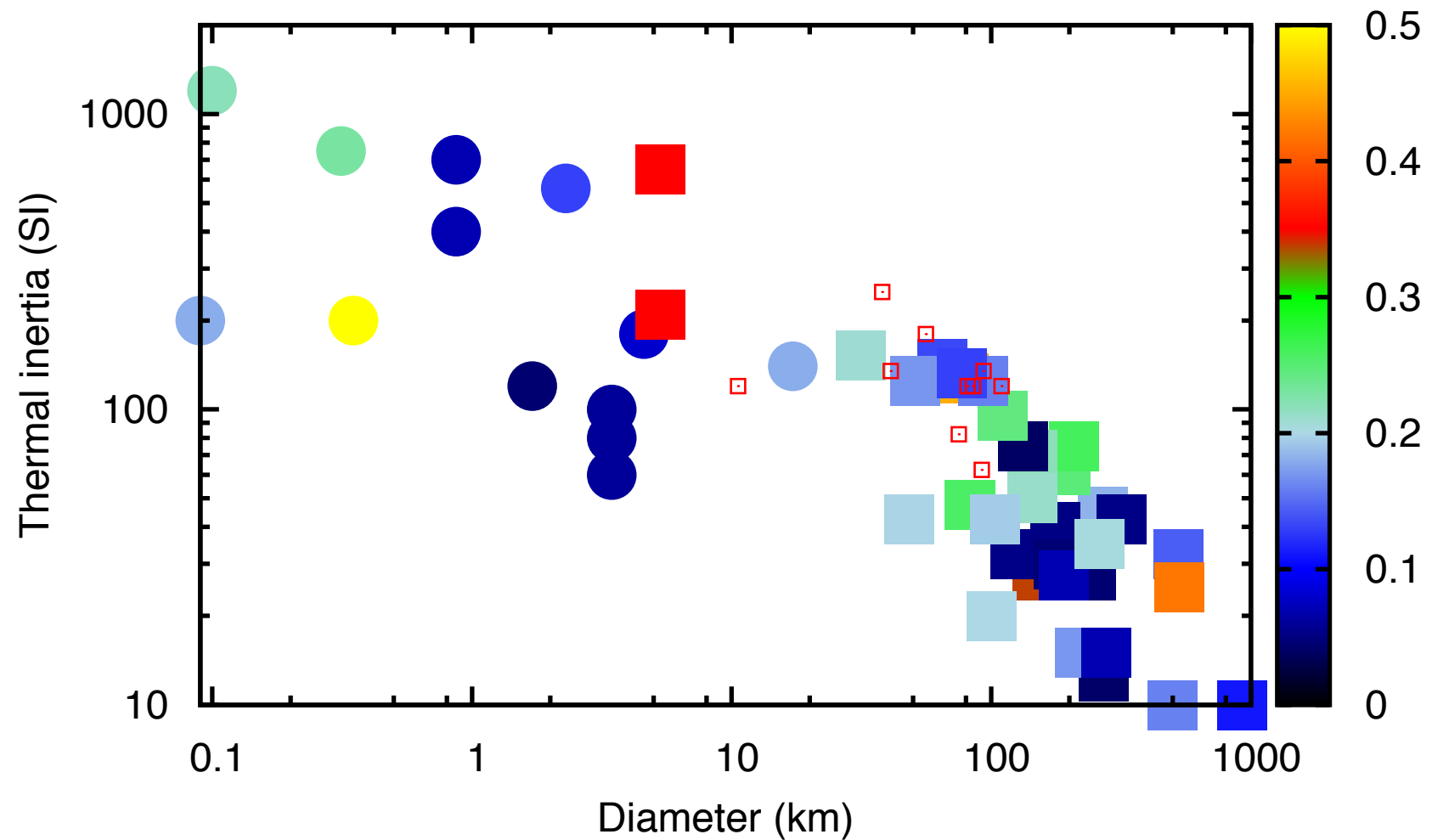
Thermal inertia (Γ) and asteroid surface regolith nature

Thermal inertia gives information about the presence (or absence), depth and thickness of regolith, and the presence of exposed rocks on the surface of atmosphere-less bodies (Γ in SI units: $Jm^{-2}s^{-0.5}K^{-1}$).

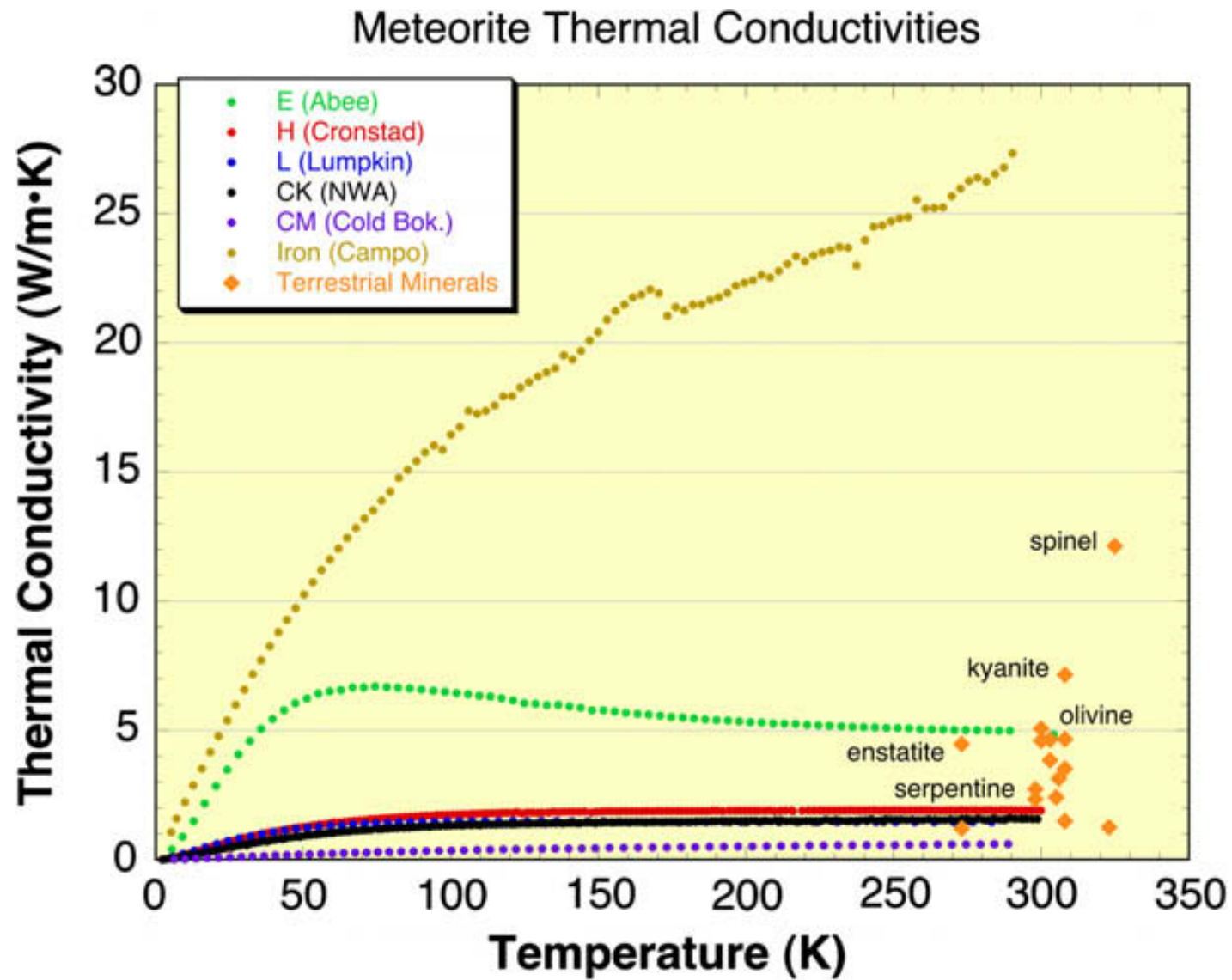
25143 Itokawa	433 Eros	The moon	21 Lutetia
$\Gamma = 750$	$\Gamma = 150$	$\Gamma = 40 - 50$	$\Gamma = 20$
 <small>Release 051101-4 ISAS/JAXA</small>			
Coarse regolith and boulders	Finer and thicker regolith	Mature and fine regolith	Very fine regolith

Thermal inertia of asteroids: the big picture

Color palette: geometric visible albedo (p_V)

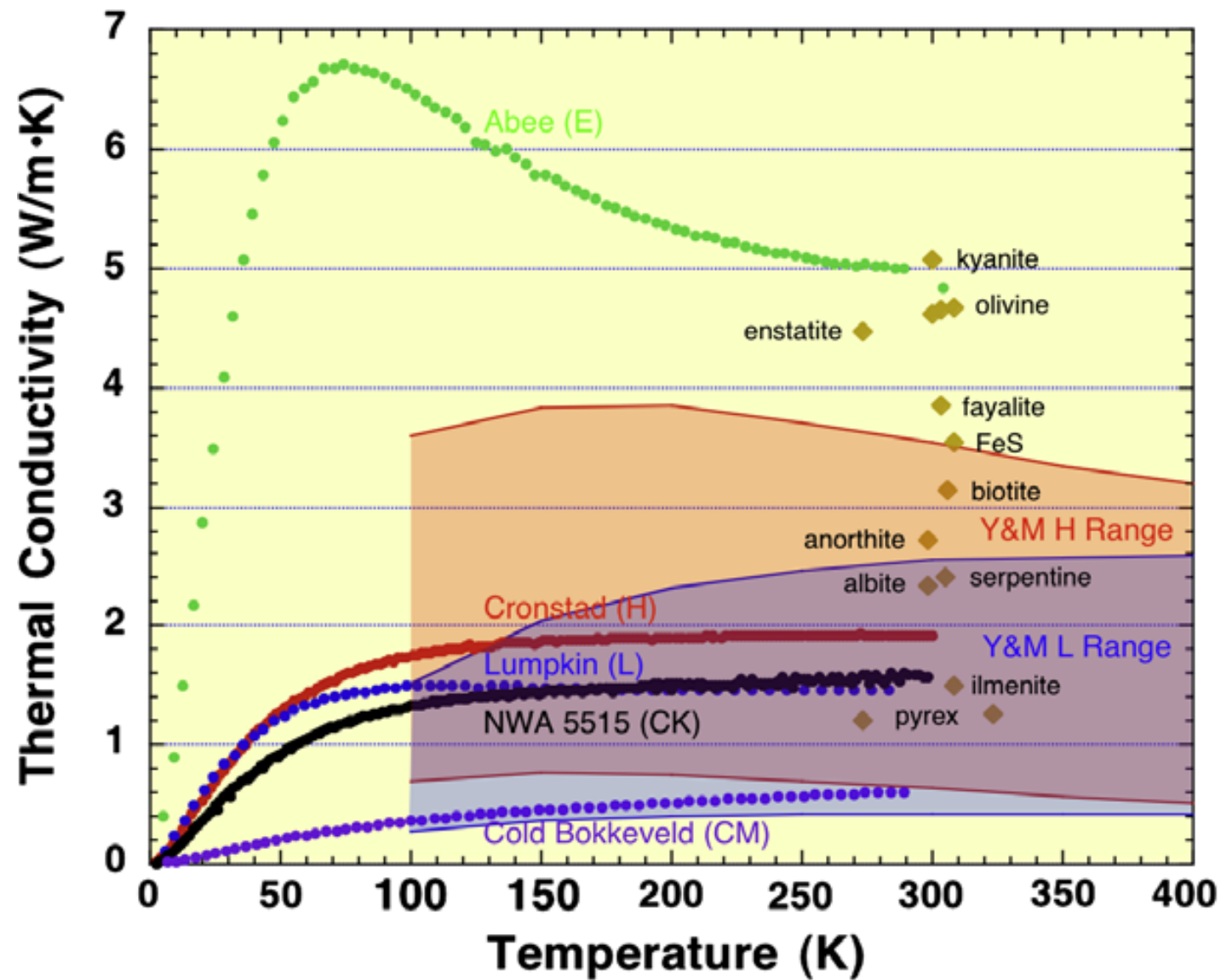


Thermal conductivity of meteorites



[OCB10]

Thermal conductivity of meteorites (2)



[OCB10]

Thermal conductivity of asteroids - meteorites: porosity

$$\kappa = \psi \kappa_{pores} + (1 - \psi) \kappa_{solid} \quad (12)$$

- ▶ κ is the effective thermal conductivity;
- ▶ κ_{pores} is the effective thermal conductivity of the pores;
- ▶ κ_{solid} is the effective thermal conductivity of the solid;
- ▶ ψ is the porosity;

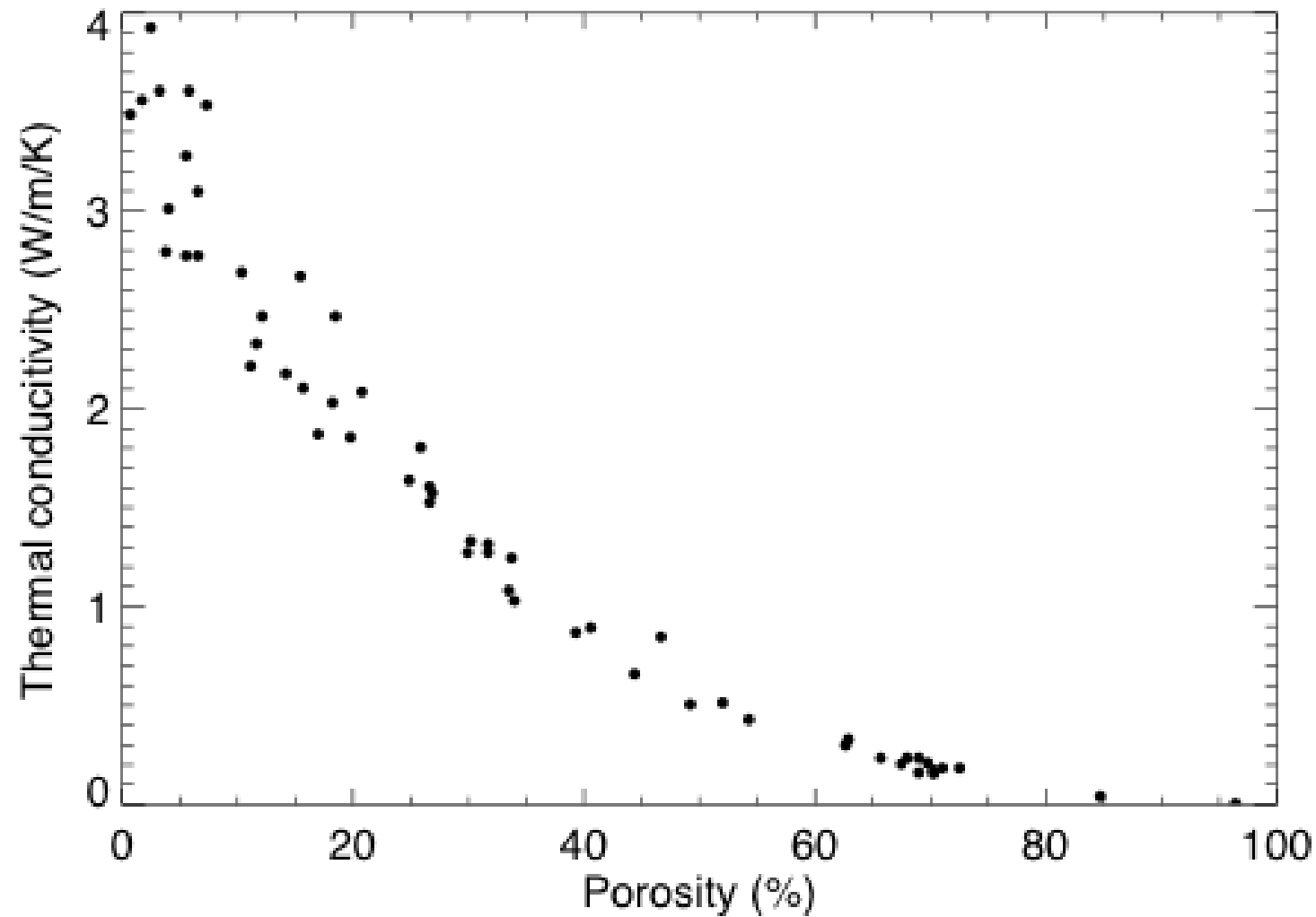
theoretically:

- ▶ $\kappa_{pores} = 4\epsilon\sigma r_{pores} T^3$, where:
- ▶ σ is the Stefan Boltzmann constant;
- ▶ ϵ is the emissivity;
- ▶ r_{pores} is the typical radius of the pores;

Porosity - Implication

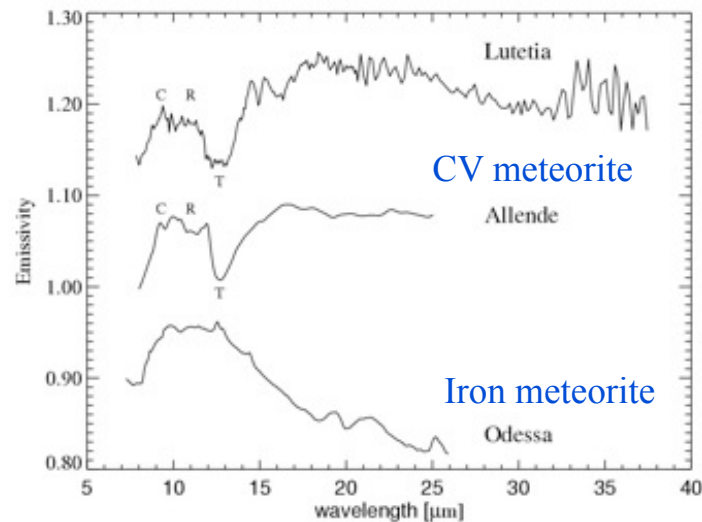
- ▶ κ is function of temperature and thus depth in the regolith, time of the day, orbital position, season....
- ▶ Low- κ (i.e. low- Γ) asteroids must have substantial surface porosity: thick and fine regolith layer

Thermal conductivity and porosity: experimental view



[Zim86]

Emissivity $\epsilon = (1 - R)$



•The Lutetia emissivity spectrum is completely different from that of the iron meteorites

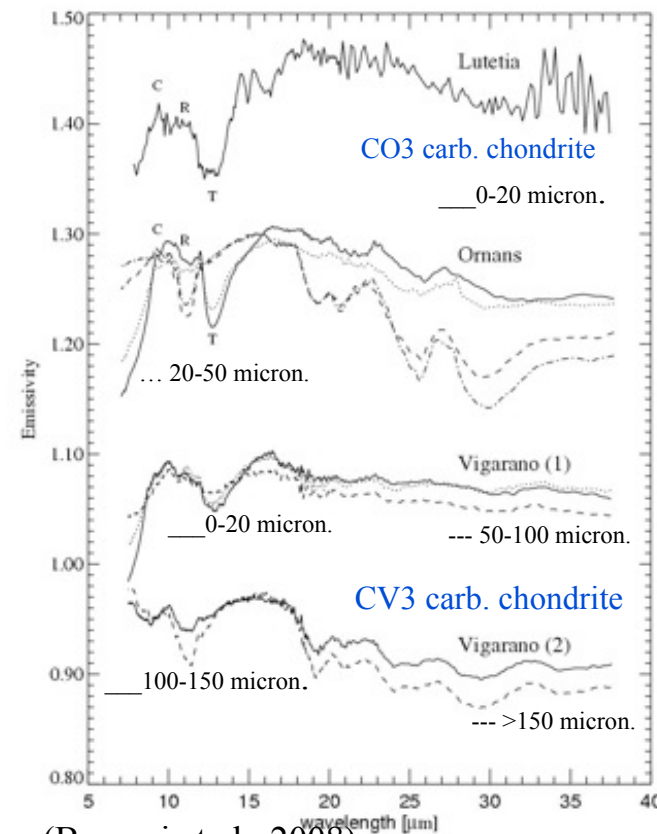
•Low thermal inertia: $I \leq 30 \text{ JK}^{-1} \text{ m}^{-2} \text{ s}^{-1/2}$, typical of main belt asteroids; Lutetia is likely covered by a thick regolith layer

•Lutetia is similar to CV3 and CO3 carbonaceous chondrites, meteorites which experienced some aqueous alteration

Enstatite chondrites C peak at 8.3 μm
(Izawa et al. 2010)

Wednesday, October 19, 2011

21 LUTETIA: Emissivity - SPITZER



(Barucci et al., 2008)

Energy output and flux

Gray body emitter (for a surface element of area Ω):

$$f(\lambda) = \Delta^{-2} \epsilon(\lambda) B(\lambda, T) \hat{N} \bullet \hat{\Delta} \Omega \quad (13)$$

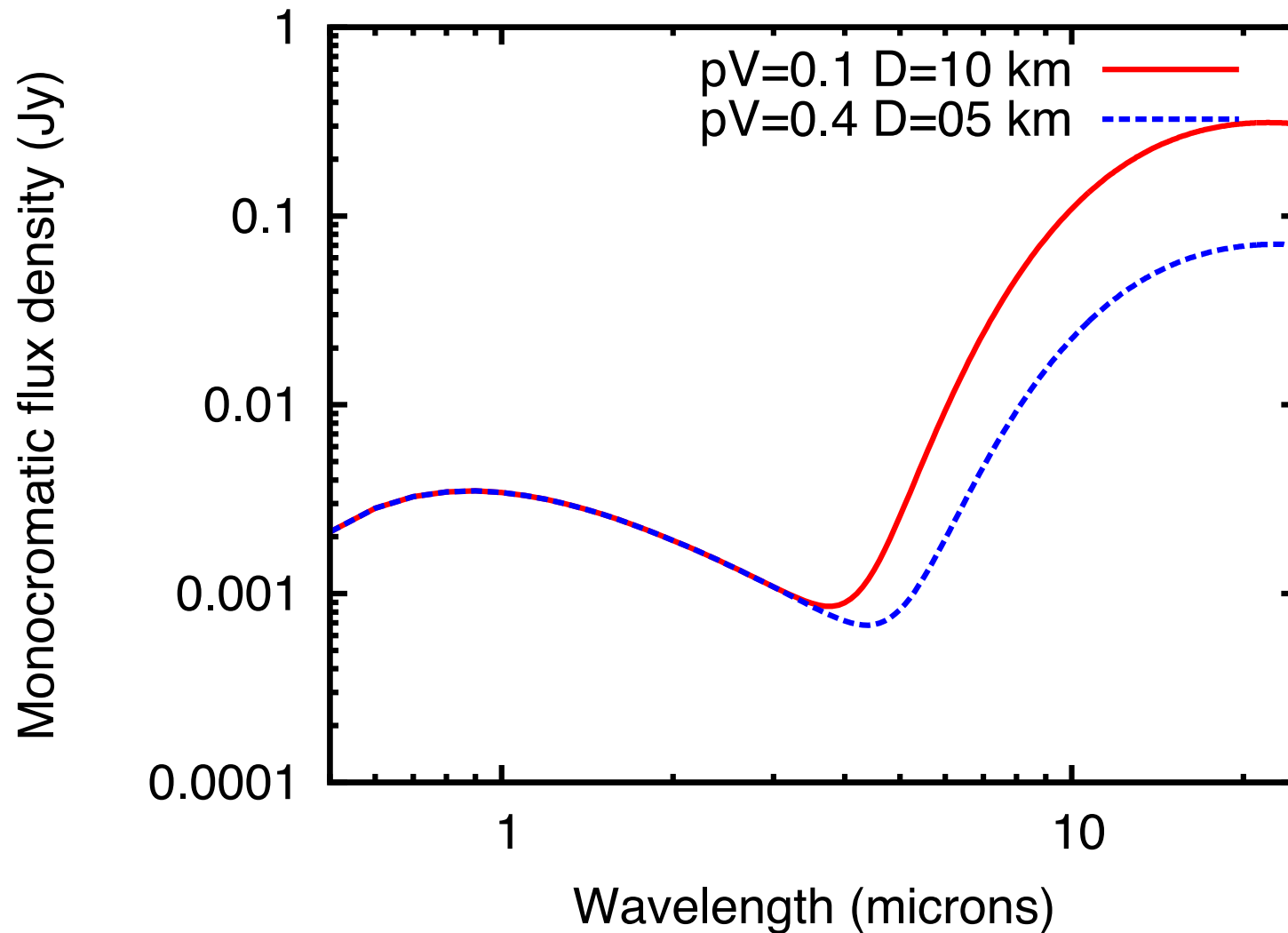
with:

$$B(\lambda, T) = \frac{2\pi hc^2}{\lambda^5} \frac{1}{\exp(\frac{hc}{\lambda kT}) - 1} \quad (14)$$

For the whole body (Σ is the surface visible to the observer):

$$F(\lambda) = \frac{1}{\Delta^2} \int_{\Sigma} \epsilon(\lambda, \Omega) B(\lambda, T(\Omega)) \hat{N}(\Omega) \bullet \hat{\Delta} d\Omega \quad (15)$$

Exemple Flux from two asteroids



Same visible and near-IR flux (reflected light), so same H -mag, but factor of 4 difference in the thermal IR (emitted) flux.

Thermal conductivity in the subsurface

Thermal conductivity in the subsurface and viewing of other facets
(non convex shape of the body)

$$(1 - A)S_{\odot}r^{-2}\mu = \epsilon\sigma T^4 - \kappa\frac{\partial T}{\partial z} + TBD + TBD \quad (16)$$

Thermal Physics of Asteroids (2nd lesson)

Charles University of Prague – Oct/Nov 2011

Marco Delbo

UNS-CNRS-Observatoire de la Côte d'Azur

Visiting: Astronomical Institute of the Charles University, Prague, CZ

October 26, 2011

Asteroids: when size matters

Sizes

- ▶ Size frequency distribution
- ▶ Collisional evolution of the belt
- ▶ Impact hazards (e.g. ask to the Dinosaurs)

Sizes from H (it does not work)

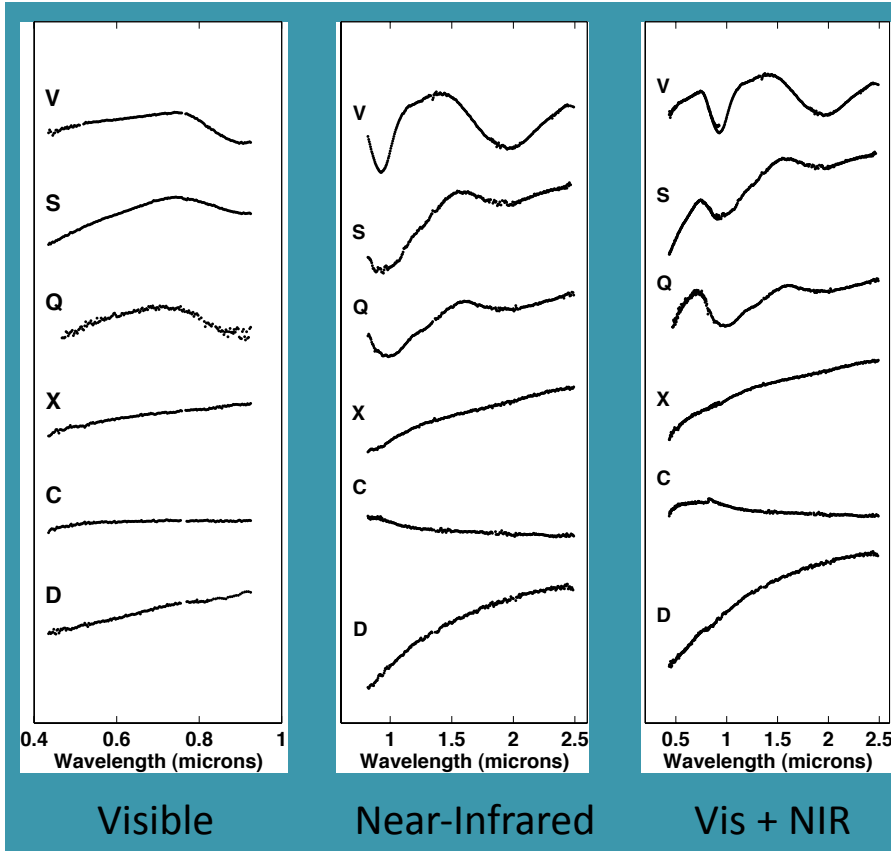
Consider 2 asteroids with equal visible magnitude:

H	p_V	D (km)
14.622	0.1	10.0
14.622	0.4	5.0

... but very different diameters, given the different albedos. Asteroids' p_V are in the range between 0.03 and 0.5 [?, TTE⁺11]

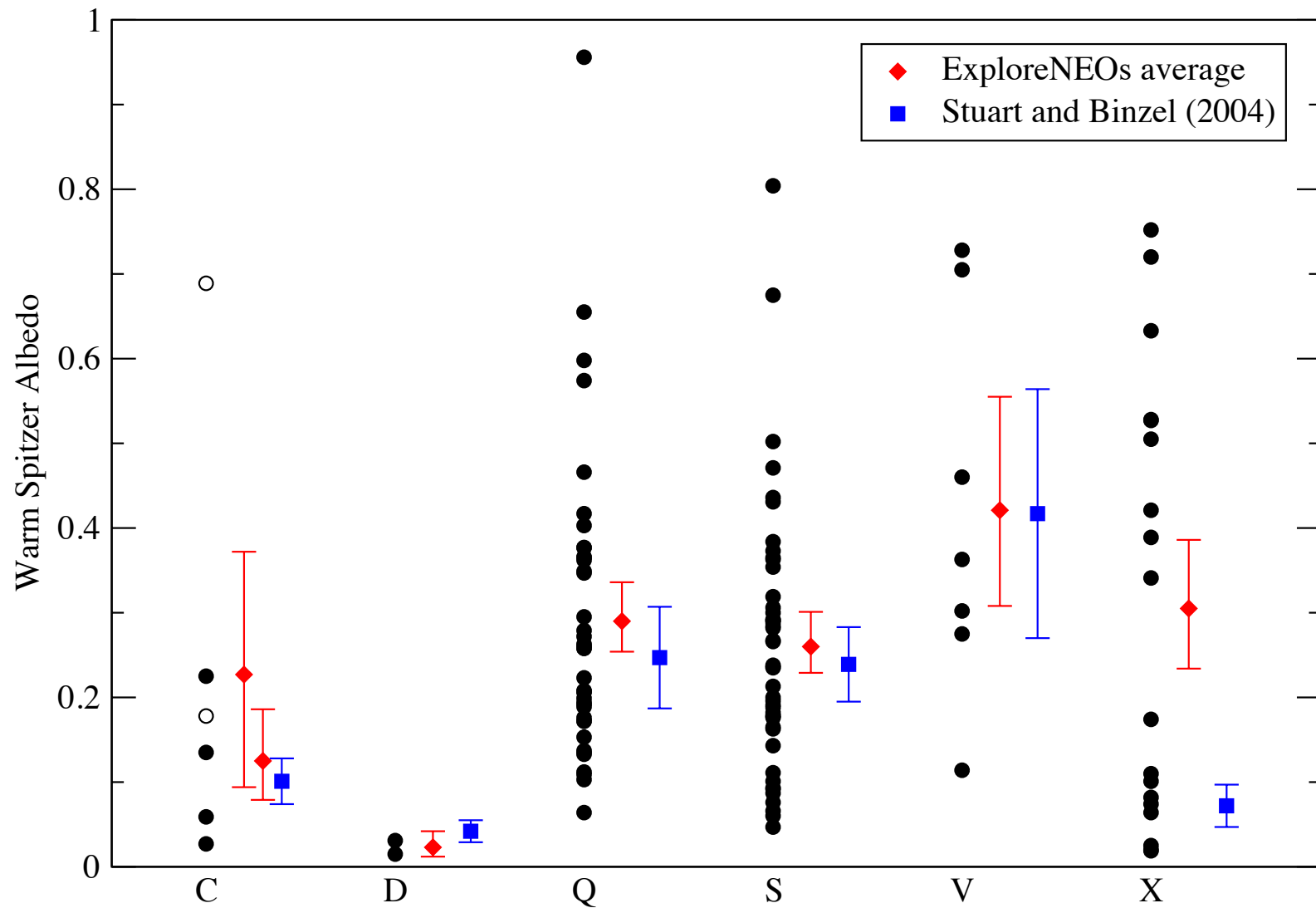
So, large uncertainty in size if the albedo is not known.

Spectroscopy of asteroids and spectral classes



- Different taxonomic types are products of different materials and/or histories
- Same taxonomic type does not guarantee same mineralogy

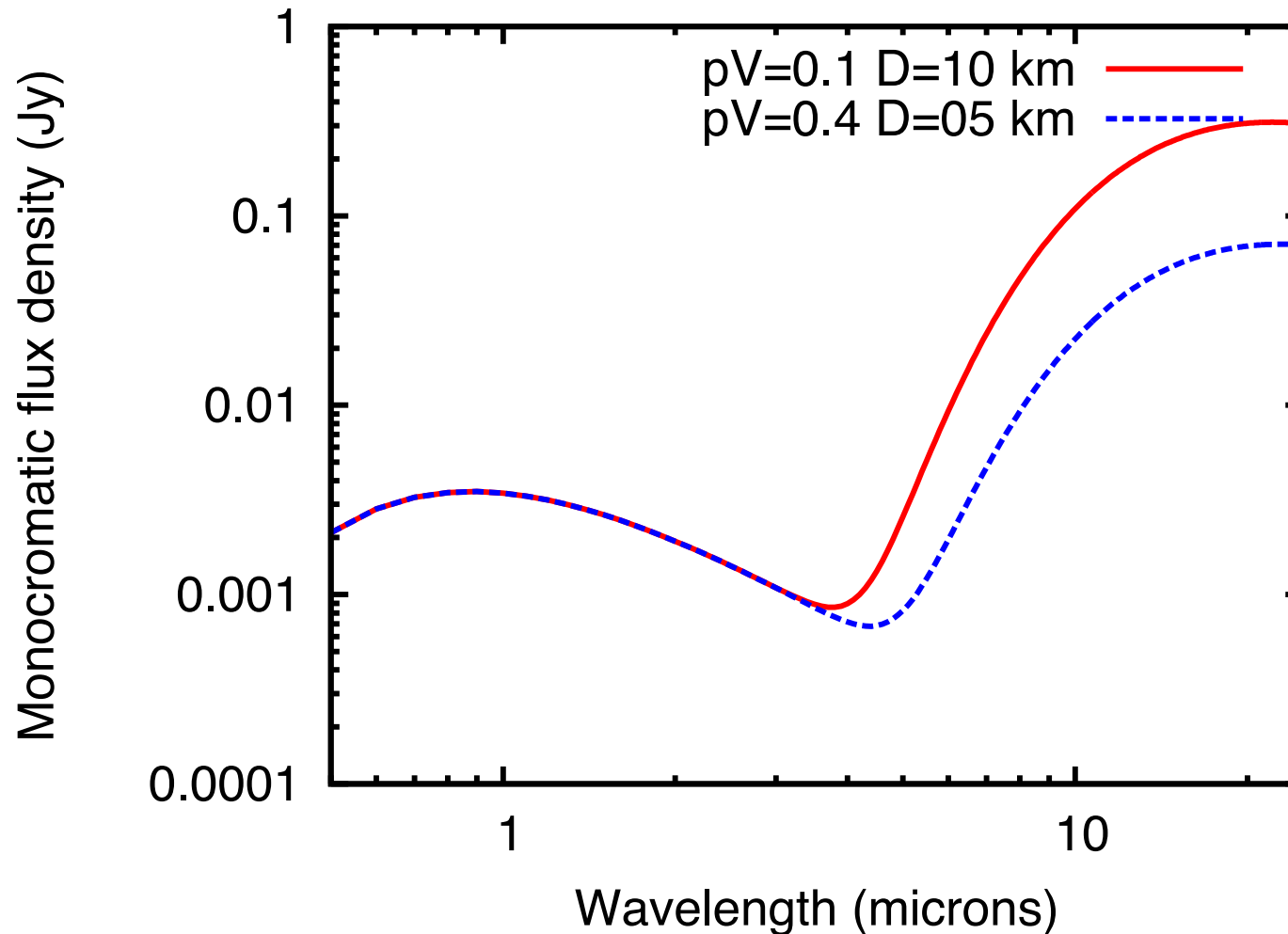
Range of albedo of asteroid spectral classes



[TTE⁺11]

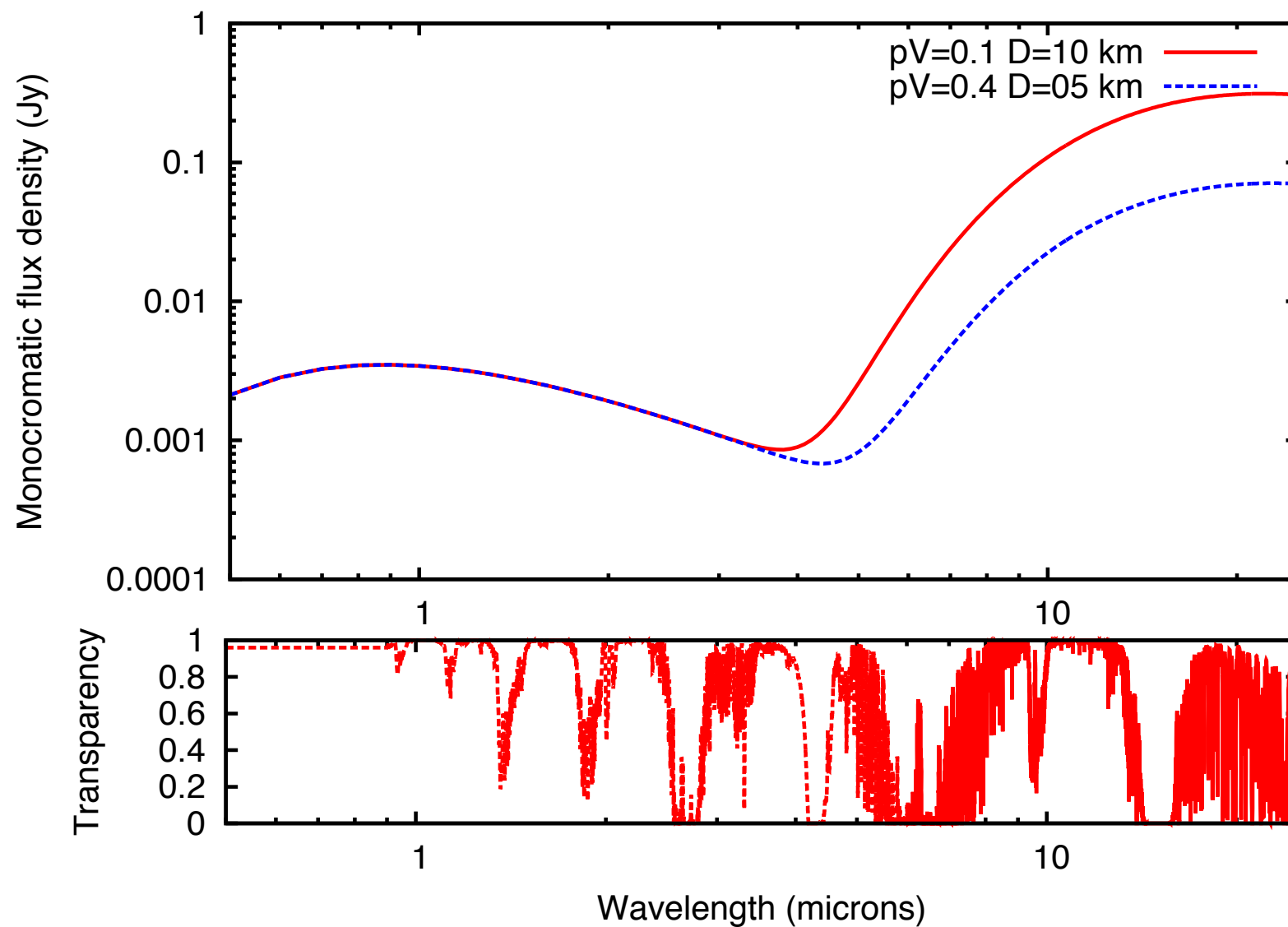
Statistical sense only... not good for single objects

Size determination from thermal-IR



Same visible and near-IR flux (reflected light), so same H -mag, but factor of 4 difference in the thermal IR (emitted) flux.

Asteroid flux and atmospheric transparency



Atmospheric transmission, bands and MID-IR filters

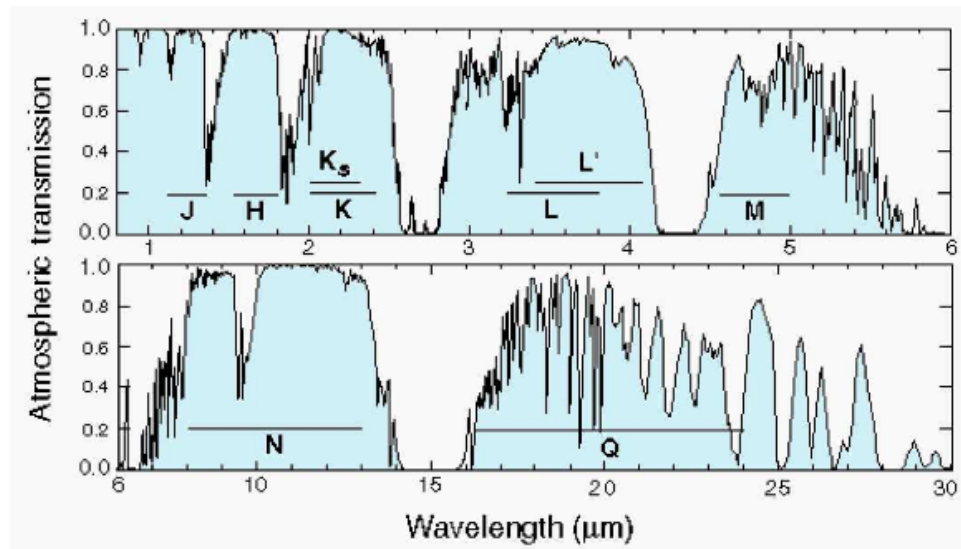
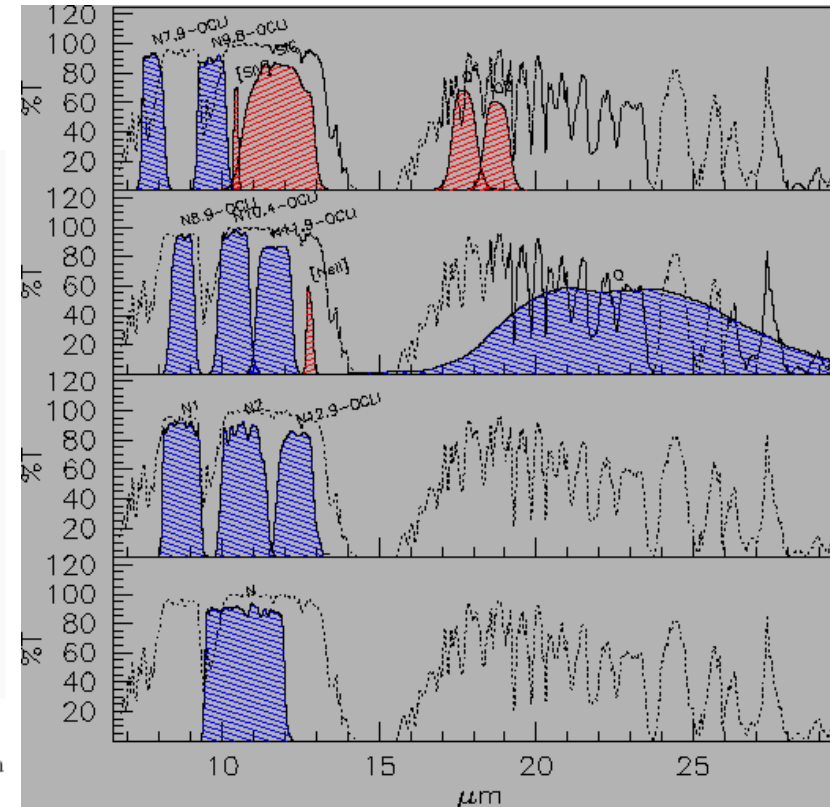


Figure 6: Atmospheric transmission at IR wavelengths, and the main photometric bands. From *Allen's Astrophysical Quantities*



Our atmosphere absorbs the majority of the MIR radiation from astronomical sources. The main absorbing molecules are H₂O, CH₄, CO₂, CO, O₂, O₃. However, the atmosphere is quite transparent in two atmospheric windows: the N and Q bands.

Atmospheric Emission: thermal background

Moreover, ground-based observations in this region are much different than the one in the optical or near infrared because of the very large thermal background flux that peaks near $10 \mu m$

$$\lambda_{peak}(\mu m) = \frac{3000}{T(K)} \quad (17)$$

For $T=300$ K, peak of thermal emission is $10 \mu m$.

Summary

Atmosphere, telescope thermal emission peak at $10 \mu m$.

Instrument Example: VISIR@ESO

Overview

Imaging and long-slit spectroscopy with VISIR can be achieved at several spatial and spectral resolution. The imager and spectrograph are two sub-instruments. They have independent light paths, optics and detectors. The spectrometer has two arms, one with low order gratings for the low and medium spectral resolution, the other with large echelle gratings providing high spectral resolution. The cryogenic optical bench is enclosed in a vacuum vessel. The vessel is a cylinder, 1.2m long and 1.5m in diameter. Standard Gifford-McMahon closed-cycle coolers are used to maintain the required temperature: 33K for most of the structure and optics and < 15K for the parts near the detector. The detectors are cooled down to ~7K. The imager can be used either in standard readout mode or in **burst readout mode**.

Imaging

spectral range [μm]	pixel field of view [arcsec]	total field of view [arcsec ²]	filter
8 - 13, 17 - 24	0.075	19.2 x 19.2	broad and narrow band filters
8 - 13, 17 - 24	0.127	32.3 x 32.3	

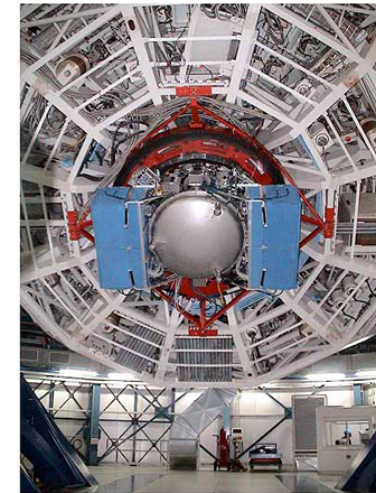
pfov is selectable for both wavelength regions

Spectroscopy

grating	offered central wavelengths [μm]	resolving power
low resolution (LR)	8.1, 8.5, 8.8, 9.8, 11.4, 12.2 and 12.4 μm	R ~ 350 at 10 μm
medium resolution (MR)	7.5 to 9.3 μm , 10.2 to 13.0 μm , 17.1 to 19.0 μm , 20.12 μm	R ~ 3200 at 10 μm
high resolution - long slit (HR)	8.02, 12.81 and 17.03 μm	R ~ 25000 at 10 μm
HR - cross dispersed (HRX)	8.970 - 9.140 μm , 9.360 - 9.690 μm , 10.480 - 10.540 μm , 11.540 - 11.570 μm , 11.762 μm , 12.210 - 12.760 μm , 12.814 - 13.364 μm , 16.390 μm , 16.925 μm , 17.790 - 17.980 μm , 18.246 μm , 18.680 - 18.960 μm , 21.295 μm	R ~ 25000 at 10 μm

<http://www.eso.org/sci/facilities/paranal/instruments/visir/index.html>

Instrument Example: VISIR@ESO



VISIR Mounted behind the 8.2-m Mirror of Melipal

ESO PR Photo 16b/04 (12 May 2004)

© European Southern Observatory



Instrument Example: VISIR@ESO - Detector UPGRADE

Characteristics Raytheon Aquarius Detector

Characteristic	Value	Comment
Array Size	1024 x 1024 pixels	30 μm square pixels
Spectral Response	3 – 28 μm	Not measured yet but Arrhenius plot indicates a 28 μm cut-off
Operating temperature	6K	Power dissipation of detector measured to be ~ 150 mW
Integration Capacity	0.6×10^6 e ⁻ 6×10^6 e ⁻	Programmable high and low gain
Input referred Noise (e rms)	< 300 e rms (high gain, speed) (~ 200 e rms slow speed) < 3000 e rms (low gain)	This is for a CDS. Note that kTC noise is low implying that uncorrelated reads may be the norm. Noise also reduced with pixel rate.
Frame rate	>100 Hz possible full frame > 1kHz windowing possible	Using all 64 outputs at 480 ns clock period
Exposure time	10 μs to >10s	S/H function in unit cell allows arbitrarily small integration times.
Dark current	< 5×10^3 electrons/pixel/second	This is expected to be much lower since our measurement is still dominated by instrument background and detector temperature.
Non-Linearity	-	Data taken and non linearity seen but not yet processed
Crosstalk	< 1.5% between outputs <1% possible odd-even column effect	"Ghost" images of bright pixel in one output are seen in the same relative position for all other outputs

Observing technique

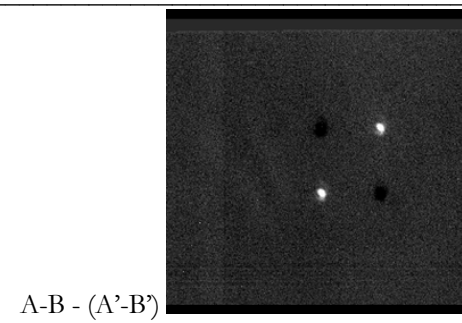
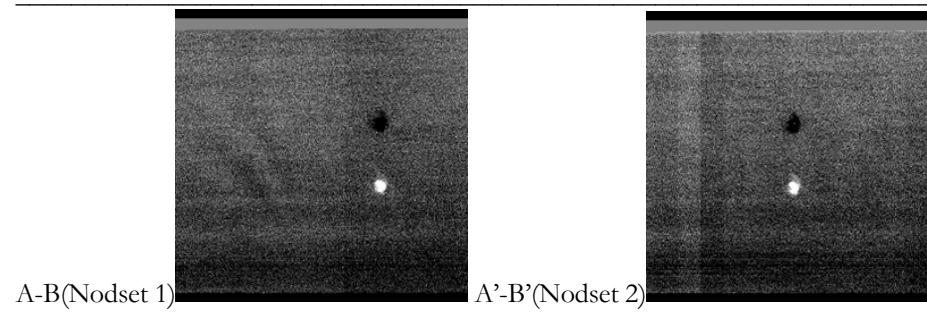
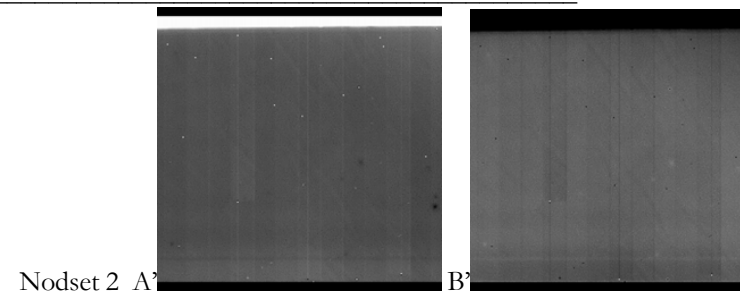
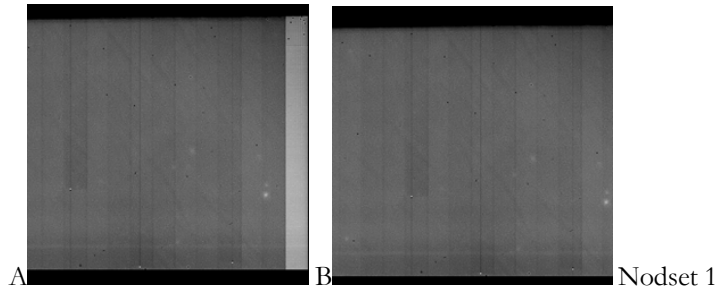
"chopping" and "nodding" techniques are needed to subtract the background to high precision. The accuracy to which the flux of an astronomical source can be obtained is basically limited by the background noise and by the " $1/f$ " noise due to variations in the background caused by temperature drifts and thin clouds.

Chopping

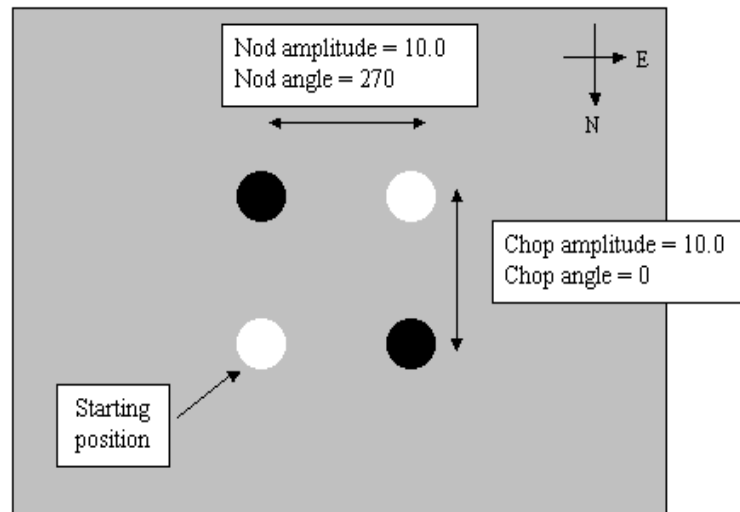
- ▶ "chopping" the telescope's secondary mirror is oscillated in a square-wave pattern at a frequency of several Hz.
- ▶ The detector alternately views two fields or "beams" on the sky: A and B beams.
- ▶ Computing $(A - B)$ cancels most, but not all, of the sky emission.

Nodding the telescope

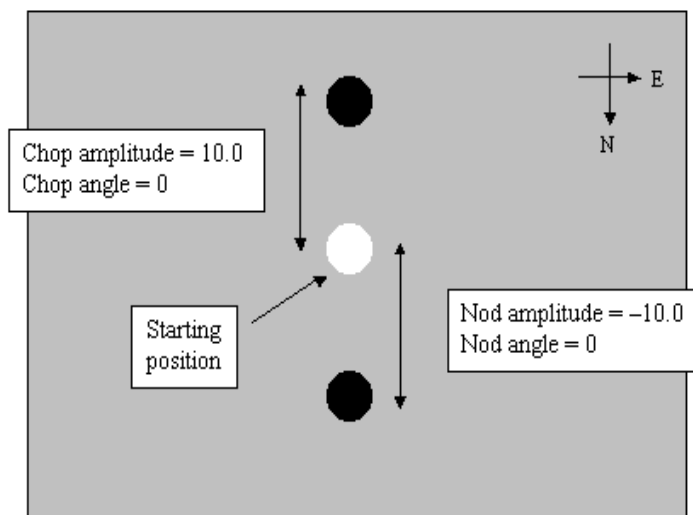
- ▶ Warm optics generates a background pattern that does not cancel out in the $A-B$ difference.
- ▶ Therefore the telescope is nodded 2-4 times a minute to move the source from the A to the B position.
- ▶ By computing $A-B$ ($A-B$) the background is properly removed.



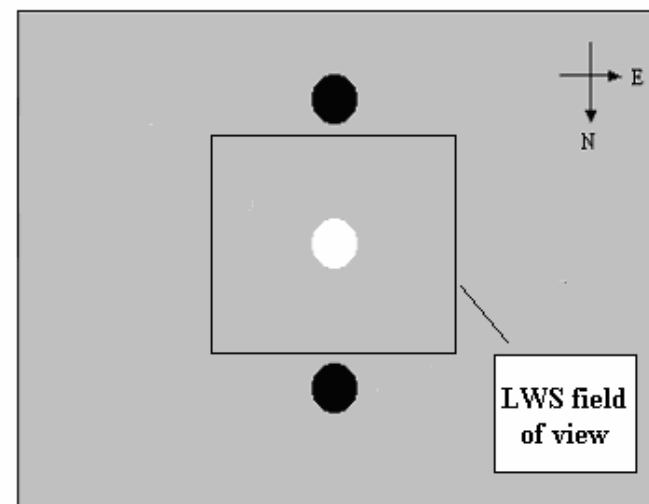
Small Source Imaging



Imaging and Spectroscopy



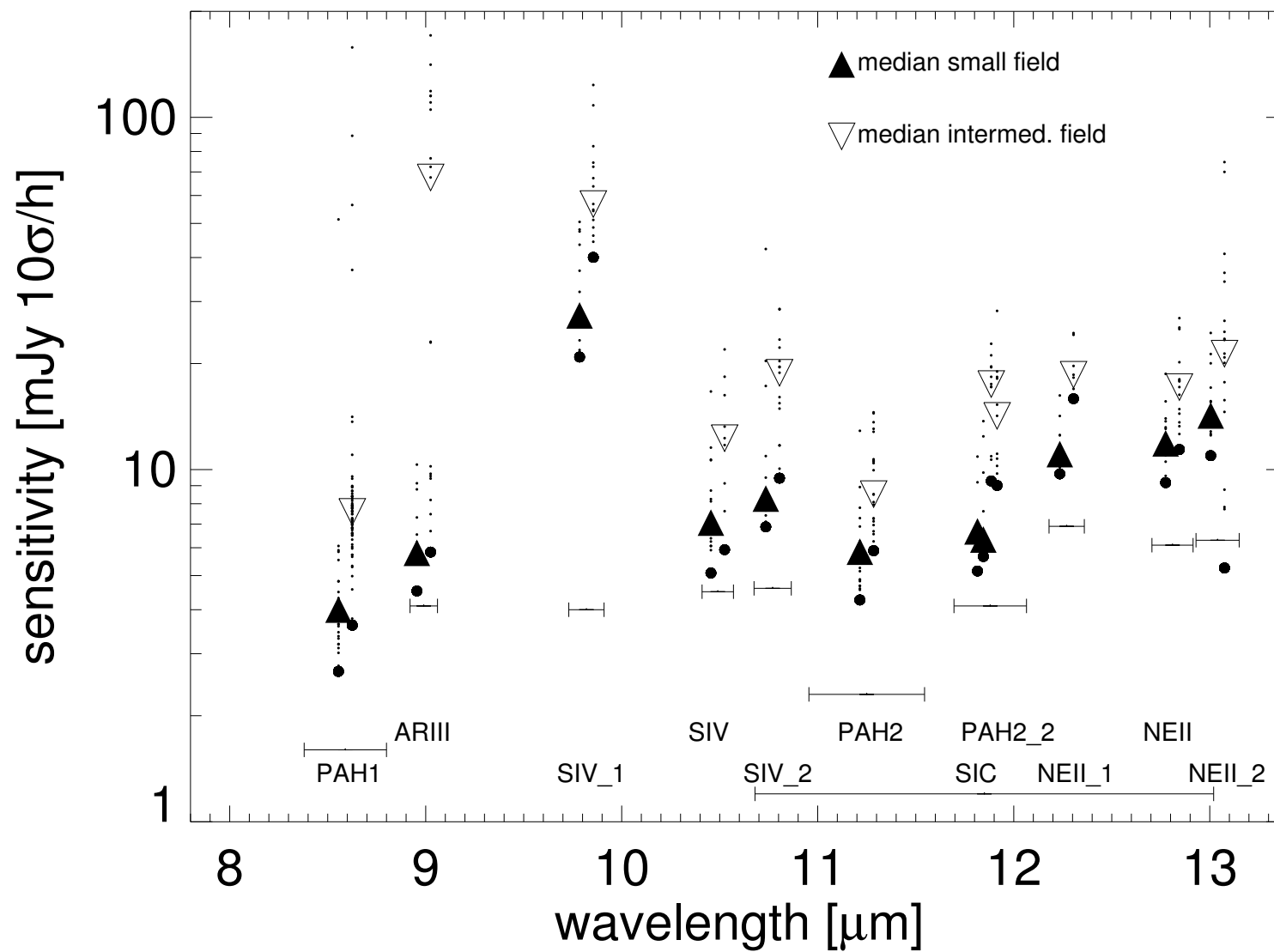
Imaging and Spectroscopy



Very short exposures

- ▶ In imaging the readout rate of the detector is high. Up to 200 frames per s are read for a minimum detector integration time of $\text{DIT} = 5 \text{ ms}$.
- ▶ During each chopping cycle the elementary exposures are added in real time and only the result is stored on disk. At a chopping frequency of $f_{\text{chop}} = 0.25 \text{ Hz}$ every $T_{\text{chop}} = 4 \text{ s}$ one VISIR image is stored as a plane in a data cube of a FITS file.

VISIR Sensitivity



Ground based observations

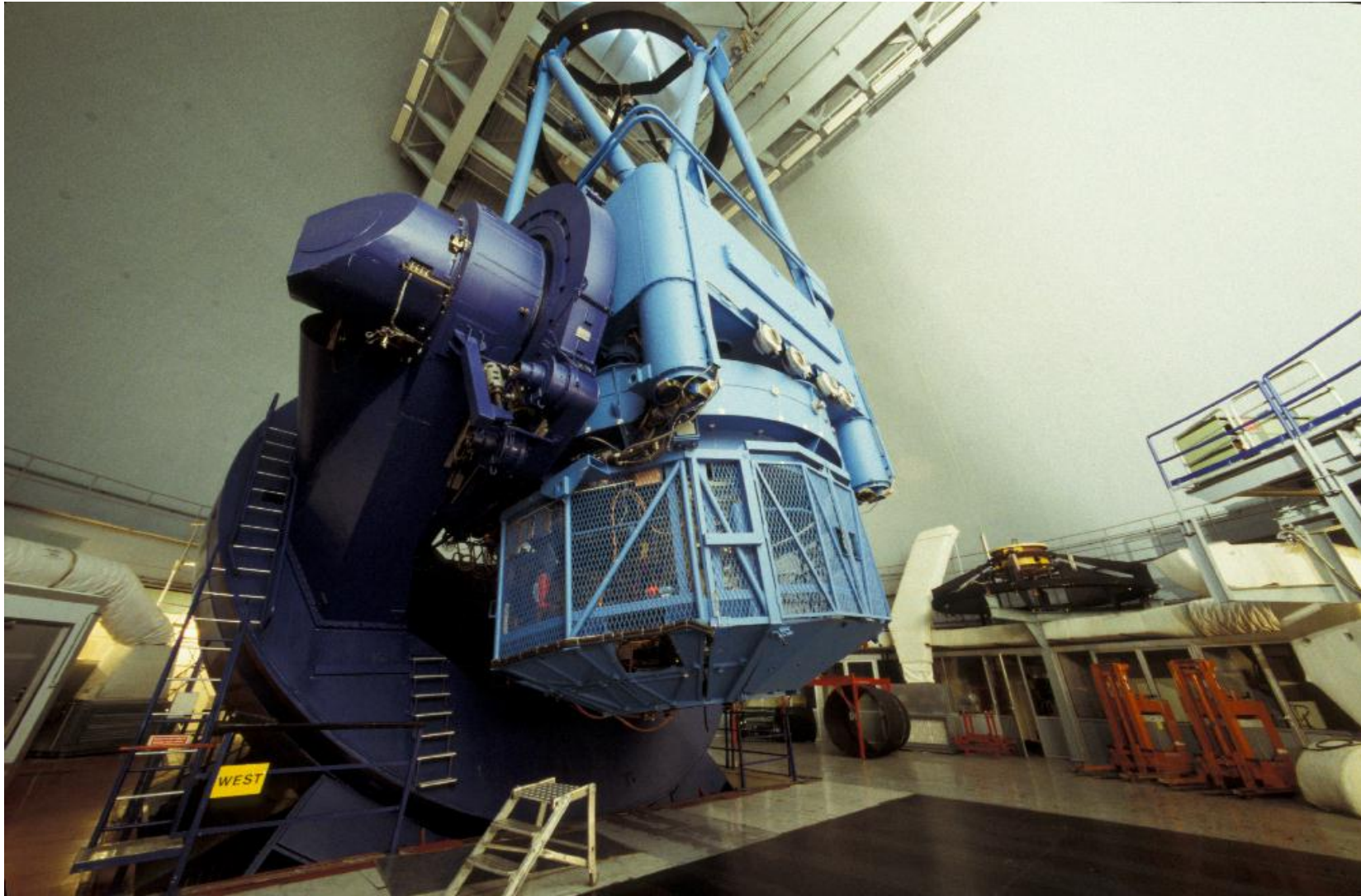
Keck - Hawaii



ESO 3.6m



3.6m ESO with f35 top ring, chopping, gold-coated M2



Space IR observatories

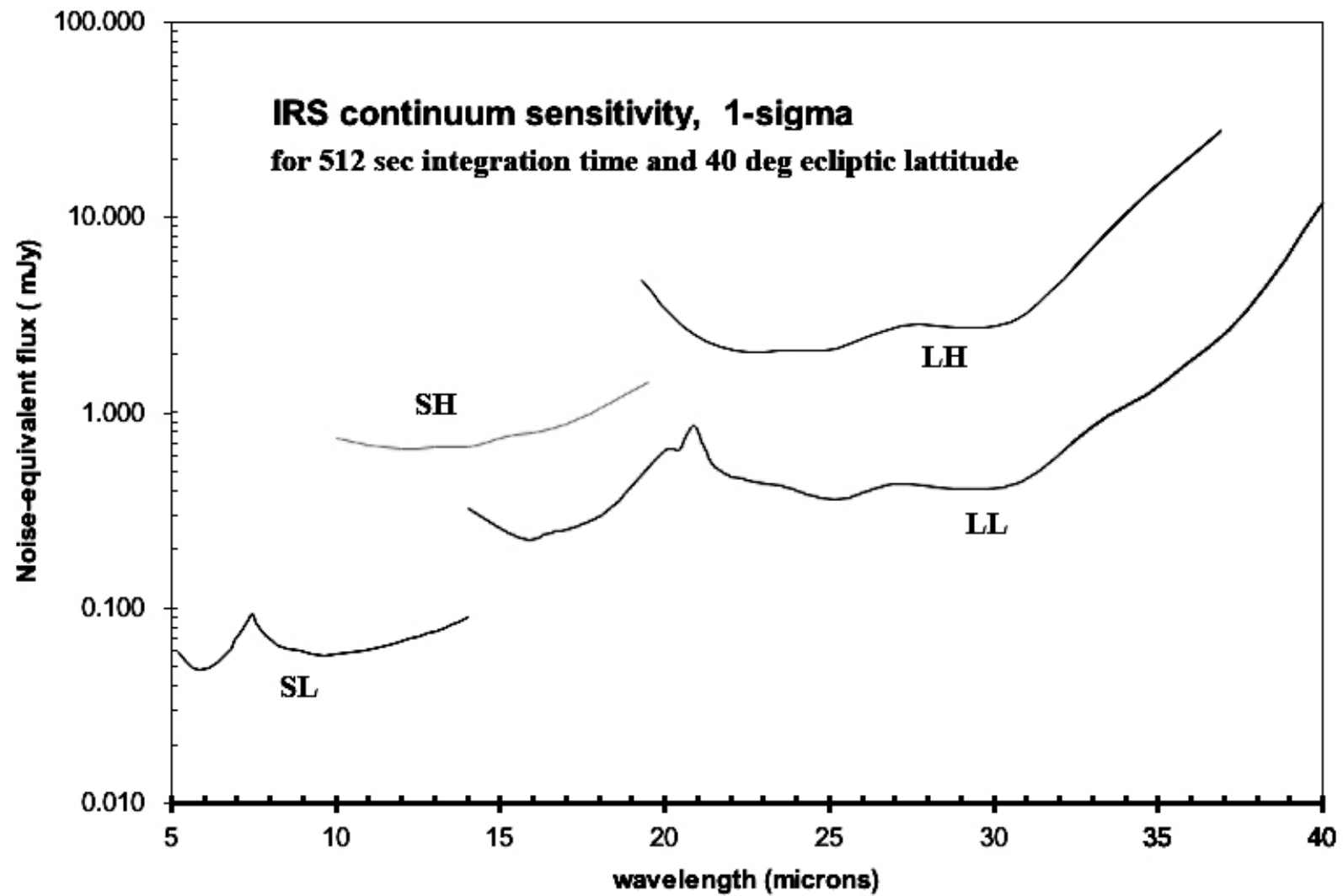
Spitzer Space Telescope

- ▶ launched in 2003.
 - ▶ IRAC (Infrared Array Camera), an infrared camera which operates simultaneously on four wavelengths (3.6, 4.5, 5.8 and 8 micron). Each module uses a 256 × 256 pixel detector; the short wavelength pair use indium antimonide technology, the long wavelength pair use arsenic-doped silicon impurity band conduction technology.
 - ▶ IRS (Infrared Spectrograph), an infrared spectrometer with four sub-modules which operate at the wavelengths 5.3-14 micron (low resolution), 10-19.5 micron (high resolution), 14-40 micron (low resolution), and 19-37 micron (high resolution).
 - ▶ MIPS (Multiband Imaging Photometer for Spitzer), three detector arrays in the far infrared (128 × 128 pixels at 24 micron, 32 × 32 pixels at 70 micron, 2 × 20 pixels at 160 micron). The 24 micron detector is identical to one of the IRS short wavelength modules. The 70 micron detector uses gallium-doped germanium technology, and the 160 micron detector also uses gallium-doped germanium.

Spitzer Space Telescope

- ▶ liquid helium supply was exhausted on 15 May 2009.
 - ▶ The two shorter wavelength bands (3.6 μ m & 4.5 μ m) of IRAC remain productive after LHe depletion, at the telescope equilibrium temperature of around 30 K, so IRAC continues to operate as the "Spitzer Warm Mission".

Spitzer Space Telescope: IRS sensitivity



The NASA WISE mission

- ▶ Radiometric data for more than 150,000 asteroids [?, ?]
- ▶ about 450 NEOs observed [?]

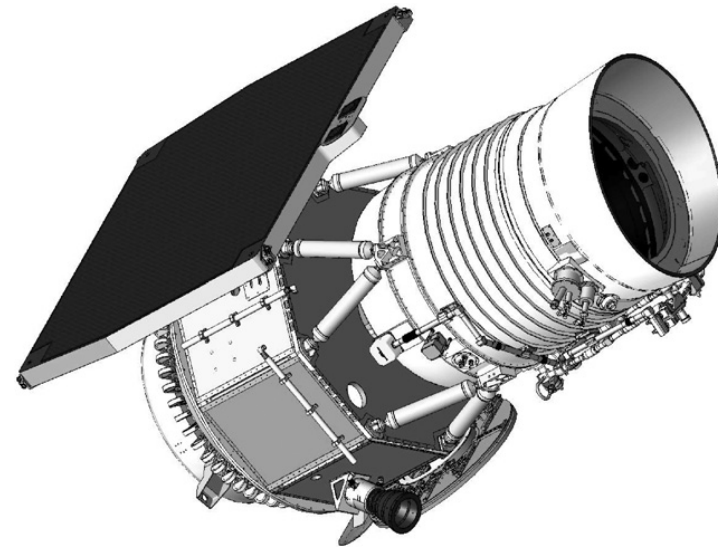


Figure 1. Diagram showing the WISE flight system in survey configuration with cover off. The spacecraft bus to the left of the bipod supports was provided by BATC, and the cryogenic instrument to the right of the bipods was provided by SDL.

WISE is in low-, above-terminator orbit



Figure 4. WISE pointing and orbit during the June solstice. Note that WISE points perpendicular to the Earth-Sun line and not toward the zenith.

Other IR space missions performing asteroid observations

- ▶ Akari (JAXA)
- ▶ ISO (ESA)
- ▶ IRAS (NASA)

Stratospheric Observatories

SOFIA - Stratospheric Observatory for Infrared Astronomy

www.sofia.usra.edu



Detection

$$N = \frac{1}{hc} \int_{-\infty}^{+\infty} f(\lambda) \lambda R(\lambda) d\lambda \quad (18)$$

where N number of photon-electrons in the unit time, unit area (in the filter band); $f(\lambda)$ = SED = monochromatic flux density [$\text{W}/\text{m}^2/\mu\text{m}$]; and with:

$$R(\lambda) = R_{\text{filter}}(\lambda) \times R_{\text{optics}}(\lambda) \times R_{\text{atmosphere}}(\lambda) \quad (19)$$

If $f(\lambda)$ and $R(\lambda)$ are continuous and $R(\lambda)$ is non negative, for the theorem of the average value for integration, there is a value of λ that we call **isophotal wavelength λ_{ISO}** such that:

$$f(\lambda_{ISO}) = \langle F \rangle = \frac{\int_{-\infty}^{+\infty} f(\lambda) \lambda R(\lambda) d\lambda}{\int_{-\infty}^{+\infty} \lambda R(\lambda) d\lambda} \quad (20)$$

Example: WISE filters $R(\lambda)$

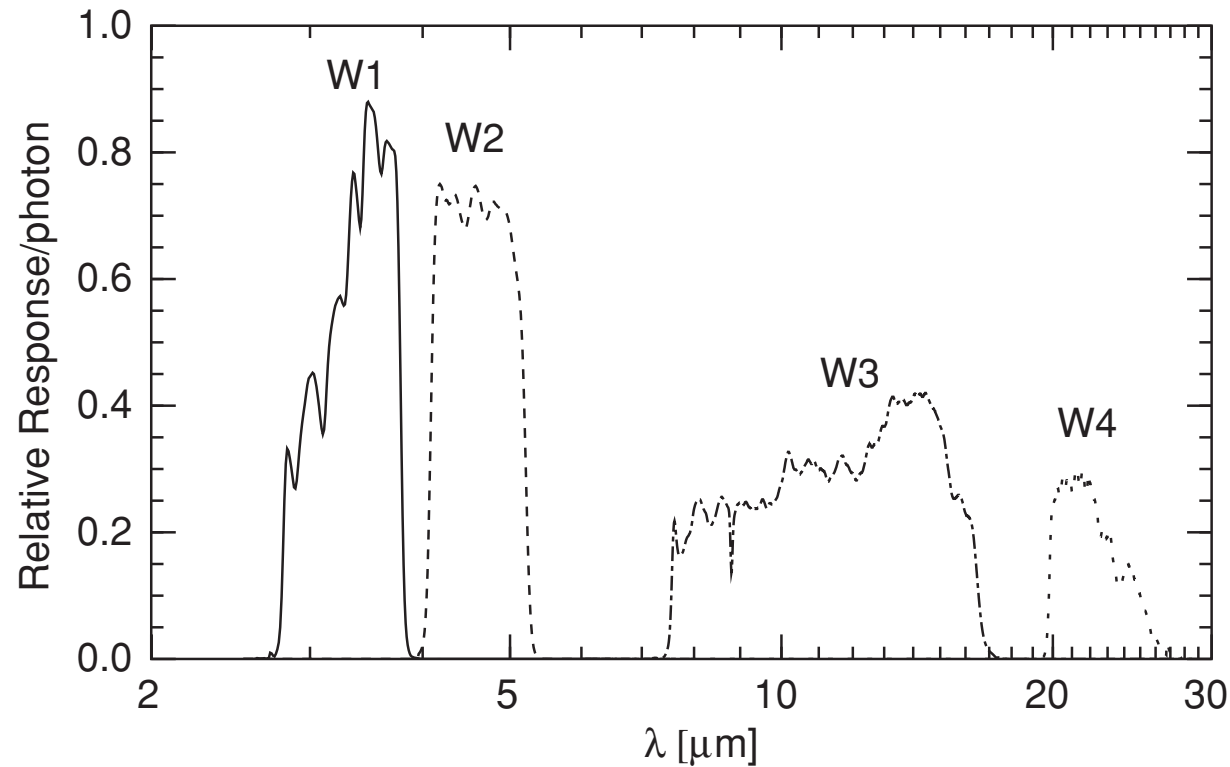


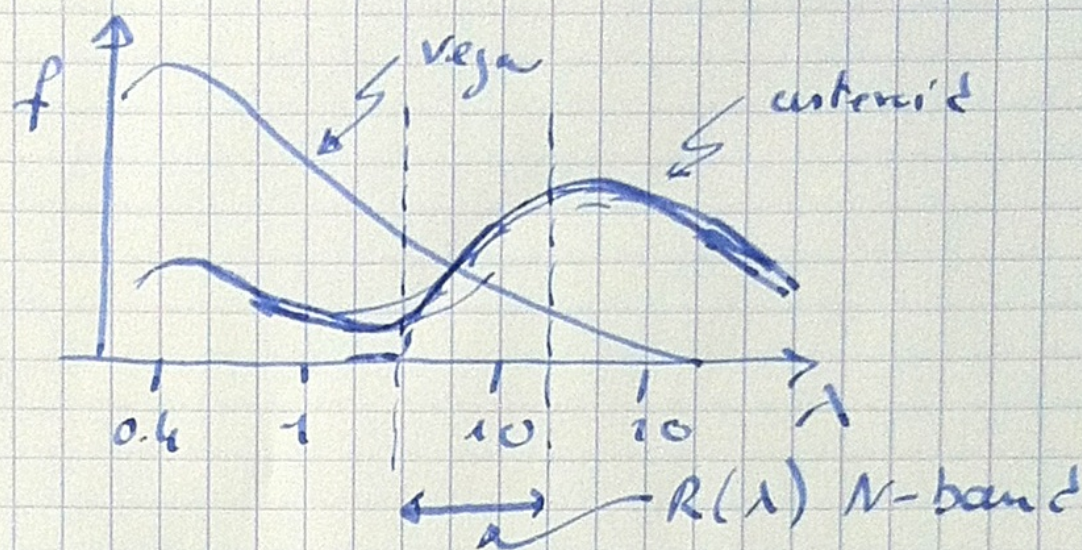
Figure 6. Weighted mean WISE relative spectral response functions in electrons per photon.

The isophotal wavelengths so defined are 3.3526, 4.6028, 11.5608, and 22.0883 microns for W1,..., W4. [?]

The ratio $\frac{N}{N_{\text{vega}}} = \frac{f(\lambda)}{f_{\text{vega}}(\lambda)}$

only if $f(\lambda)$ and $f_{\text{vega}}(\lambda)$ have the same behavior.

But $f(\lambda)$ of asteroids VERY different from $f_{\text{vega}}(\lambda)$



$$\begin{aligned}
 \frac{N}{N^{\text{vega}}} &= \frac{\frac{1}{hc} \int_{-\infty}^{\infty} f(\lambda) \lambda R(\lambda) d\lambda}{\frac{1}{hc} \int_{-\infty}^{\infty} f^{\text{vega}}(\lambda) \lambda R(\lambda) d\lambda} = \frac{\int_{-\infty}^{\infty} f(\lambda) \lambda R(\lambda) d\lambda}{f^{\text{vega}}(\lambda_{\text{iso}}) \int_{-\infty}^{\infty} \lambda R(\lambda) d\lambda} \\
 &= \frac{f(\lambda_{\text{iso}})}{f^{\text{vega}}(\lambda_{\text{iso}})} \times \underbrace{\frac{\int_{-\infty}^{\infty} \frac{f(\lambda)}{f(\lambda_{\text{iso}})} \lambda R(\lambda) d\lambda}{\int_{-\infty}^{\infty} \lambda R(\lambda) d\lambda}}
 \end{aligned}$$

It depends on the behaviour of $f(\lambda)$
and this term is called color
correction

in the end:

$$\frac{N}{N^{\text{vega}}} = \frac{f(\lambda_{\text{iso}})}{f^{\text{vega}}(\lambda_{\text{iso}})} \times C_c$$

$$f(\lambda_{ISO}) = \frac{N}{N^{Vega}} f^{Vega}(\lambda_{ISO}) / C_C \quad (21)$$

C_C for WISE filters for Power Laws and Blackbodies

F_ν	$f_c(W1)$	$f_c(W2)$	$f_c(W3)$	$f_c(W4)$
ν^3	1.0283	1.0206	1.1344	1.0142
ν^2	1.0084	1.0066	1.0088	1.0013
ν^1	0.9961	0.9976	0.9393	0.9934
ν^0	0.9907	0.9935	0.9169	0.9905
ν^{-1}	0.9921	0.9943	0.9373	0.9926
ν^{-2}	1.0000	1.0000	1.0000	1.0000
ν^{-3}	1.0142	1.0107	1.1081	1.0130
ν^{-4}	1.0347	1.0265	1.2687	1.0319
$B_\nu(100)$	17.2062	3.9096	2.6588	1.0032
$B_\nu(141)$	4.0882	1.9739	1.4002	0.9852
$B_\nu(200)$	2.0577	1.3448	1.0006	0.9833
$B_\nu(283)$	1.3917	1.1124	0.8791	0.9865
$B_\nu(400)$	1.1316	1.0229	0.8622	0.9903
$B_\nu(566)$	1.0263	0.9919	0.8833	0.9935
$B_\nu(800)$	0.9884	0.9853	0.9125	0.9958
$B_\nu(1131)$	0.9801	0.9877	0.9386	0.9975
K2V	1.0038	1.0512	1.0030	1.0013
G2V	1.0049	1.0193	1.0024	1.0012

Calibration from the ground

the issue: $R_{ATMOSPHERE}(\lambda)$ is temporally and spatially very variable

Photometric standards are observed as much as possible and as close as possible in time and space to the science source.

It is also common practice to use:

$$f(\lambda_{ISO}) = \frac{N}{N_S} \times f_S(\lambda_{ISO}) / C_C \quad (22)$$

For narrow band filters (width $\sim 1\mu m$) C_C is close to one and it is often omitted.

Filter name	Black body temperature (K)									
	100	150	200	250	300	350	400	450	500	550
L	0.79	0.95	1.00	1.02	1.02	1.02	1.02	1.02	1.02	1.02
M	0.80	0.95	1.00	1.02	1.02	1.02	1.02	1.02	1.02	1.01
N1	0.98	1.02	1.03	1.02	1.02	1.01	1.01	1.00	1.00	1.00
N2	1.00	1.03	1.02	1.02	1.01	1.00	1.00	1.00	0.99	0.99
N7.9	1.00	1.02	1.02	1.02	1.01	1.01	1.01	1.00	1.00	1.00
N8.9	1.01	1.02	1.02	1.01	1.01	1.01	1.00	1.00	1.00	1.00
N9.8	1.02	1.02	1.02	1.01	1.01	1.00	1.00	1.00	1.00	1.00
N10.4	1.02	1.02	1.02	1.01	1.01	1.00	1.00	1.00	1.00	0.99
N11.9	1.02	1.02	1.01	1.01	1.00	1.00	1.00	0.99	0.99	0.99
SiC	1.00	1.03	1.03	1.02	1.01	1.00	1.00	0.99	0.99	0.98
N12.9	1.02	1.02	1.01	1.01	1.00	1.00	1.00	0.99	0.99	0.99
[NeII]	1.01	1.00	1.00	1.00	1.00	1.00	1.00	1.00	1.00	1.00
Q1	1.01	1.00	1.00	1.00	1.00	1.00	1.00	1.00	1.00	1.00

Table B-6 Color correction factors calculated for TIMMI2 filters assuming a window transmission function which limits were defined at the 50% level of the actual filters transmission (see Table B-4).

HD	L (Jy)	M (Jy)	N7.9 (Jy)	N1 (Jy)	N8.9 (Jy)	N9.8 (Jy)	N10.4 (Jy)	N11.9 (Jy)	N12.9 (Jy)	Q1 (Jy)	Q2 (Jy)
WEL	3.84	4.72	7.72	8.58	8.64	9.49	10.24	11.56	12.20	17.75	18.75
HD1522	112.64	61.08	29.46	23.90	23.56	19.96	17.59	13.81	12.34	5.91	5.29
HD4128	322.81	194.18	85.60	69.61	68.69	57.57	49.52	39.44	35.30	16.97	15.22
HD6805	118.93	64.50	31.11	25.23	24.88	21.08	18.58	14.58	13.03	6.24	5.59
HD12929	481.19	244.19	122.27	99.73	98.54	85.15	75.30	59.99	53.91	25.77	23.52
HD29139	3960.	2063.72	963.02	776.43	768.26	672.82	604.06	491.13	438.51	207.77	187.45
HD29291	54.69	32.41	14.79	12.06	11.92	9.92	8.56	6.78	6.10	2.92	2.62
HD32887	334.74	174.38	81.38	65.61	64.92	56.86	51.04	41.50	37.06	17.56	15.84
HD37160	56.61	34.05	15.01	12.20	12.04	10.09	8.68	6.91	6.19	2.98	2.67
HD47105	43.47	29.61	11.60	9.45	9.29	7.74	6.65	5.23	4.74	2.27	2.03
HD81420	41.51	21.63	10.09	8.14	8.05	7.05	6.33	5.15	4.60	2.18	1.96
HD81797	833.22	436.78	198.27	160.55	158.03	141.19	128.76	100.57	90.34	43.14	38.69
HD108903	0.	2662.	1403.	1102.	1088.94	927.37	866.04	708.55	619.00	296.69	267.41
HD110458	32.68	19.66	8.66	7.05	6.95	5.83	5.01	3.99	3.57	1.72	1.54
HD123139	334.07	200.98	88.58	72.04	71.09	59.56	51.26	40.81	36.53	17.57	15.75
HD124897	4361.	2159.	1109.52	905.65	891.29	770.92	681.71	534.89	486.83	231.89	208.86
HD133774	71.98	37.51	17.51	14.11	13.96	12.23	10.98	8.93	7.97	3.78	3.41
HD156277	43.71	23.78	11.52	9.20	9.06	7.63	6.74	5.35	4.81	2.31	2.07
HD169916	182.33	98.88	47.70	38.71	38.13	32.32	28.48	22.35	19.98	9.56	8.56
HD175775	113.30	61.44	29.64	24.04	23.70	20.08	17.70	13.89	12.42	5.94	5.32
HD178345	67.04	40.33	17.78	14.46	14.26	11.96	10.29	8.19	7.33	3.53	3.16
HD187642	200.24	136.74	53.35	43.41	42.88	35.64	30.72	24.28	21.81	10.41	9.34
HD189831	68.57	35.72	16.67	13.44	13.30	11.65	10.46	8.50	7.59	3.60	3.24
HD196171	122.18	73.50	32.39	26.35	25.99	21.79	18.74	14.92	13.36	6.42	5.76

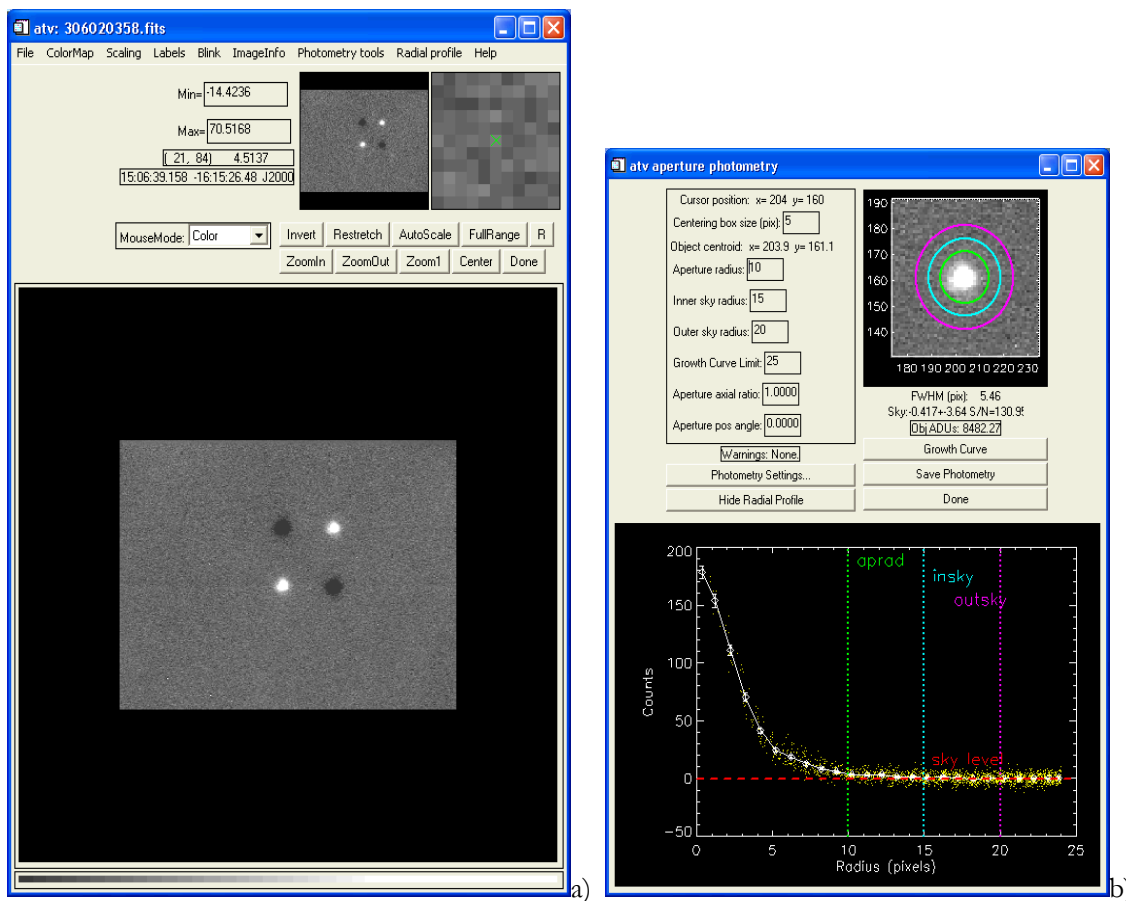
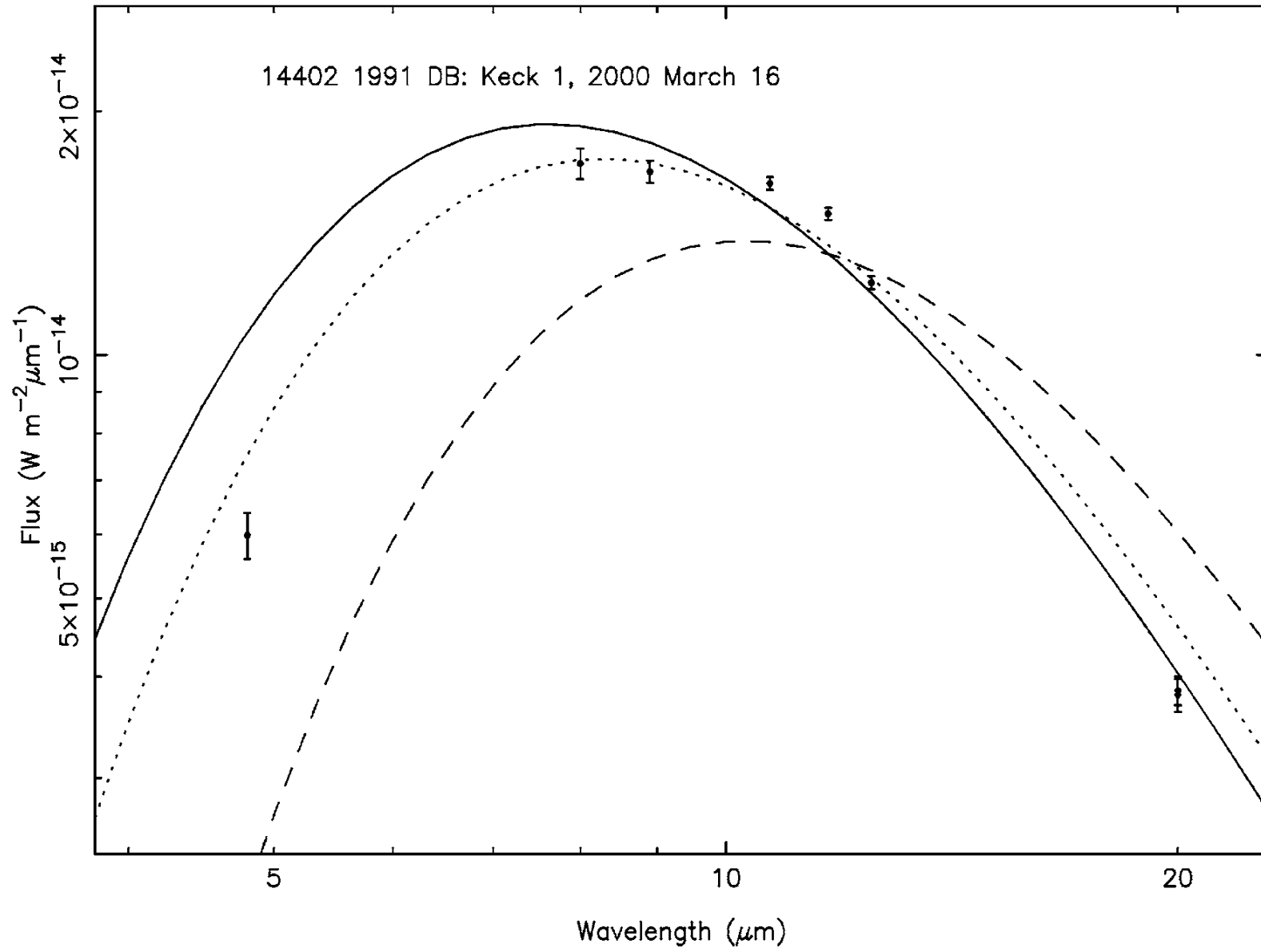


Fig. 3.4 The ATV tool: on the left (a), ATV shows a mid-IR image of a standard star obtained with the TIMMI2 at the ESO 3.6 m telescope. On the right (b), the ATV aperture photometry plug-in used to analyze one of the four chop-nod channels.



[?]

Ground based spectroscopy

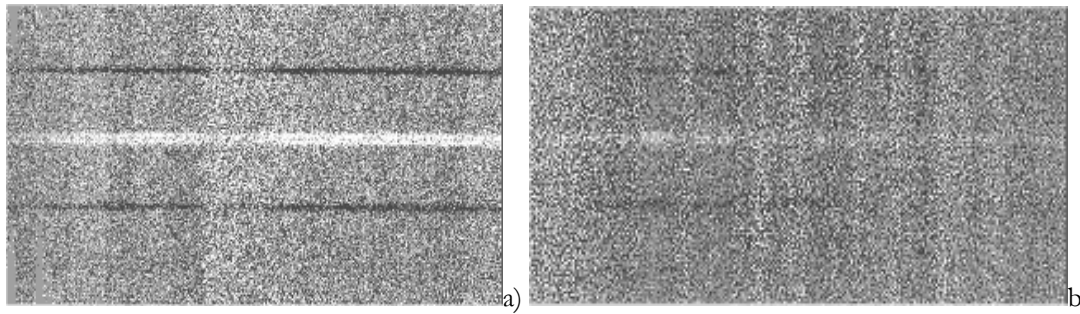


Fig. 2.1 N-band a) and Q-band b) spectra of the thermal infrared emission of the near-earth asteroid 5587 (1990SB) observed on April 09, 2001 with the TIMMI2 installed at the 3.6m telescope, La Silla, ESO (Chile). This asteroid has a diameter of almost 4km.

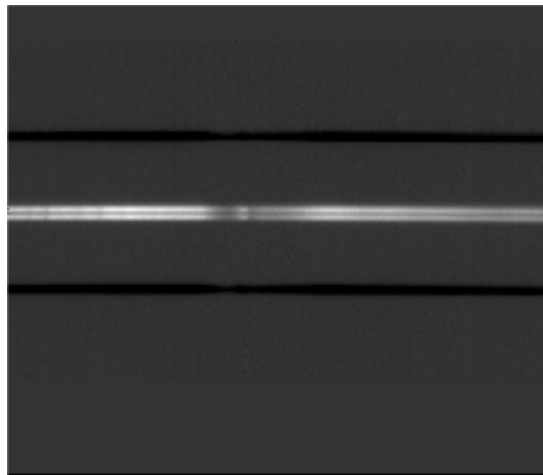


Fig. 3.8 Raw image of the N-band spectrum of the standard star HD123139 observed with the ESO 3.6m telescope and TIMMI2

Ground based spectroscopy

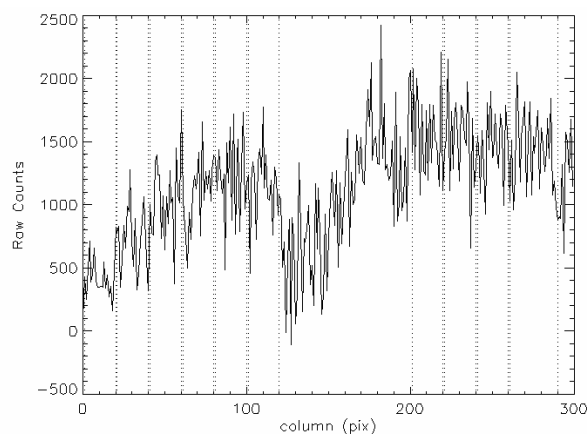


Fig. 3.11 N-band raw spectrum of the NEA 5587. Dotted vertical lines are drawn in correspondence to the bin extremes. The binning intervals were taken at the following detector columns (1 20), (21 40), (41 60), (61 80), (81 100), (101 120), (201 220), (221 240), (241 260), (261 290).

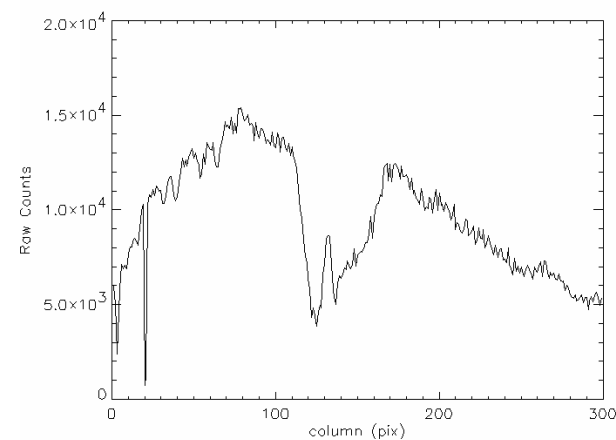


Fig. 3.10 Raw extracted spectrum of the standard star HD123139. Note the characteristic ozone feature between pixels 110-190

Ground based spectroscopy

$$f(\lambda) = \frac{N(\lambda)}{N_S(\lambda)} \times f_S(\lambda) \quad (23)$$

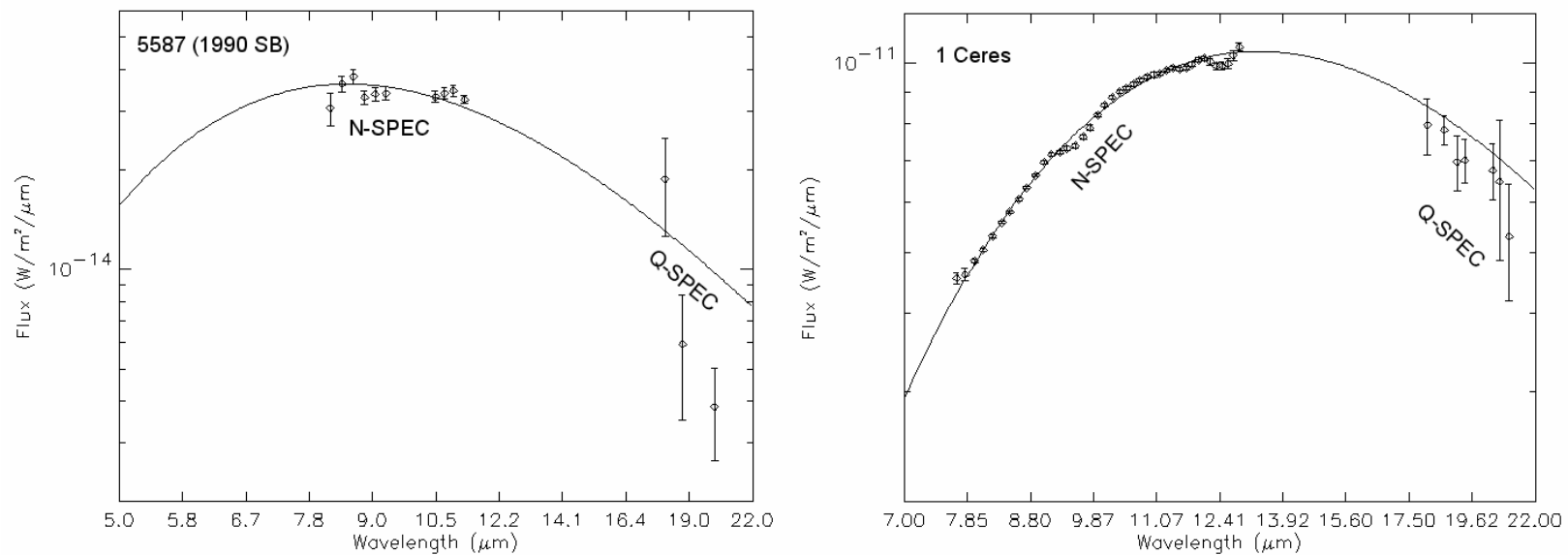


Fig. 2.2 Observed thermal infrared fluxes of the NEA 5587 on the left and of the largest asteroid 1 Ceres. Note the noise affecting Q-band data which have been binned for increasing the signal to noise ratio. Continuous line is a black body fit to the infrared spectra.

Spitzer spectroscopy

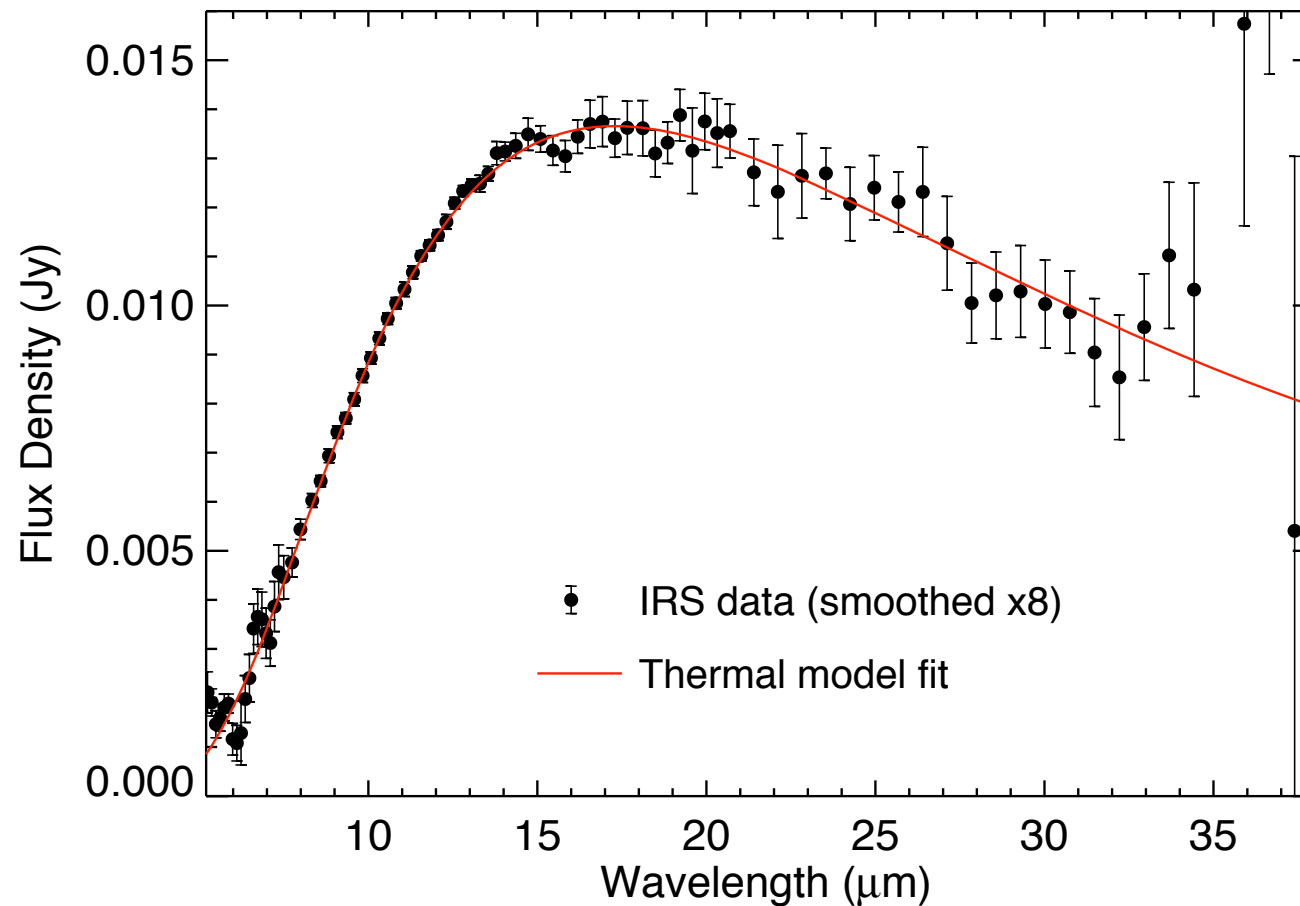


Figure 1. IRS spectrum of 1999 RQ₃₆ binned by a factor of 8 and fit with a thermophysical model. The model fit suggests thermal inertia $\sim 600 \text{ J m}^{-2} \text{ s}^{-1/2} \text{ K}^{-1}$ and diameter of $\sim 610 \text{ m}$ (giving $p_V \sim 0.03$).

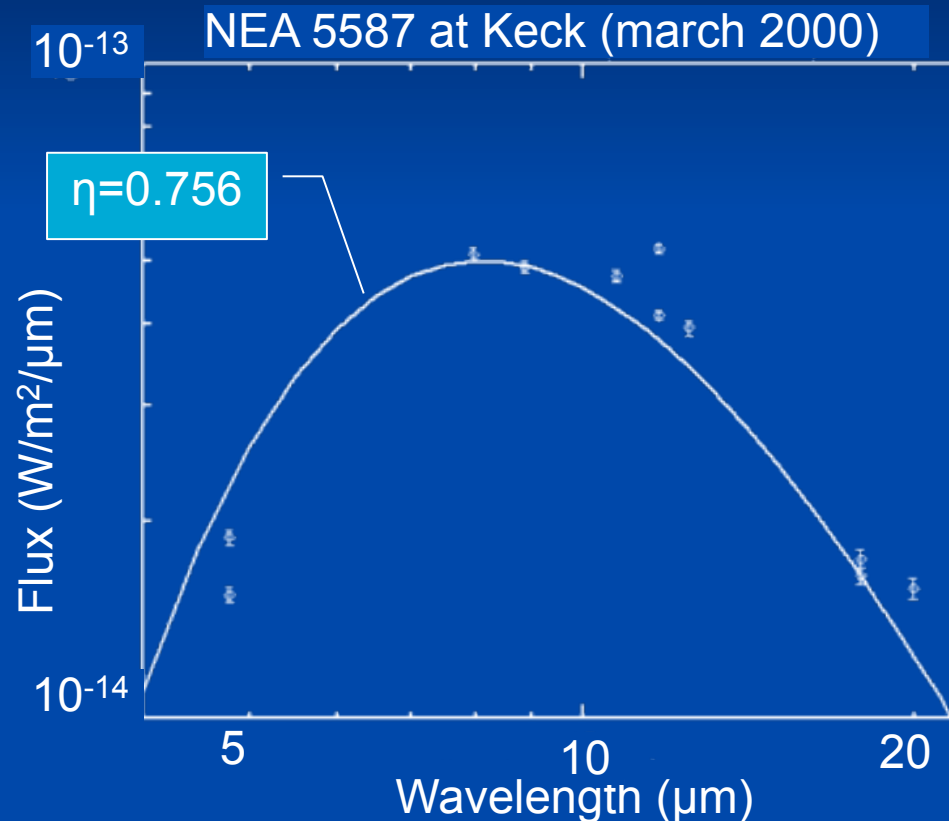
Thermal Models

Models of the temperature distribution on the surface of air-less bodies.

- ▶ Analytical
- ▶ Numerical

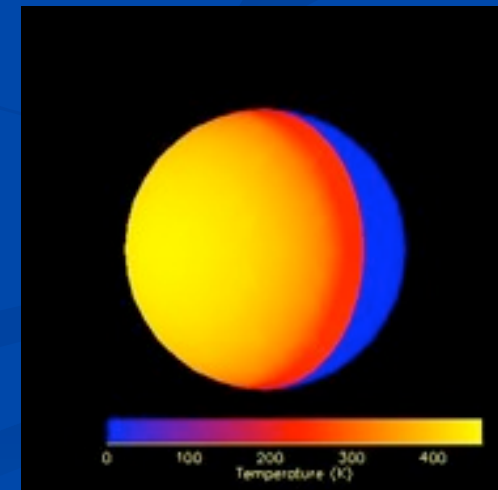
Near-Earth Asteroid Thermal Model (the NEATM, Harris,

- Spherical shape
- Temperature



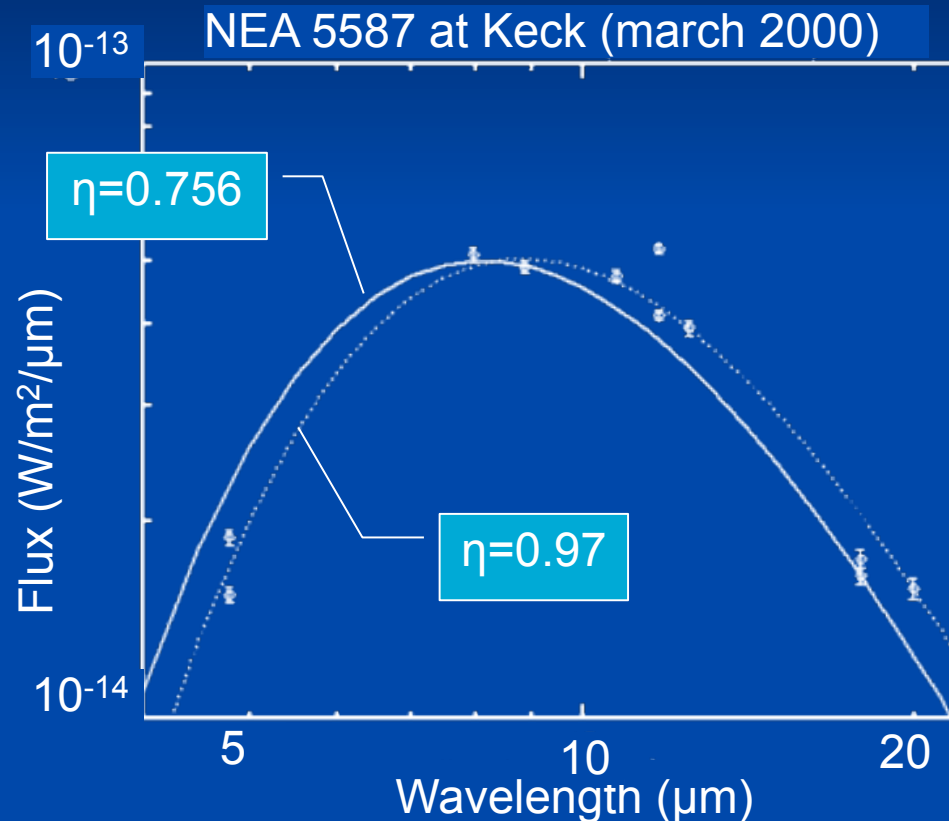
$$T(\psi) = \begin{cases} T_{SS} \times \cos^{1/4}\psi & \text{for } (0 \leq \psi \leq \pi/2) \\ 0 & \text{otherwise} \end{cases}$$

$$T_{SS} = \left[\frac{S_{\odot}}{r^2} \times \frac{(1-A)}{\epsilon\sigma\eta} \right]^{1/4}$$



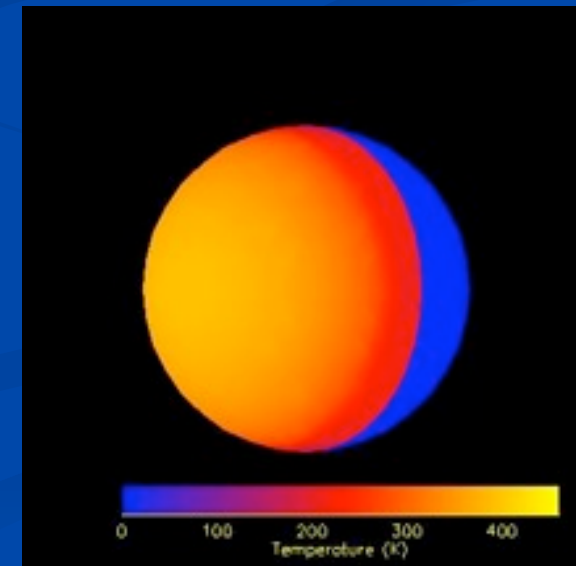
Near-Earth Asteroid Thermal Model (the NEATM, Harris,

- Spherical shape
- Temperature



$$T(\psi) = \begin{cases} T_{SS} \times \cos^{1/4}\psi & \text{for } (0 \leq \psi \leq \pi/2) \\ 0 & \text{otherwise} \end{cases}$$

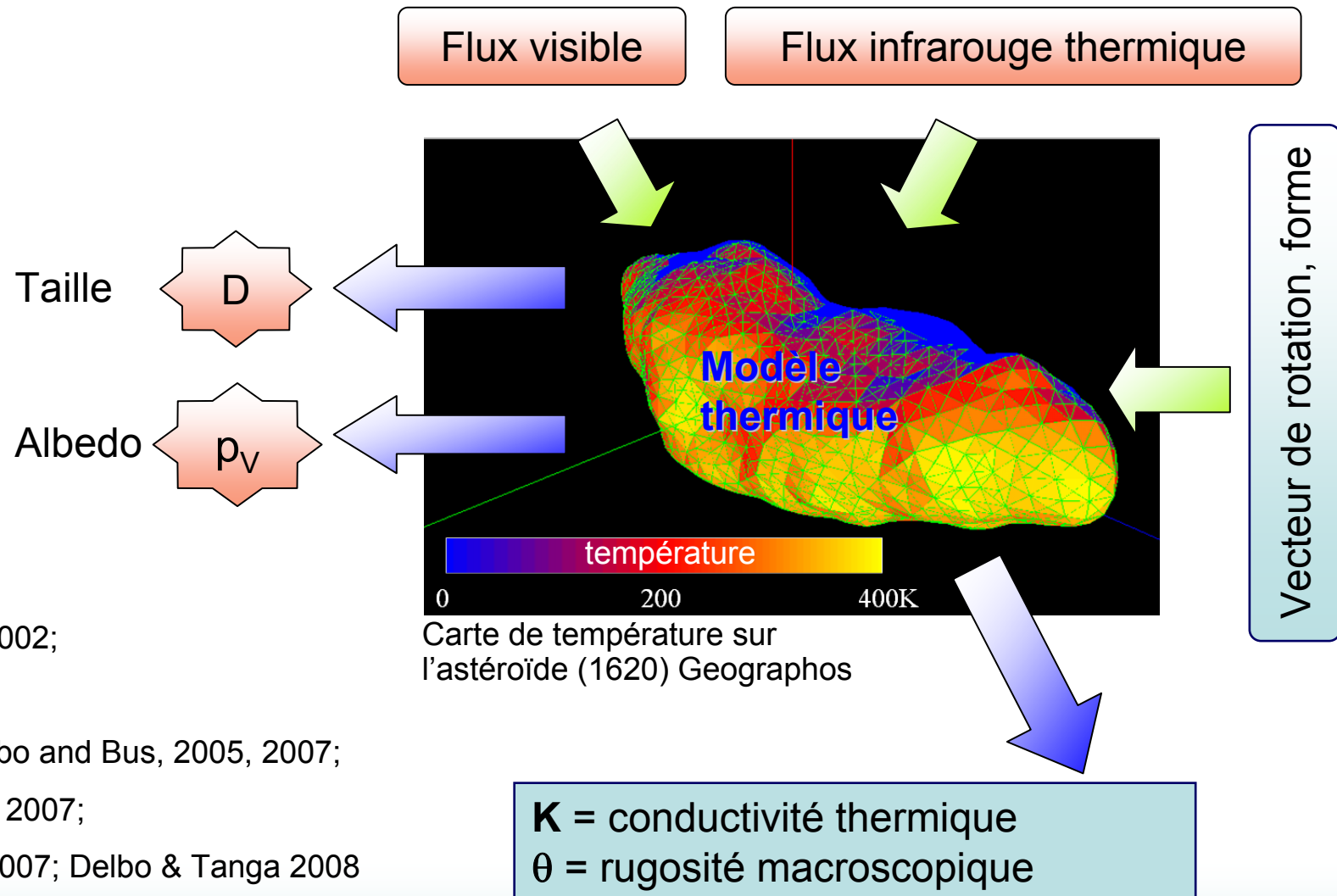
$$T_{SS} = \left[\frac{S_{\odot}}{r^2} \times \frac{(1-A)}{\epsilon\sigma\eta} \right]^{1/4}$$



Surface properties of NEAs and η

- In the NEATM, η takes account of effects that alter the surface temp. distribution with respect to that of the standard thermal model ($\eta=1$), mainly:
- Thermal Inertia
 - a measure of a material's thermal response to the diurnal heating cycle. (higher thermal inertia $\rightarrow \eta > 1$)
- Macroscopic surface roughness
 - e.g. cratering (higher degree of roughness $\rightarrow \eta < 1$)

Modèles thermiques des astéroïdes: détermination des tailles, albedos, et propriétés à la surface



Références:

Delbo and Harris, 2002;
Delbo, 2004;
Harris, Mueller, Delbo and Bus, 2005, 2007;
Muller, Delbo, et al. 2007;
Delbo et al. 2003, 2007; Delbo & Tanga 2008

Thermophysical Model Components

- ▶ 1D heat diffusion (parameter: $\Gamma = \sqrt{\kappa \rho C}$):

$$\frac{\partial T(X,t)}{\partial t} = \omega \frac{\partial^2 T(X,t)}{\partial X^2}$$

- ▶ Boundary conditions:

- ▶ no heat flux towards the nucleus: $\sqrt{\omega} \Gamma \left(\frac{\partial T(X,t)}{\partial X} \right)_{X=d} = 0$

- ▶ at the surface:

$$\sqrt{\omega} \Gamma \left(\frac{\partial T(X,t)}{\partial X} \right)_{X=0} = \epsilon \sigma T^4(0,t) - (1 - A_k)(1 - S_k) \frac{S_{\odot}}{r^2} \mu_k(t)$$

- ▶ Craters (parameters: surface density, opening angle)

- ▶ 1D heat diffusion

- ▶ Boundary conditions:

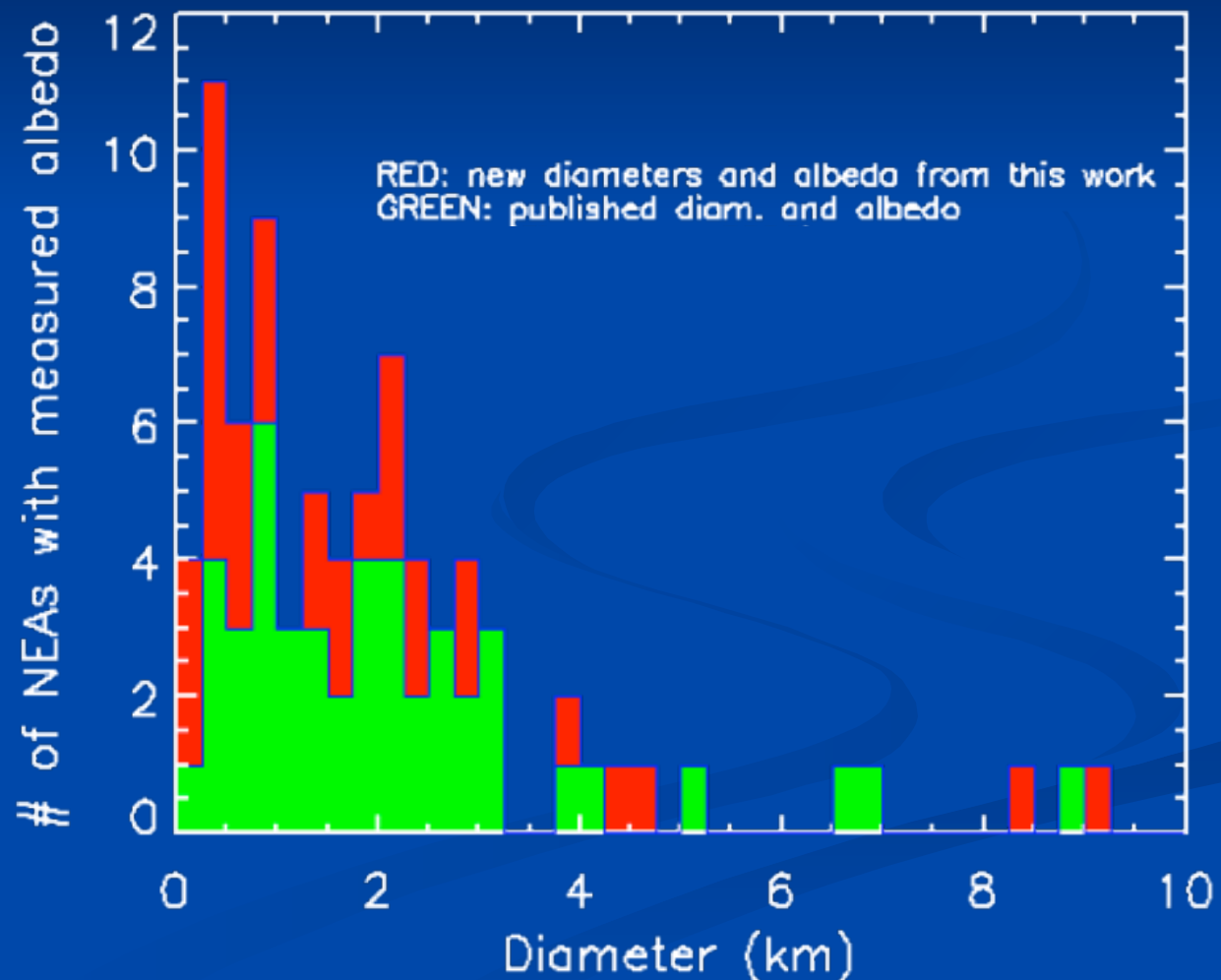
- ▶ no heat flux towards the nucleus

- ▶ at the surface:
$$\sqrt{\omega} \Gamma \left(\frac{\partial T_i(X_i,t)}{\partial X_i} \right)_{X_i=0} = \epsilon \sigma T_i^4(0,t) - (1 - A_i)(1 - S_i) \frac{S_{\odot}}{r^2} \mu_i(t) - \epsilon \sigma \sum_{j \neq i} f_{ij} T_j^4(0,t) \cos \beta_{ij} - E_{ref}(0,t)$$

Scientific relevance of this work

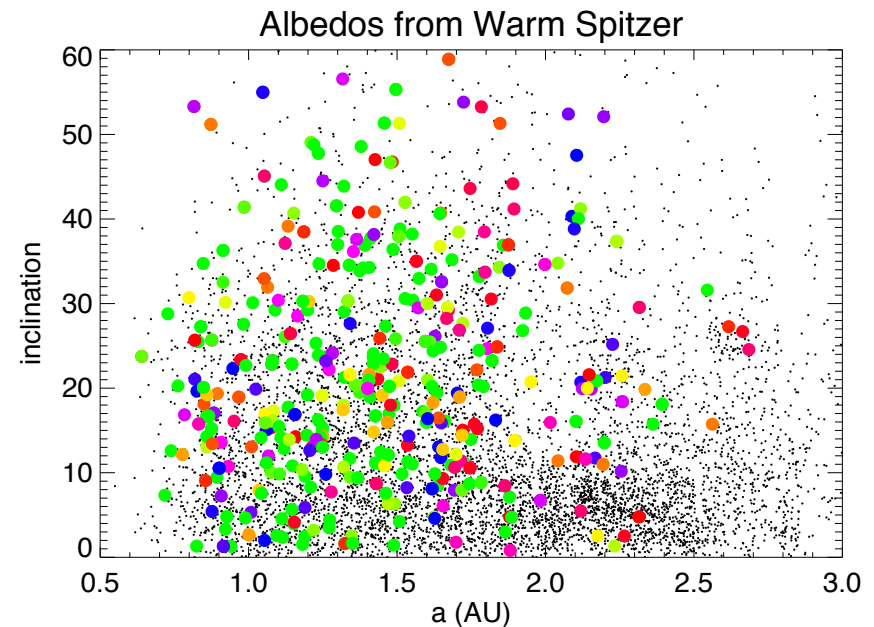
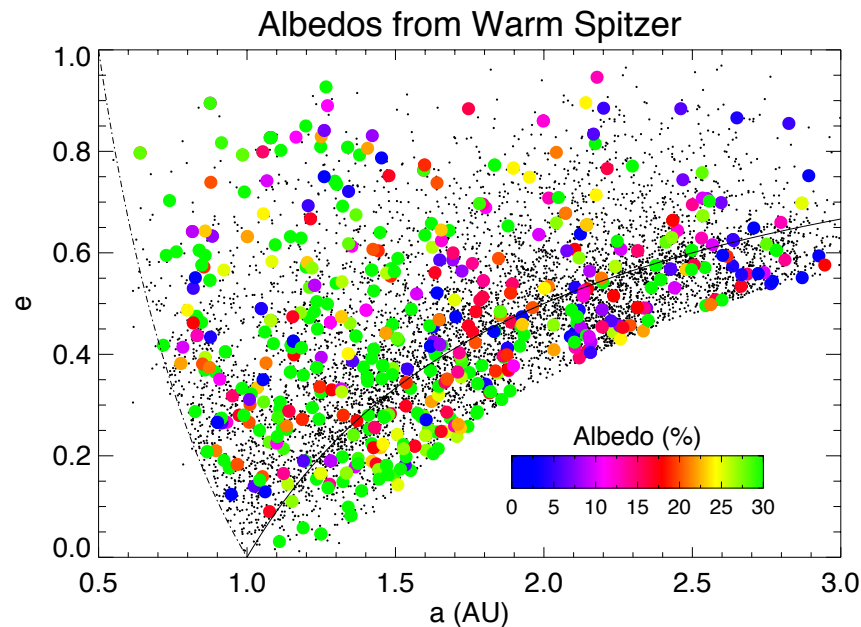
This work increments the number of NEAs with measured sizes and albedos by 54%.

We have more than doubled the number of subkilometer-NEAs with measured size and albedos.



Near-Earth Objects (NEOs) albedos

Orbital plots of known NEOs, color coded according to albedo data from ExploreNEOs PI D. Trilling (June 2011)



Thermal Physics of Asteroids (3rd lesson)

Charles University of Prague – Oct/Nov 2011

Marco Delbo

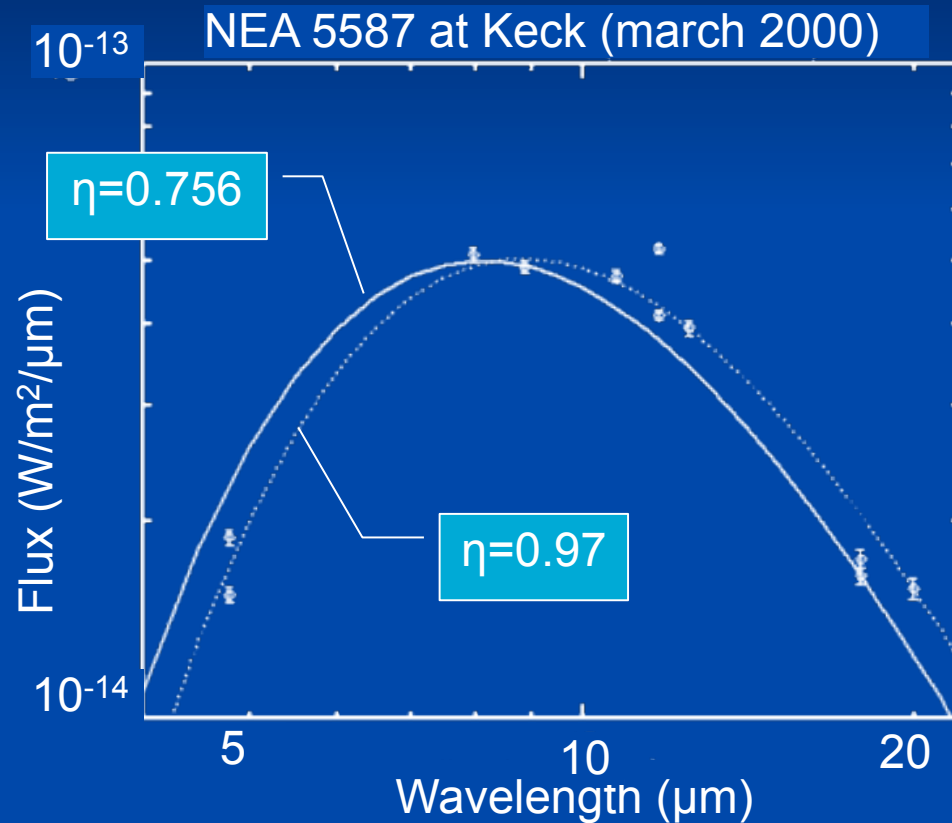
UNS-CNRS-Observatoire de la Côte d'Azur

Visiting: Astronomical Institute of the Charles University, Prague, CZ

November 2, 2011

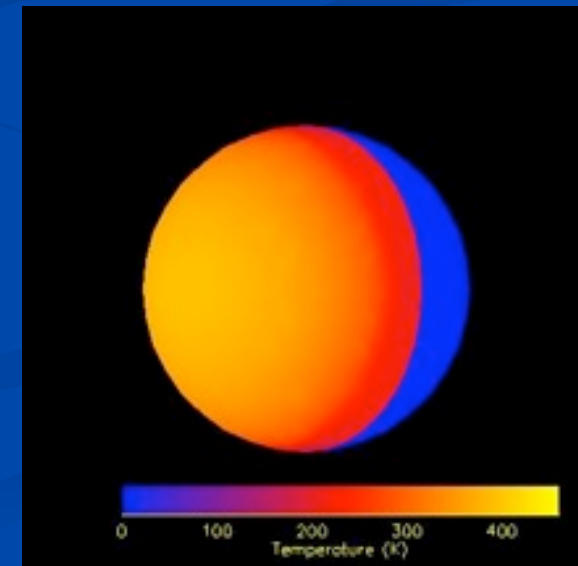
Near-Earth Asteroid Thermal Model (the NEATM, Harris,

- Spherical shape
- Temperature



$$T(\psi) = \begin{cases} T_{SS} \times \cos^{1/4} \psi & \text{for } (0 \leq \psi \leq \pi/2) \\ 0 & \text{otherwise} \end{cases}$$

$$T_{SS} = \left[\frac{S_{\odot}}{r^2} \times \frac{(1-A)}{\epsilon \sigma \eta} \right]^{1/4}$$



Asteroid Thermo-Physical Models

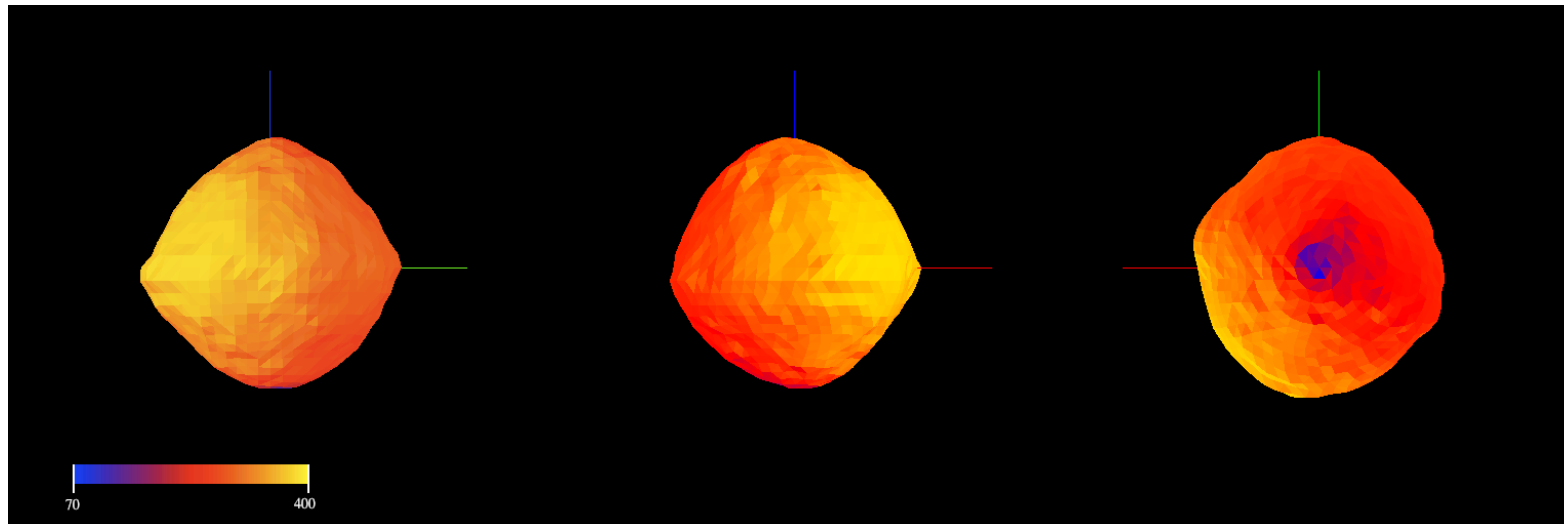
Thermophysical model(s) – TPM

An asteroid TPM calculates :

- ▶ temperature distribution at the surface and in the subsurface: $T(\phi, \theta, z, t)$
- ▶ the emitted thermal IR flux: $f(\lambda, \phi, \theta, t, \vec{\Delta})$
- ▶ $f(\lambda, t, \vec{\Delta}) = \int_{\phi} \int_{\theta} f(\lambda, \phi, \theta, t, \vec{\Delta}) \sin(\theta) d\theta d\phi$

as a function of physical and orbital parameters:

- ▶ Size, macroscopic shape, Albedo A (Bolometric Bond's albedo), Thermal Inertia Γ , surface roughness $\bar{\theta}$, spin vector \vec{v}_{spin}
- ▶ Heliocentric position $\vec{r}(t)$ (and its history)



Equations of the TPM

Thermal conductivity in the subsurface: Surface boundary condition

$$\epsilon\sigma T^4(r, z, t) - \kappa \frac{\partial T(r, z, t)}{\partial z} = \frac{(1 - A)S_{\odot}}{r^2(t)} \mu(\theta, \phi, t) + \int_{\Sigma} J_V(r') F(r, r') da' + \epsilon\sigma(1 - \epsilon) \int_{\Sigma} J_{IR}(r') F(r, r') da' \quad (1)$$

Thermal conductivity in the subsurface: heat diffusion in the regolith

$$\rho C \frac{\partial T}{\partial t} = \frac{\partial}{\partial z} \kappa \frac{\partial T}{\partial z} \simeq \kappa \frac{\partial^2 T}{\partial^2 z} \quad (2)$$

for κ independent of z .

Thermal conductivity in the subsurface: boundary condition at depth

$$\left(\frac{\partial T}{\partial z} \right)_{z \gg l_s} = 0 \quad (3)$$

TPM: Numerical solution of the equation

Each simulation starts with the facets of the mesh at an initial temperature (e.g. constant).

The model calculates the heat flow from the surface into the sub-surface using a discrete grid of sub-surface elements (δZ) in successive increment of time (δt). For each facet we find the temperature at the time ($t + \delta t$) by:

$$T_i(Z, t + \delta t) = T_i(Z, t) + \left(\frac{2\pi\delta t}{\delta Z^2 P_{SID}} \right) \times (T_i(Z + \delta Z, t) - 2T_i(Z, t) + T_i(Z - \delta Z, t)) \quad (4)$$

TPM: Numerical solution of the equation

We obtain the surface temperature from the evolution equation and the surface boundary condition:

$$\begin{aligned} T_i(0, t + dt) = & T_i(0, t) + 2 \frac{dt\omega}{dZ^2} (T_i(dZ, t) - T_i(0, t)) - \\ & 2 \frac{dt\sqrt{\omega}}{\Gamma dZ} (\epsilon\sigma T_i^4(0, t) - \frac{(1-A)S_{\odot}}{r^2(t)}\mu_i(t) - \\ & \sum_{j \neq i} f_{ij} E_j^{refl}(0, t) \cos(\beta_{ij}) - \epsilon\sigma(1-\epsilon) \sum_{j \neq i} f_{ij} T_j^4(0, t) \cos(\beta_{ij})) \quad (5) \end{aligned}$$

Application: Required sensitivity of
OTES on board of OSIRS-REx

OSIRIS-REx

From Wikipedia, the free encyclopedia

Origins Spectral Interpretation Resource Identification Security Regolith Explorer (OSIRIS-REx) is a planetary science mission, the third selected in the [New Frontiers Program](#). The mission will study and return a sample of a [carbonaceous asteroid](#) to Earth for detailed analyses in about 2023. Material returned is expected to enable scientists to learn more about the time before the birth of our solar system, initial stages of planet formation, and the source of organic compounds which led to the formation of life. The team planning the mission will be staffed by a multi-generational team due to the long duration of the program.^[5]^[*dead link*] The cost of the mission will be approximately \$800 million not including the launch vehicle which is expected to add an additional \$200 million to the total.^[6]

**Origins Spectral Interpretation
Resource Identification Security
Regolith Explorer**



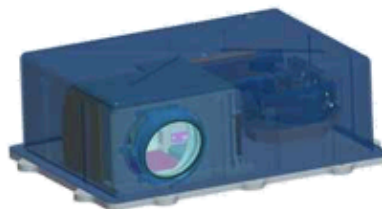
OSIRIS-REx



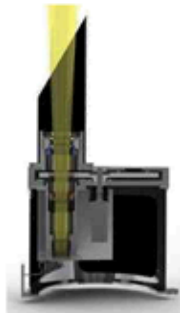
Science requirements are fulfilled by our instrument capabilities



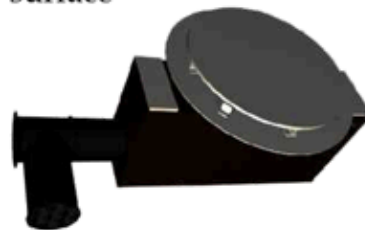
–**PolyCam** acquires 1999 RQ36 from 2M km range and refines its ephemeris



–**OLA** maps the shape and topography



–**MapCam** performs filter photometry and maps the surface

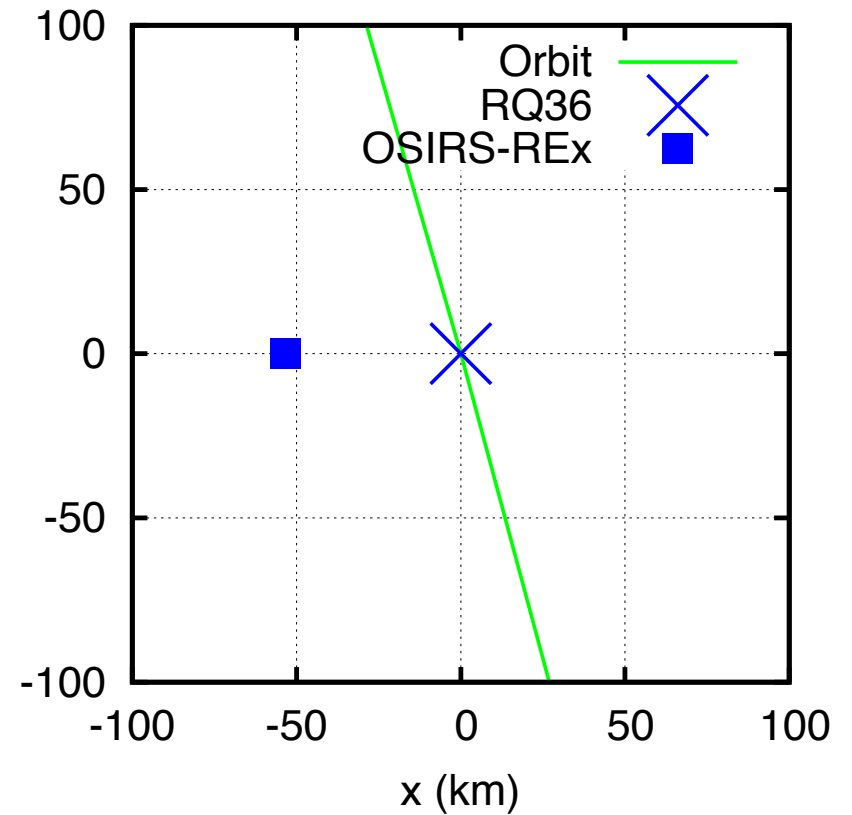
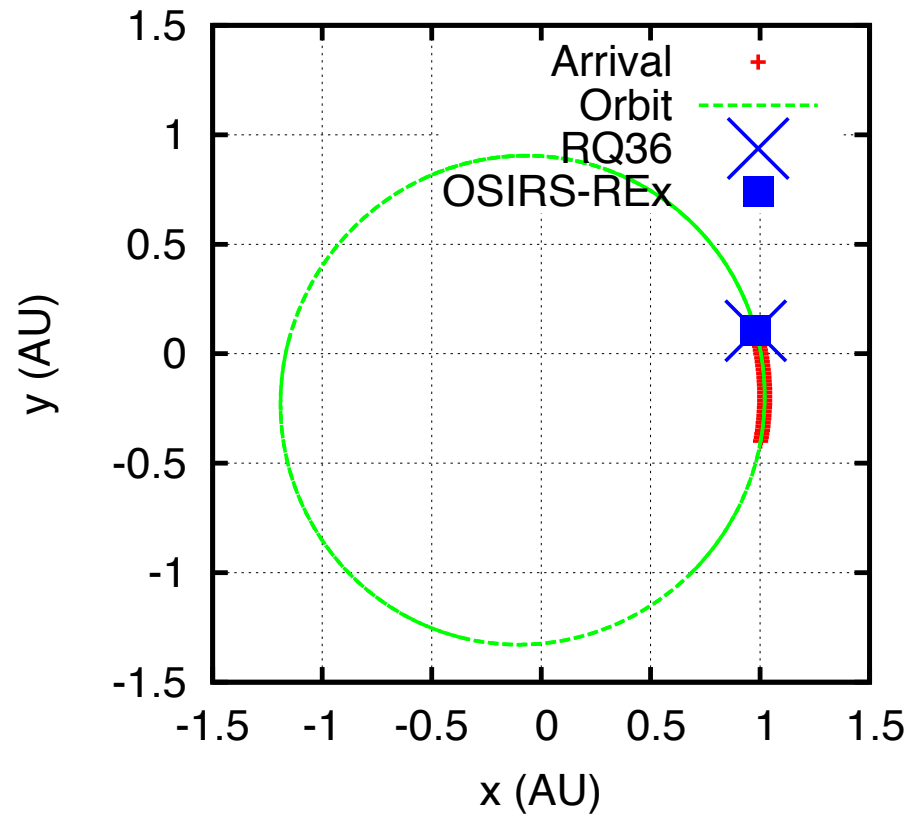


–**OVIRS** maps the spectral properties from 0.4 – 4.3 μm

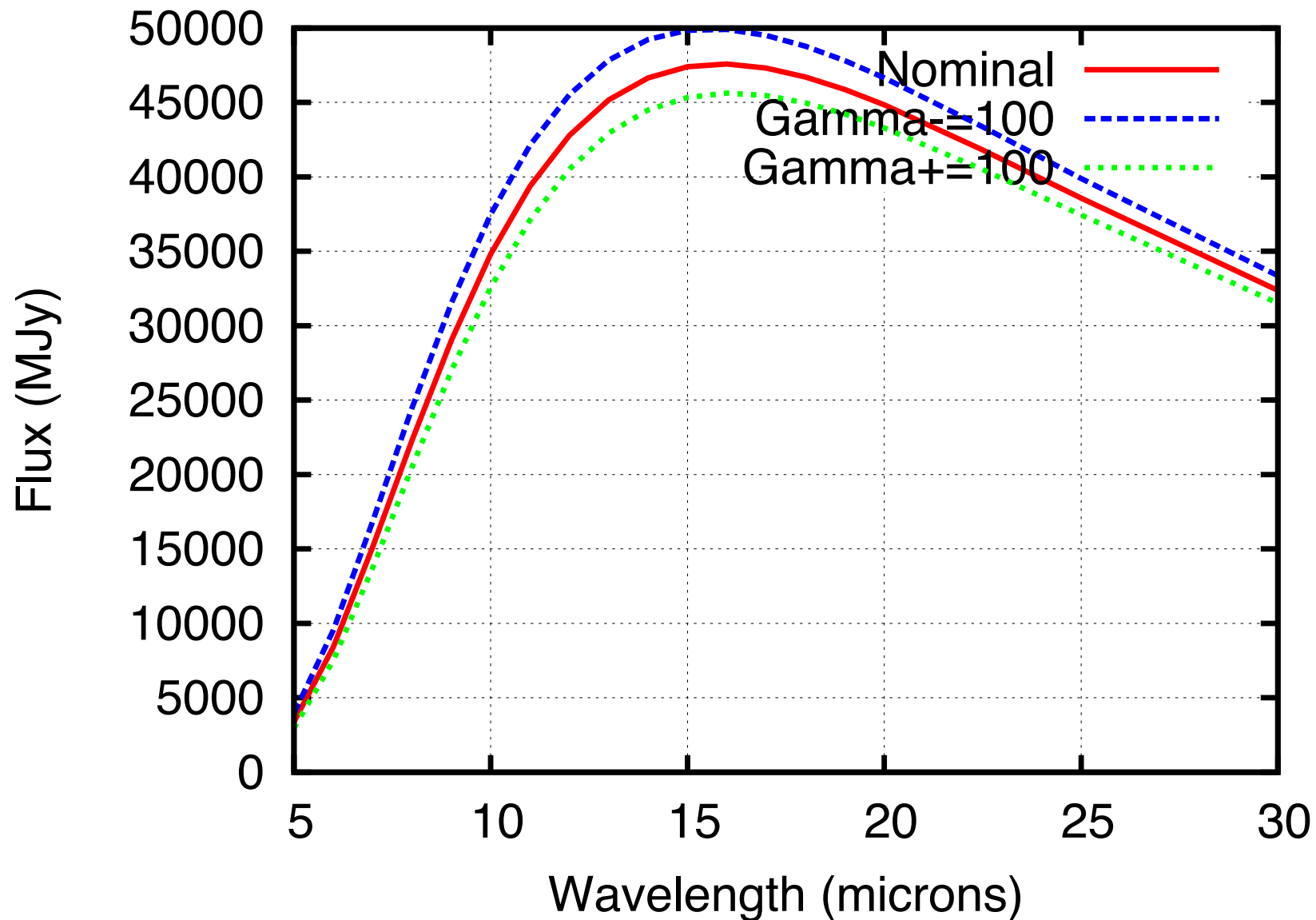


–**OTES** maps the spectral properties from 4 – 50 μm

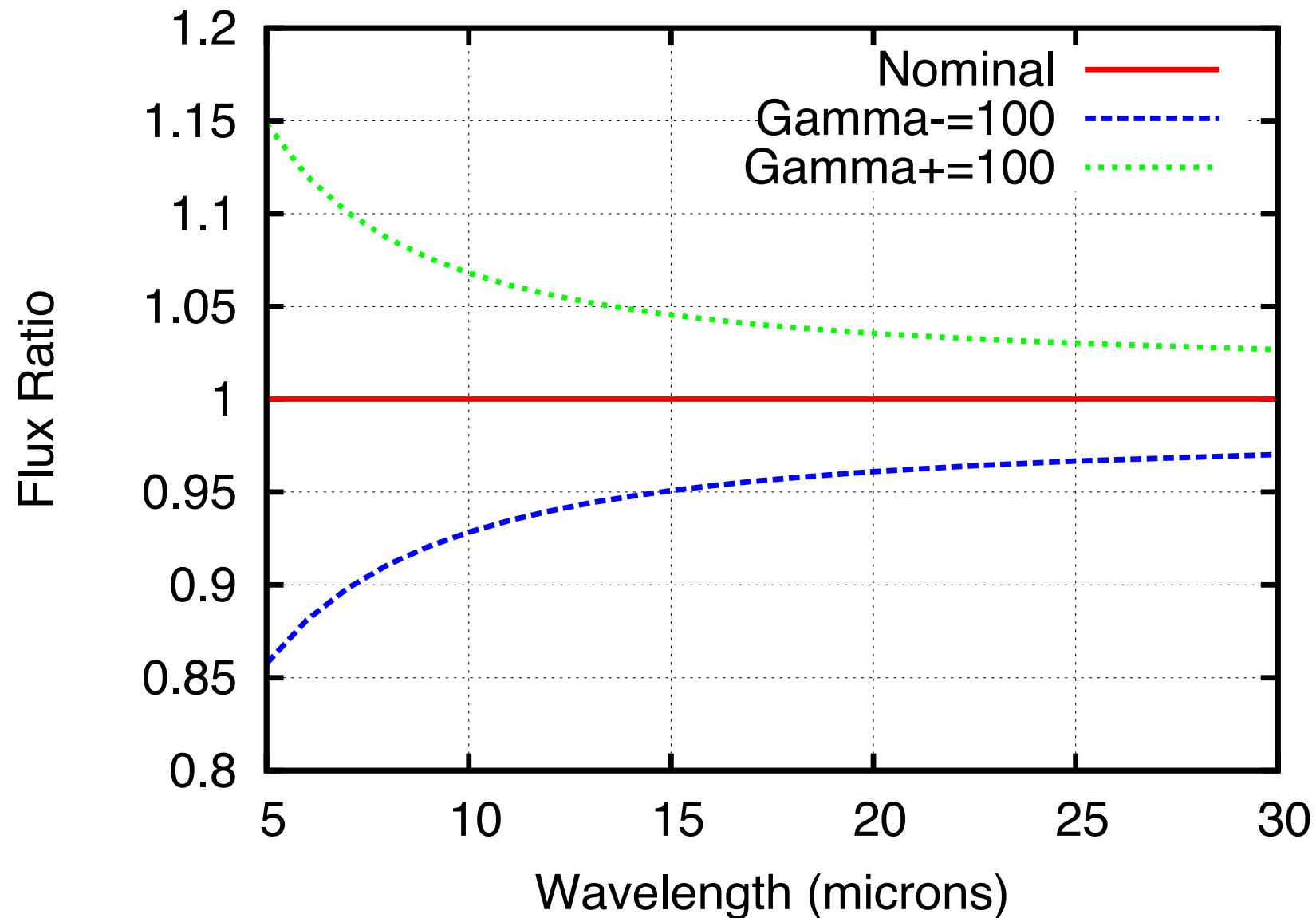
Example of TPM calculation: OTES spectrum at arrival



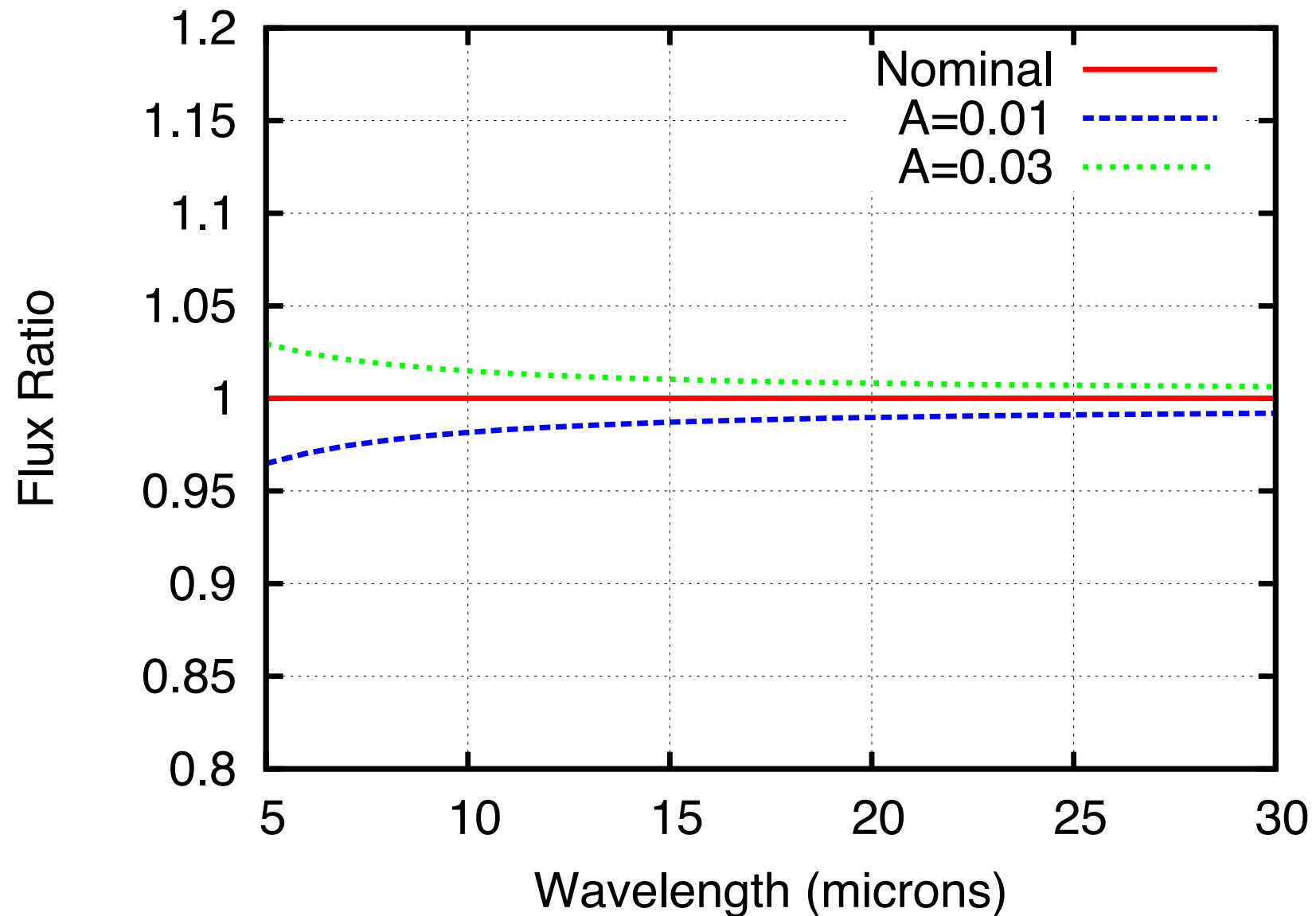
OTES spectra



OTES ratio of spectra: accuracy



OTES ratio of spectra: accuracy



OTES: accuracy - conclusions

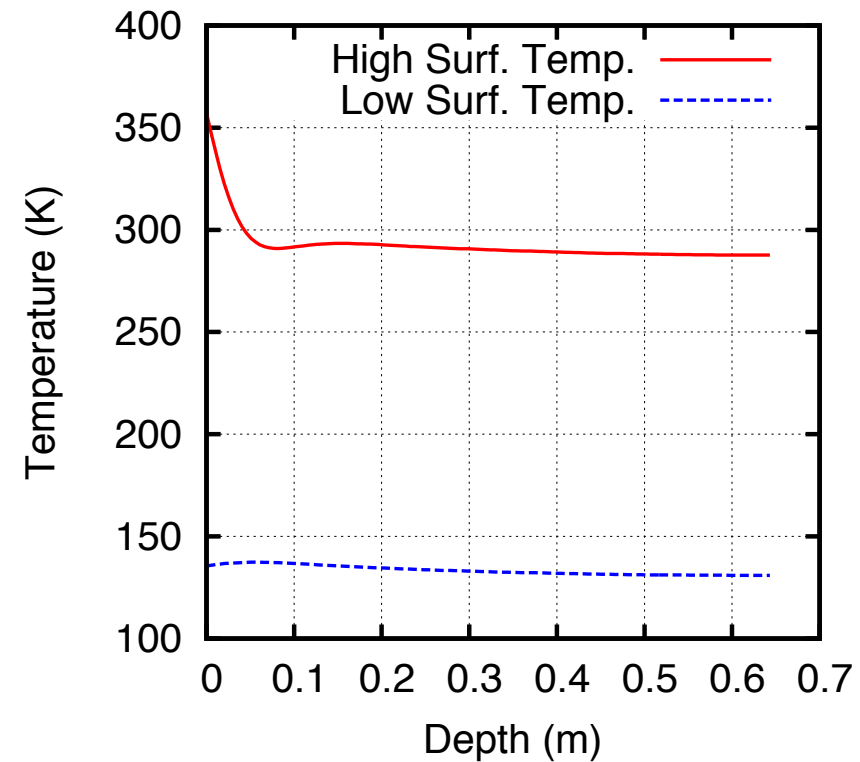
- ▶ Accurate determination of the value of Γ is required for accurate modeling of the net acceleration to RQ36 due to emission of thermal IR photons (Yarkovsky effect).
- ▶ Variation of the value of Γ of $100 J m^{-2} s^{-0.5} K^{-1}$ causes a wavelength-dependent variation of the flux $>5\%$ relative only for $\lambda < 10 \mu m$.
- ▶ Desirable accuracy of OTES measurements within few percent.

Surface, sub-surface temperatures
and thermal history of RQ36

Example of subsurface temperatures

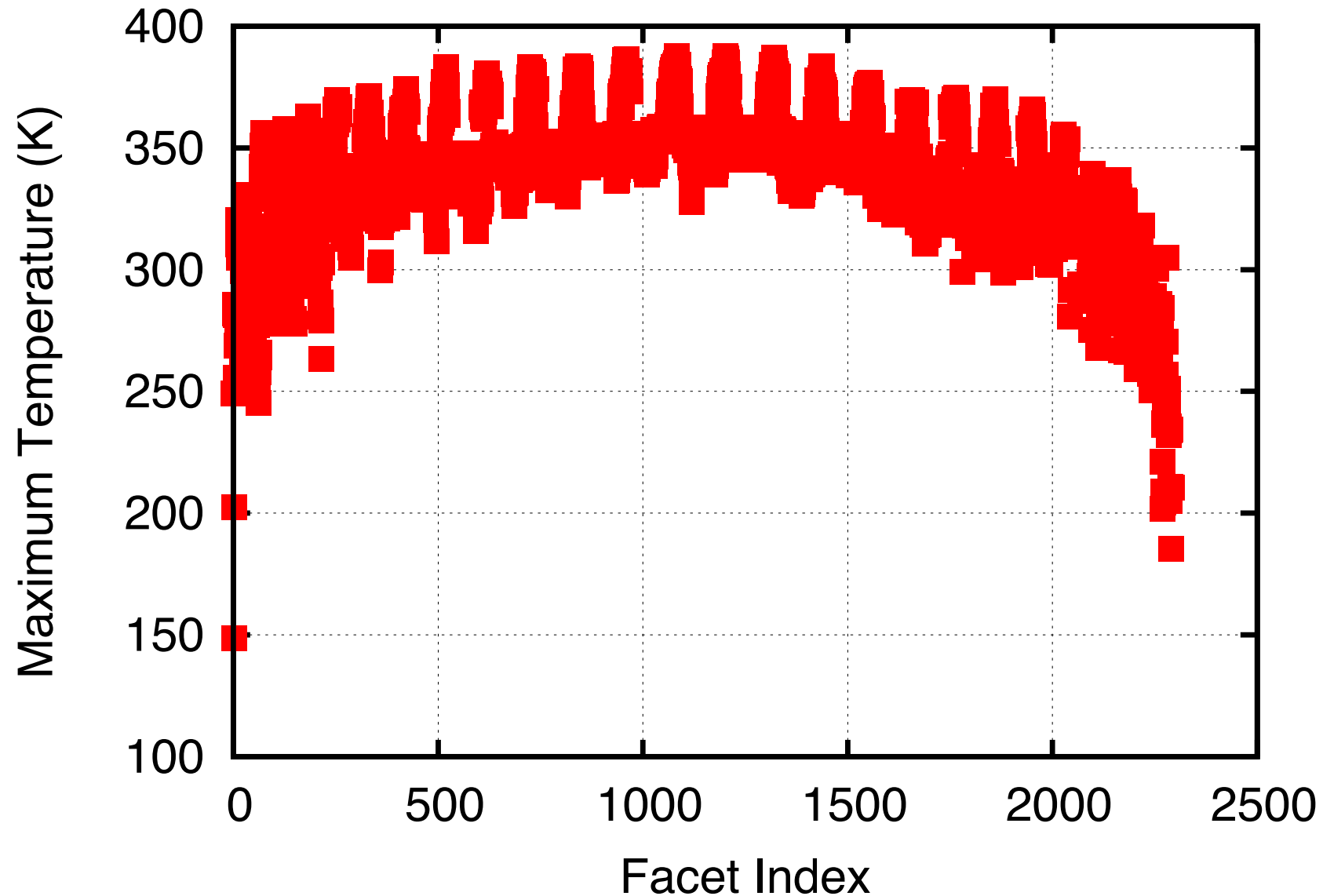
Assuming $\rho=2500 \text{ kg m}^{-3}$;
 $C=600 \text{ J kg K}^{-1}$, we obtain
 $\kappa=0.25 \text{ W/m/K}$ for
 $\Gamma=600 \text{ Jm}^{-2}\text{s}^{-0.5}\text{K}^{-1}$. Since:

$$l_s = \sqrt{\frac{\kappa P}{2\pi\rho C}} = 0.02\text{m} \quad (6)$$



Some region of the surface are always cold

Max surface temperature monitored over several rotations, during the arrival TPM track.



Temperatures of RQ36 and alteration of organics

Compound	Consequence of heating	Temperature threshold (K)	Probability at surface (%)	Probability 5 cm depth (%)	Reference
Ferruginous smectite	First dehydration ¹	300	100	100	a
Nontronites	First dehydration ¹	300	100	100	a
Murchinson bulk	Degradation ²	300	100	100	b
Ferruginous smectite	Second dehydration ¹	360	100	85	a
Nontronites	Second dehydration ¹	360	100	85	a
Insoluble organic matter	Degradation ²	370	95	69	b
Labile kerogen	Decomposition	370	95	69	c
Ferruginous smectite	Third dehydration ¹	380	90	65	a
Nontronites	Third dehydration ¹	380	90	65	a
Montmorillonite	First dehydration ¹	420	80	40	d
Hg and volatiles (CM & CV)	Release of	470	62	18	e
Montmorillonite	Second dehydration ¹	520	43	12	d
Ferruginous smectite	Dehydroxylation ¹	670	13	9	a
Nontronites	Dehydroxylation ¹	670	13	9	a

Table: Threshold temperature for a variety of chemical compounds discussed in the text. The probability of the reaction is given at the surface and at 5-cm depth. All boxes where the probability is >50% are shaded. See text for more details. References: (a) [?]; (b) [?]; (c) Franchi, personal communication; (d) [?] (e) [?]. Notes: ¹heating performed under an inert atmosphere of N gas (to avoid oxidation). ²heating performed under an inert atmosphere of Ar gas. The threshold temperature is for complete loss of the C-H aliphatic band in the infrared in 200 years of time.

Transport of organics to the Earth

Marco Delbo

UNS-CNRS-Observatoire de la Côte d'Azur, Nice, France

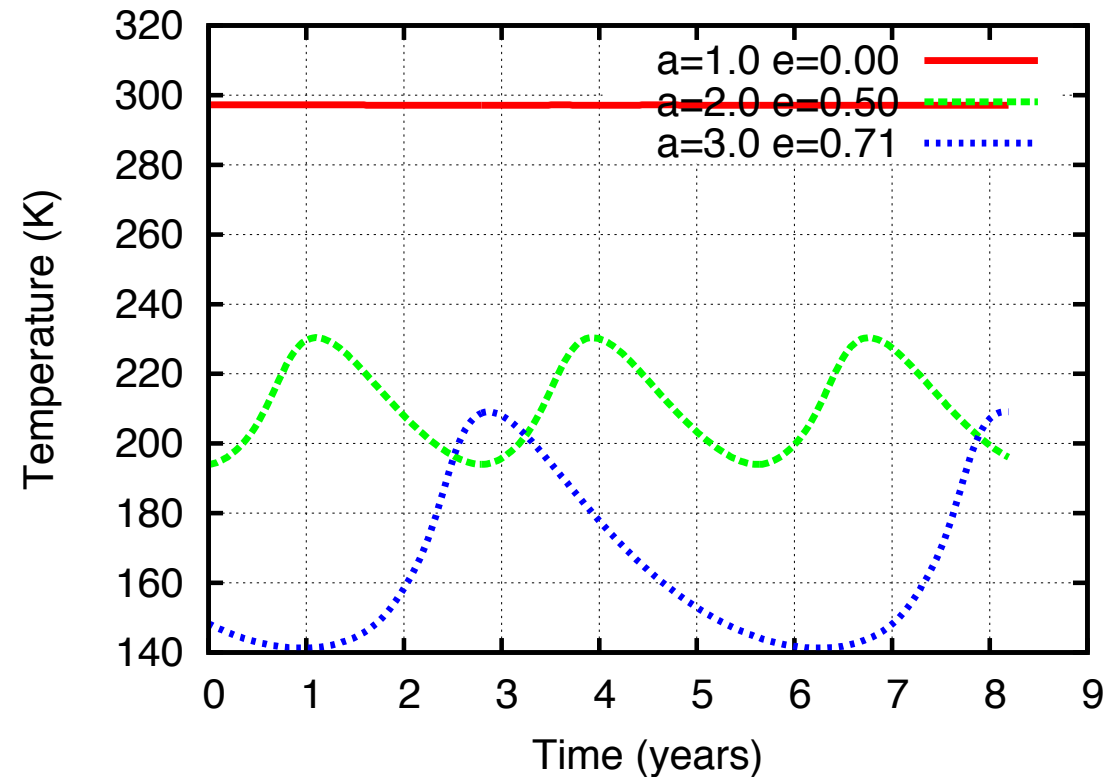
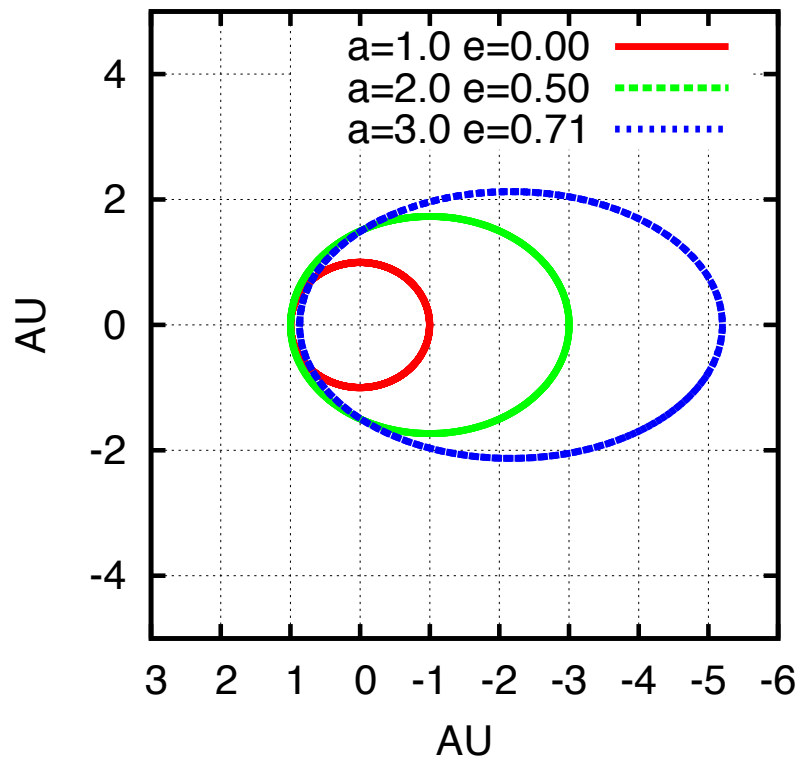
September 30, 2011

Disclaimer and Outline of this talk

- ▶ Degradation of organic matter during its transport from the asteroid Main Belt to the Earth.
 - ▶ **Heat source:**
radiative heating from the Sun of meteoroids is the mechanism invoked to cause the degradation of the organic matter.

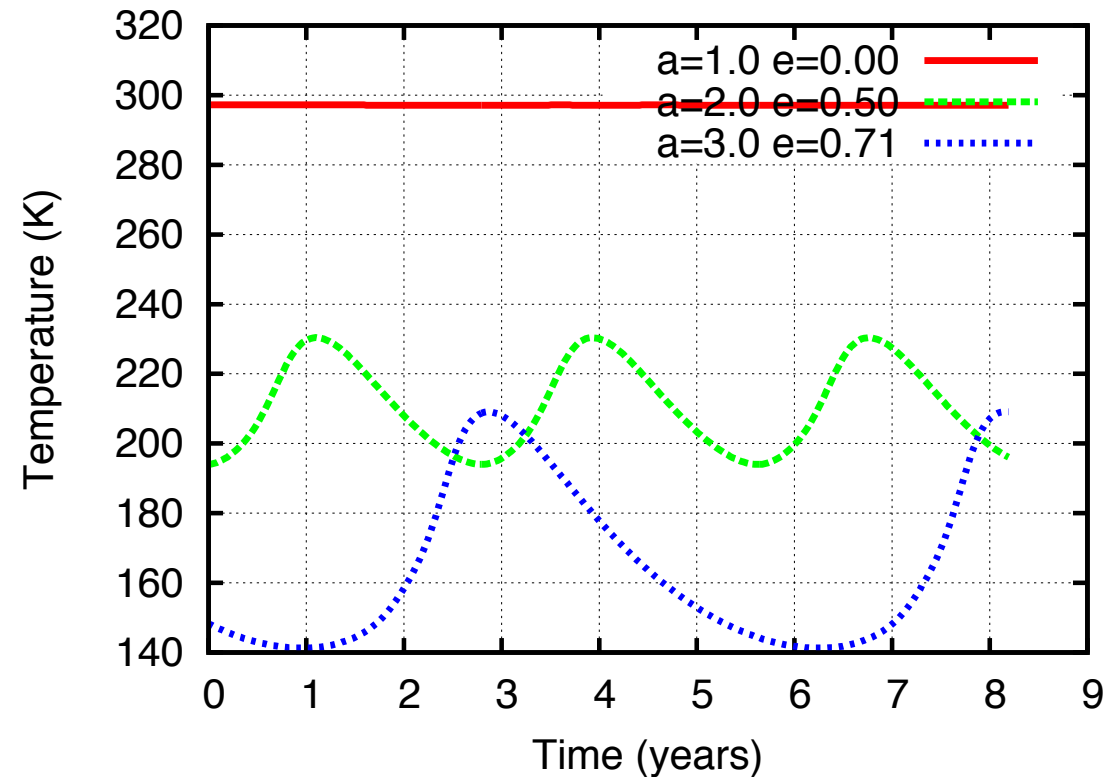
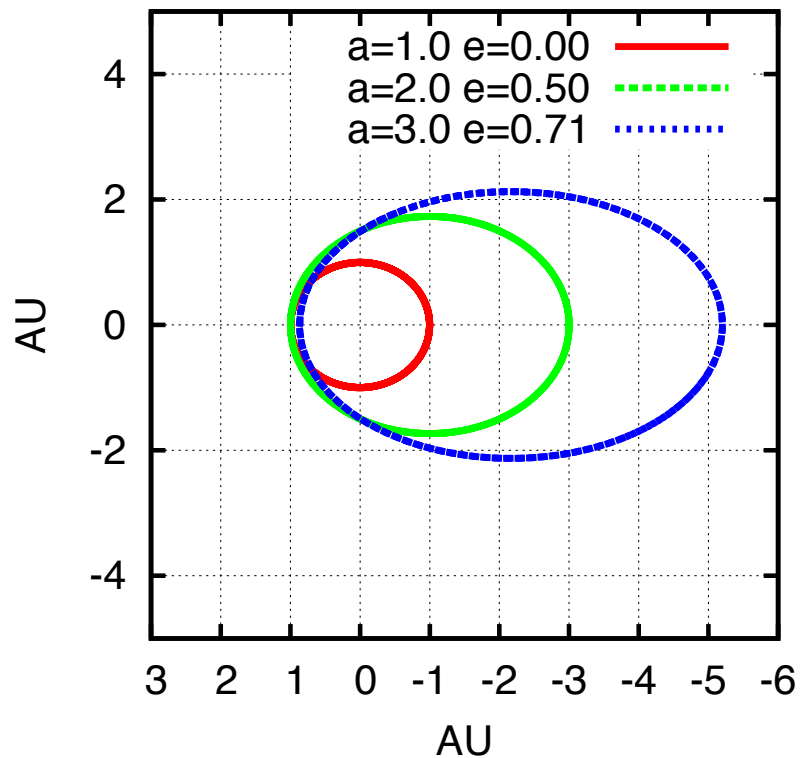
Meteoroids inner temperatures as a function of their orbits

Calculated temperatures 3.5 m below the surface of meteoroids, as a function of time and their orbits.



Meteoroids inner temperatures as a function of their orbits

Calculated temperatures 3.5 m below the surface of meteoroids, as a function of time and their orbits.

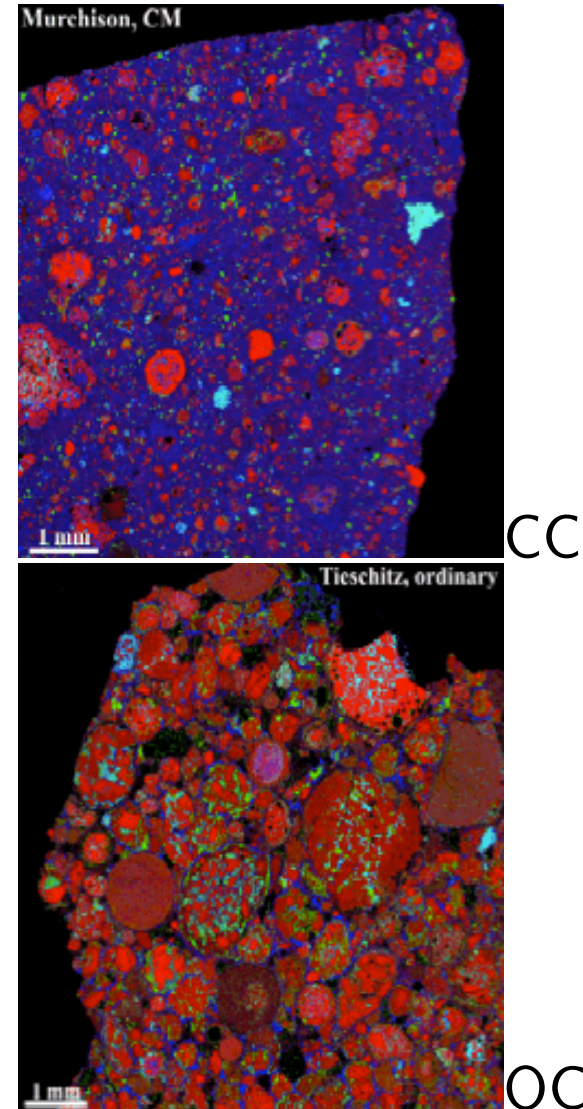


Note: Green orbit: Tagish Lake like orbit (Brown et al. 2000)

Note: Blue orbit: Orgueil like orbit (Gounelle et al. 2006)

Primitive asteroids' analogs: the carbonaceous chondrites

- ▶ Carbonaceous chondrites is a class of meteorites thought to derive from primitive asteroids
 - ▶ Low albedo ($p_V < 0.1$)
 - ▶ C-complex spectroscopic class
- ▶ Carbonaceous chondritic meteorites contain abundant carbon up to a few wt%, which exists predominantly in the form of insoluble organic matter (IOM).
- ▶ Organics are also present in the bulk of the matrix of CC meteorites.



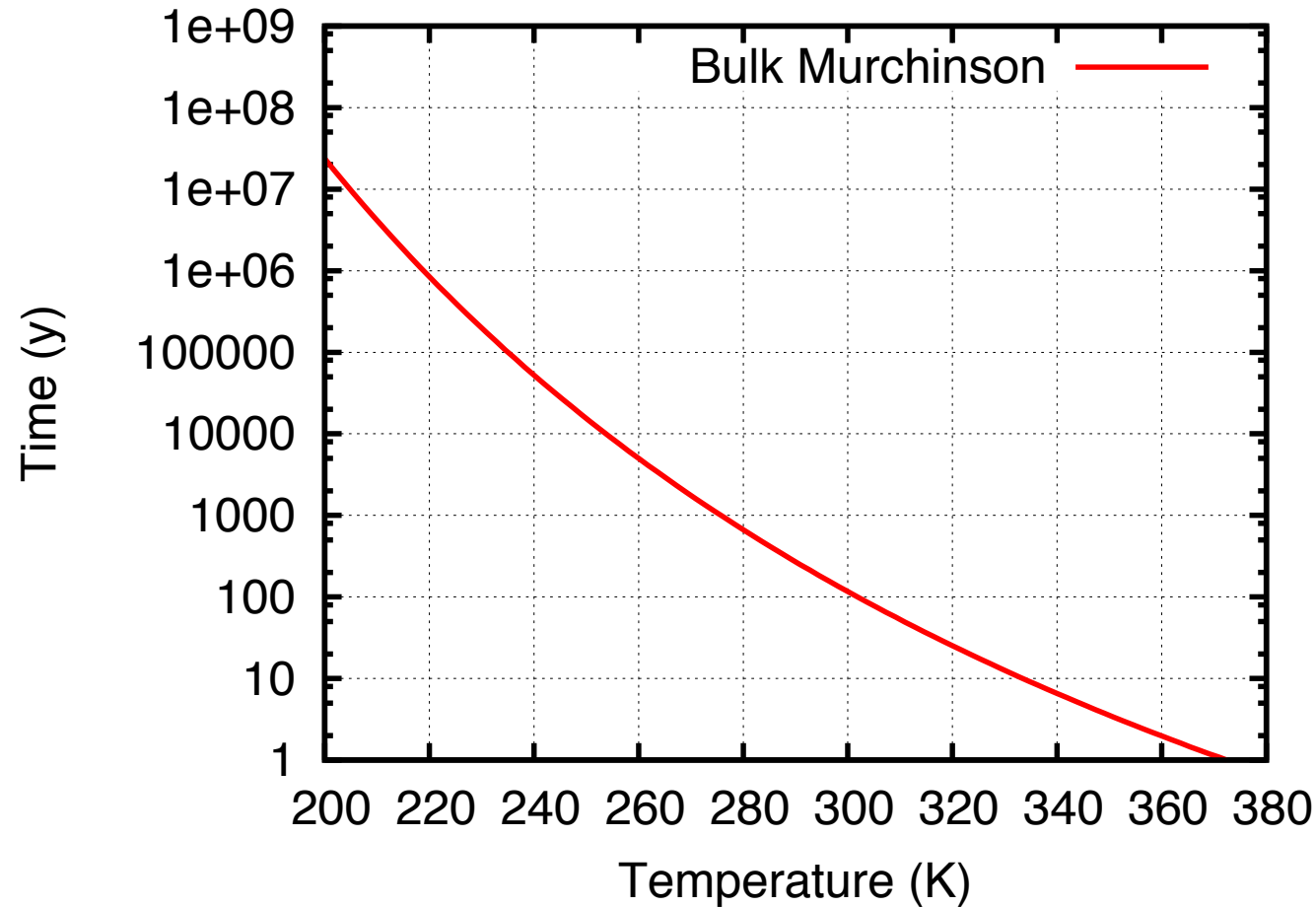
Degradation of organic matter and heat

- ▶ Organics can be degraded by heat:



- ▶ Rate of the reaction: $\frac{dx}{dt} = f(x) \times A \exp(-\frac{E_a}{RT})$
- ▶ Kebukawa et al. (2010) have studied the kinetic parameters of the reaction above for the organics in the bulk and in the IOM of the Murchinson meteorite.
- ▶ These parameters can be used to calculate survivability of organics.
- ▶ It should be noted that these kinetic parameters are based on the loss of aliphatic C–H, so it means this is not for the loss of whole organic matter but for 'degradation' of organic matter.

Time scale and temperatures for degradation of organics



At 300 K organics in the bulk of Murchinson are degraded in only 100 y.

Implications

- ▶ In order to be able to find some un-degraded organics in the CC (e.g. Murchinson) we need the interior of the meteoroids never above ~ 220 K.
- ▶ Low eccentricity orbits at ~ 1 AU imply too hot meteoroids.
- ▶ High eccentricity orbits allow meteoroids to stay cool enough to keep their organics un-degraded.

This is consistent with the orbits of e.g. the **Orgeuil meteorite** (Gounelle et al. 2006) and maybe the **Tagish Lake meteorite** (Brown et al. 2001).

Interferometry of ASTEROIDS

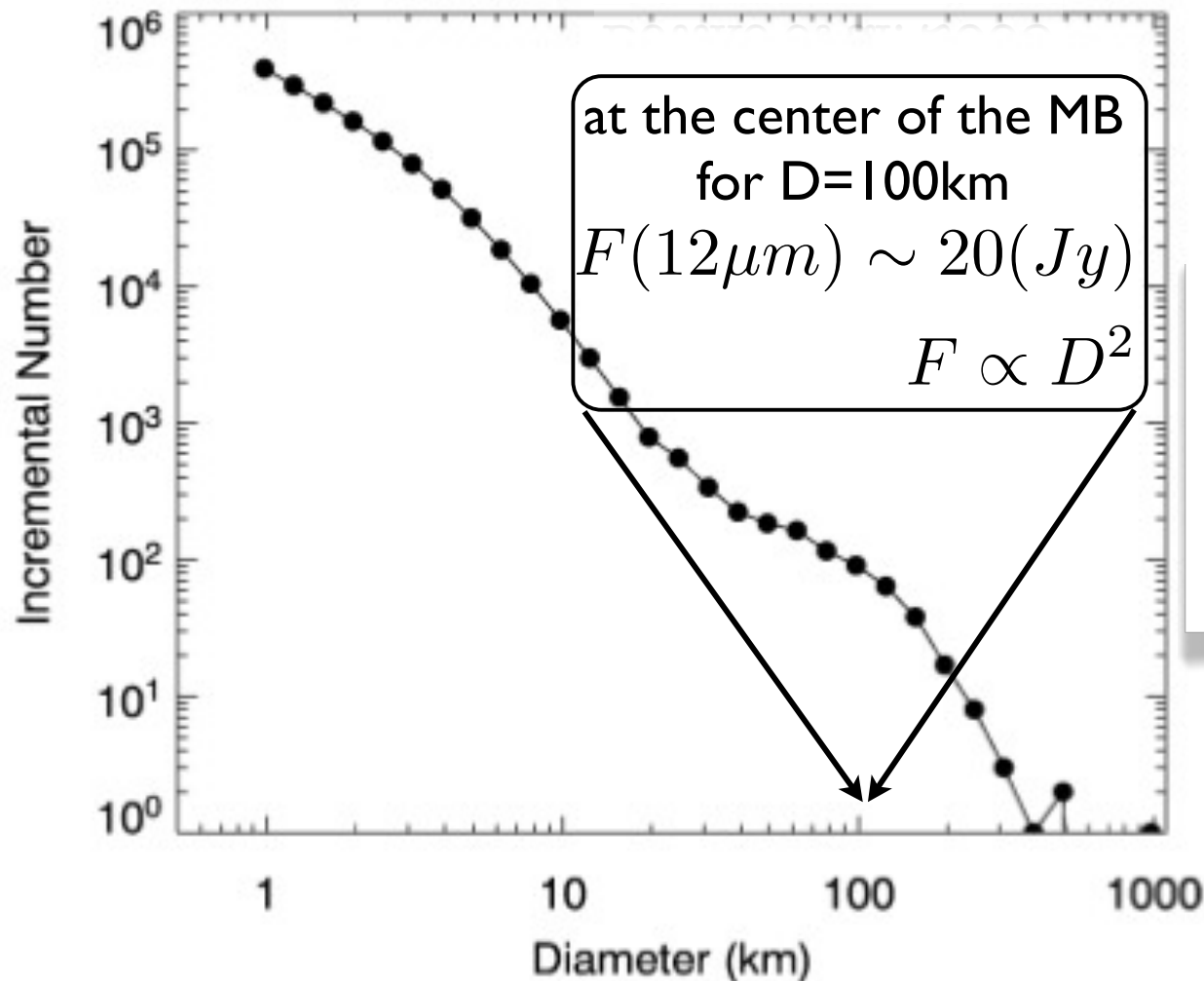
Marco Delbo

CNRS - Observatoire de la Cote d'Azur

Collaborators: A. Matter (Bonn, Germany), **B. Carry** (ESA), **S. Ligi** (Torino, Italy), **P. Tanga** (Nice, France), and **G. Van Belle** (ESO/Lowell)

Size distribution of main belt asteroids

Bottke et al. 2005



Assumption of
spherical shapes

$$\theta(mas) = \frac{D(km)}{0.72 \Delta(AU)}$$

$$\sim D \times \frac{1.5}{\Delta}$$

$\theta(mas) \sim D(km)$
at the center of the Belt

Interferometry and physical characterization of asteroids

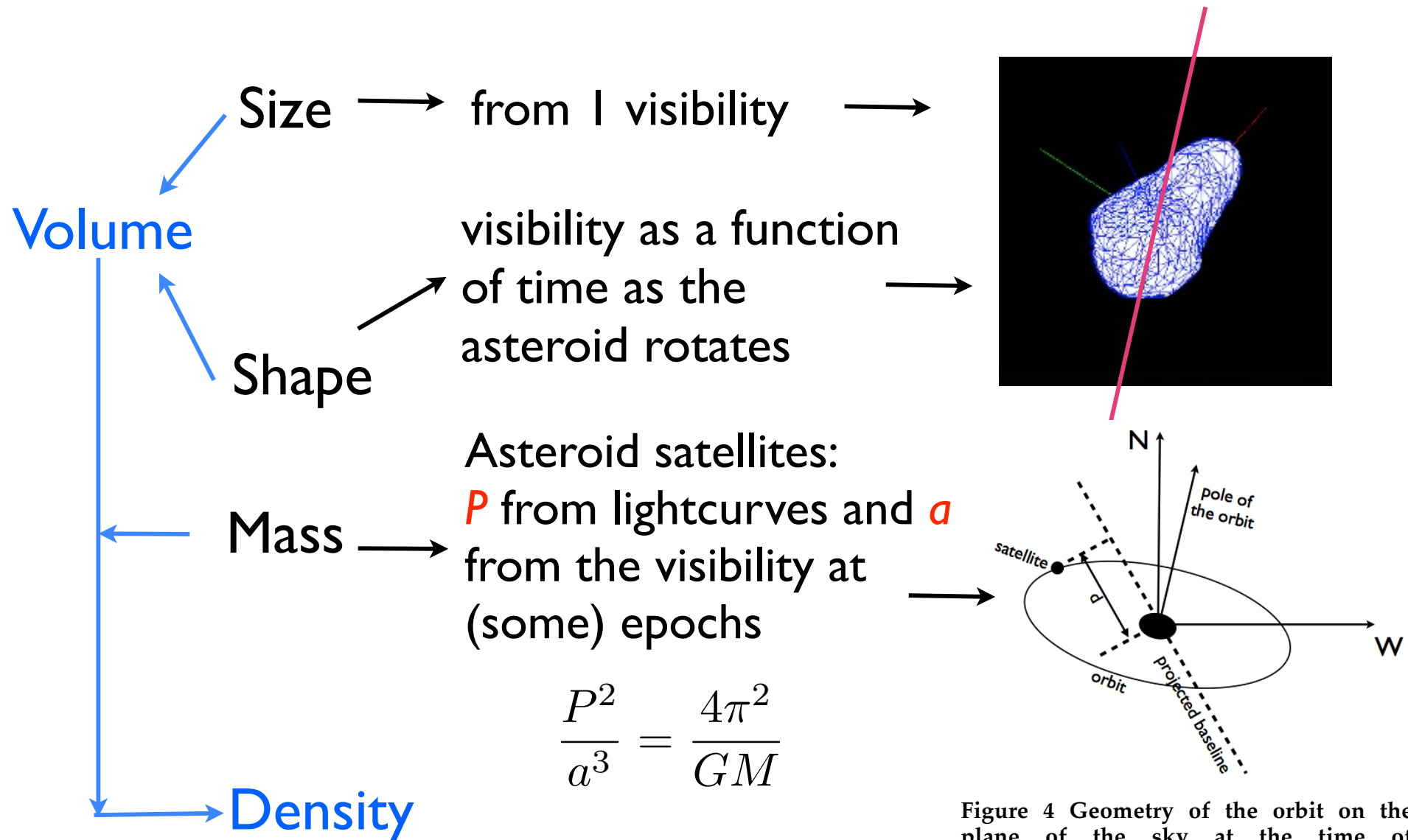


Figure 4 Geometry of the orbit on the plane of the sky at the time of interferometric measurement.

FIRST VLTI-MIDI DIRECT DETERMINATIONS OF ASTEROID SIZES*

M. DELBO^{1,2}, S. LIGORI³, A. MATTER⁴, A. CELLINO⁵, AND J. BERTHIER⁶

¹ UNS, CNRS, Observatoire de la Côte d’Azur, BP 4229 06304 Nice cedex 04, France

² INAF-Osservatorio Astronomico di Torino Strada Osservatorio 20, 10025 Pino Torinese, Torino, Italy; delbo@oca.eu

³ INAF-Osservatorio Astronomico di Torino Strada Osservatorio 20, 10025 Pino Torinese, Torino, Italy

⁴ UNS, Observatoire de la Côte d’Azur, BP 4229 06304 Nice cedex 04, France

⁵ INAF-Osservatorio Astronomico di Torino Strada Osservatorio 20, 10025 Pino Torinese, Torino, Italy

⁶ Institut de Mecanique Celeste (IMCCE) 77 av. Denfert Rochereau, 75014 Paris, France

Received 2008 August 26; accepted 2008 December 16; published 2009 March 24

ABSTRACT

We have obtained the first successful interferometric measurements of asteroid sizes and shapes by means of the Very Large Telescope Interferometer-Mid-Infrared Interferometric Instrument (VLTI-MIDI). The VLTI can spatially resolve asteroids in a range of sizes and heliocentric distances that are not accessible to other techniques such as adaptive optics and radar. We have observed, as a typical bench mark, the asteroid (951) Gaspra, visited in the

metric visibility. Given the brightness distribution $O(x, y, \lambda)$ of a source on the projected sky plane, (x, y) , and the corresponding total flux intensity $I(\lambda) = \int \int O(x, y, \lambda) dx dy$, the visibility is given by $V(u, v) = \hat{O}(u, v)/I(\lambda)$, where $\hat{O}(u, v) = \int \int O(x, y, \lambda) e^{-2\pi i(xu+yv)} dx dy$ is the Fourier transform of $O(x, y, \lambda)$, $u = B_x/\lambda$ and $v = B_y/\lambda$ are the spatial frequencies in rad^{-1} along the x - and y -coordinates, respectively, B_x and B_y are the components along the two orthogonal directions of the interferometer's baseline projected on the plane of the sky, and λ is the wavelength of the light.

In principle, by measuring $V(u, v)$ for a set of different values of u and v , possibly filling the uv -plane, one could directly derive the spatial flux distribution of the source $O(x, y, \lambda)$ by taking the inverse Fourier transform of $V(u, v)$ (aperture synthesis). However, because at present the MIDI acquisition of one calibrated visibility observation requires about 1 hr of time when observations are executed in the service mode, images of asteroids from interferometric measurements are difficult to obtain from aperture synthesis methods. An additional complication comes also from the fact that asteroids rotate considerably during such an interval of time.

Simple geometric models (2)

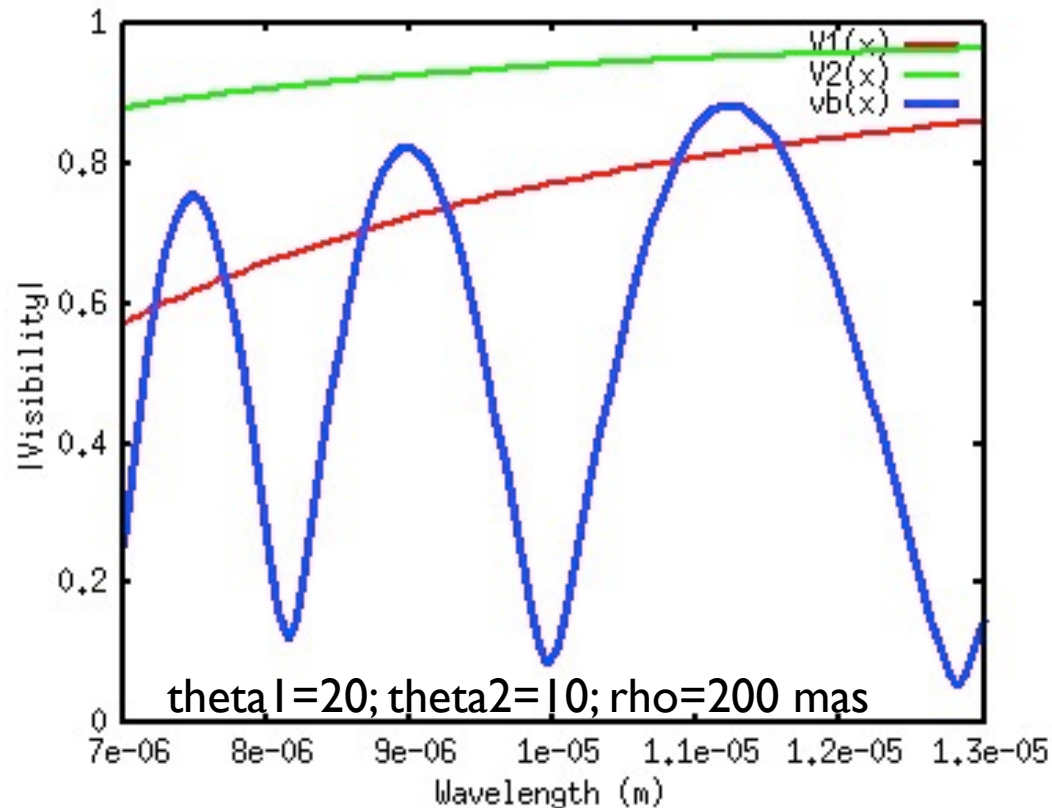
binary model

Visibility

$$|V_b(u)| = \frac{\sqrt{V_{\theta_1}^2 I_{\theta_1}^2 + V_{\theta_2}^2 I_{\theta_2}^2 + 2V_{\theta_1} I_{\theta_1} V_{\theta_2} I_{\theta_2} \cos(2\pi u \rho)}}{I_{\theta_1} + I_{\theta_2}}$$

Interferometric
visibility of a binary of
components of sizes
 θ_1 and θ_2 separated
by a distance ρ

as function of λ
in meters



Simple geometric models (2)

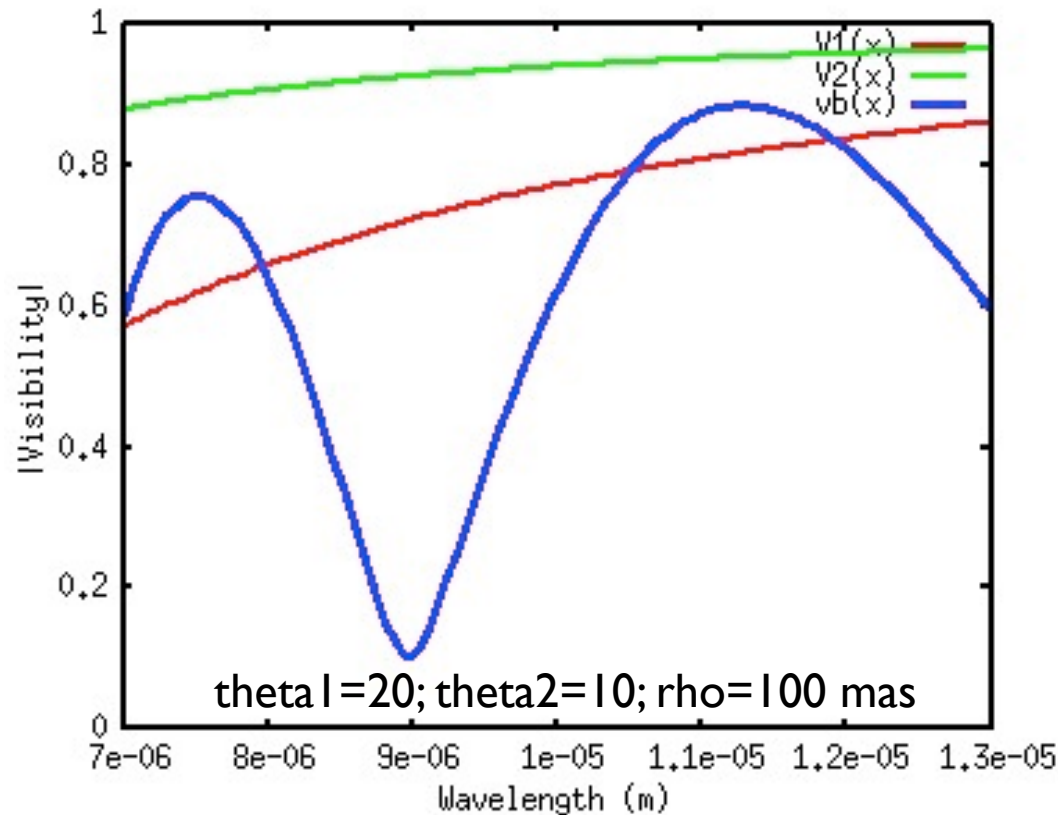
binary model

Visibility

$$|V_b(u)| = \frac{\sqrt{V_{\theta_1}^2 I_{\theta_1}^2 + V_{\theta_2}^2 I_{\theta_2}^2 + 2V_{\theta_1} I_{\theta_1} V_{\theta_2} I_{\theta_2} \cos(2\pi u \rho)}}{I_{\theta_1} + I_{\theta_2}}$$

Interferometric
visibility of a binary of
components of sizes
 θ_1 and θ_2 separated
by a distance ρ

as function of λ
in meters



Simple geometric models (2)

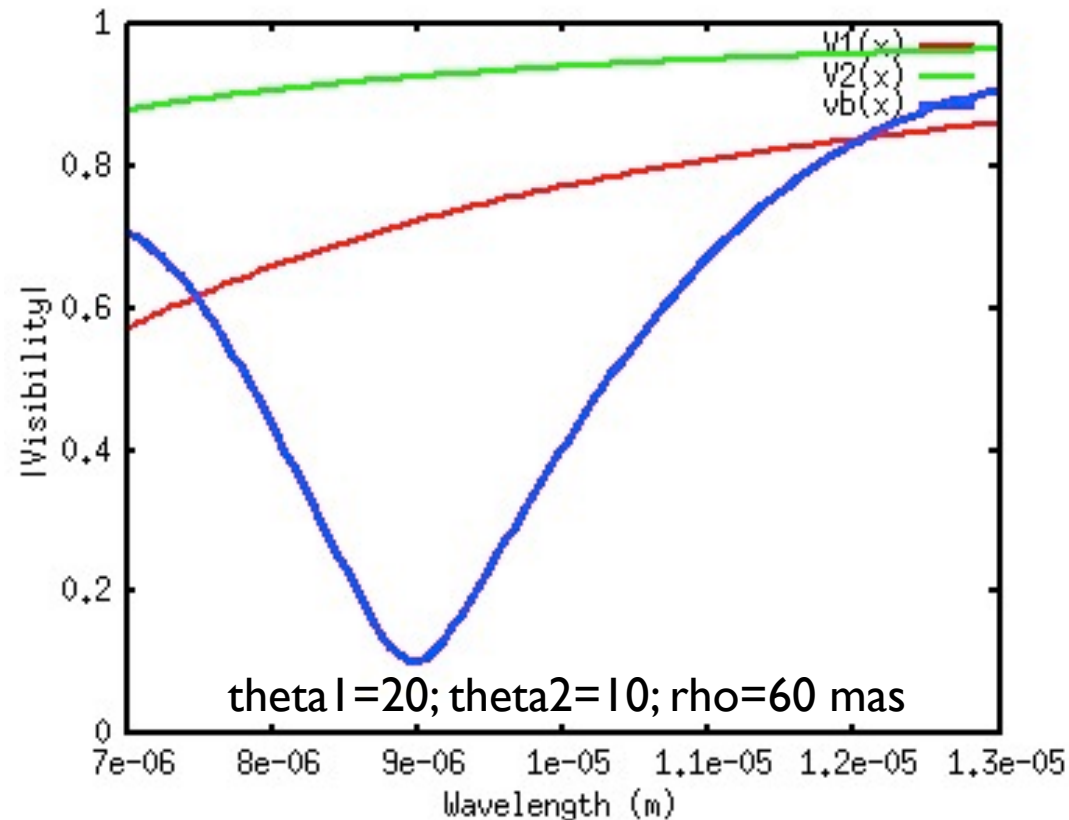
binary model

Visibility

$$|V_b(u)| = \frac{\sqrt{V_{\theta_1}^2 I_{\theta_1}^2 + V_{\theta_2}^2 I_{\theta_2}^2 + 2V_{\theta_1} I_{\theta_1} V_{\theta_2} I_{\theta_2} \cos(2\pi u \rho)}}{I_{\theta_1} + I_{\theta_2}}$$

Interferometric
visibility of a binary of
components of sizes
 θ_1 and θ_2 separated
by a distance ρ

as function of λ
in meters



The VLTI of the ESO

- Coherent combination of the light from telescopes (distance between them B) of the VLT
- Resolution $\theta \sim \lambda/B$
 - MIDI $\lambda \in [8, 13] \mu\text{m}$
 - AMBER $\lambda \in [1.2, 2.5] \mu\text{m}$
 - VLTI $B \in [16, 120] \text{m}$

$$\theta_{\text{MIDI}} \in [15, 100] \text{mas}$$

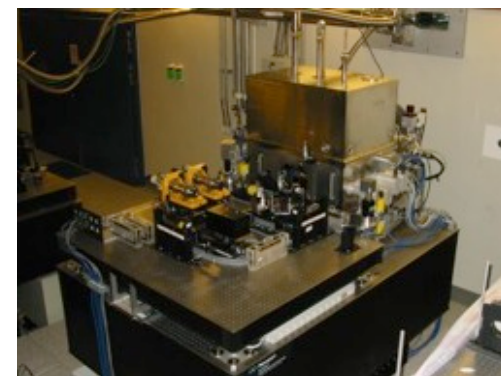
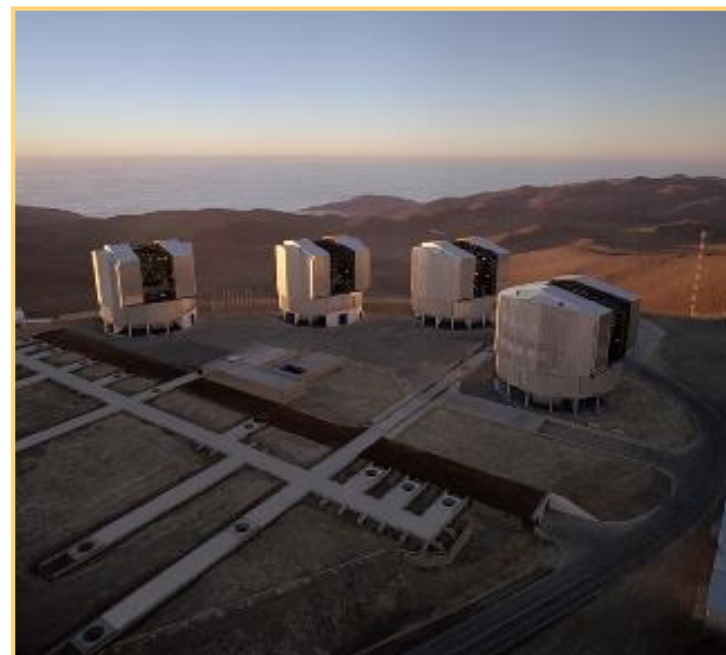
$$\theta_{\text{AMBER}} \in [3, 25] \text{mas}$$

Not sensitive enough for asteroids..

$$\theta_{\text{PRIMA}} \in [3, 25] \text{mas}$$

$K < 9$ (guide star) dual field (reference star and asteroid need to be within $\sim 30''$)

So far results for MIDI only



First successful observations of asteroids with MIDI-VLT

Obtained fringes on

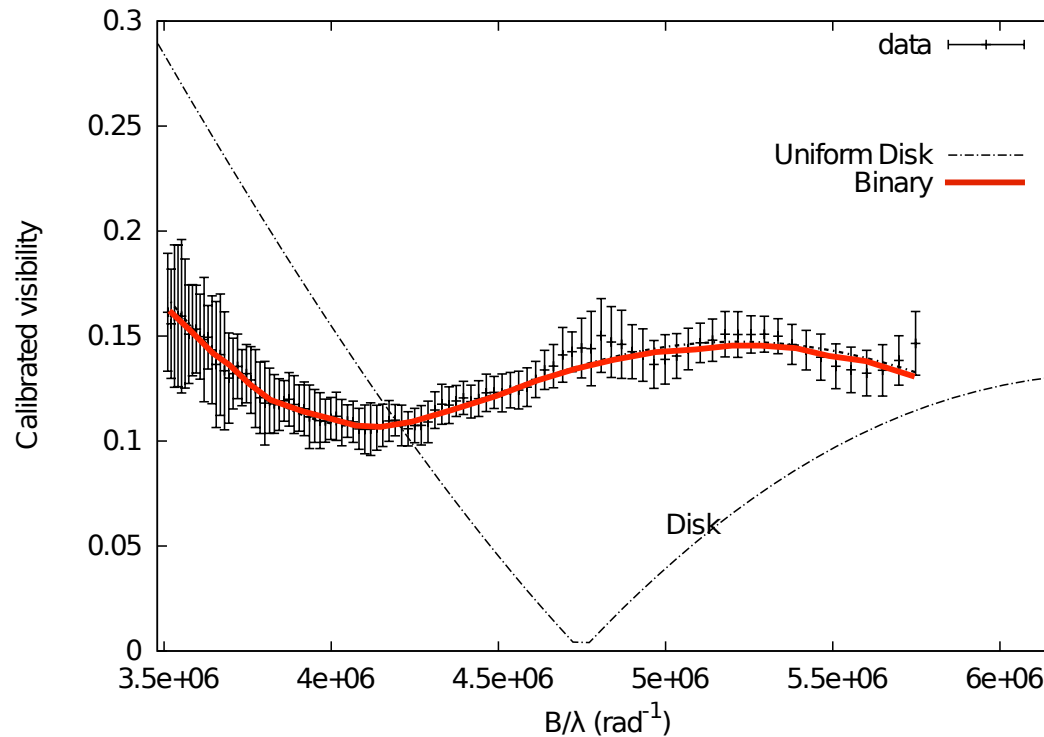
- 951 Gaspra (a testbed) see Delbo et al 2009
- 234 Barbara (complex shape)
 - long rotation period (26.5 hr, Schober 1981; Harris & Young 1983) suggestive of a possible binary system.
 - interferometric observations by Delbo et al 2009
- 41 Daphne (complex shape)
 - Matter et al 2011, see also Matter's talk

Successful observations of asteroids with MIDI-VLT

and Obtained fringes on

- 16 Psyche (metallic asteroid?)
 - see Matter's talk
- 265 Kleopatra (complex shape, metallic?)
- 12 Victoria, 751 Faina, 2 Pallas
- 939 Isberga, 1313 Berna
 - (stay tuned!!)

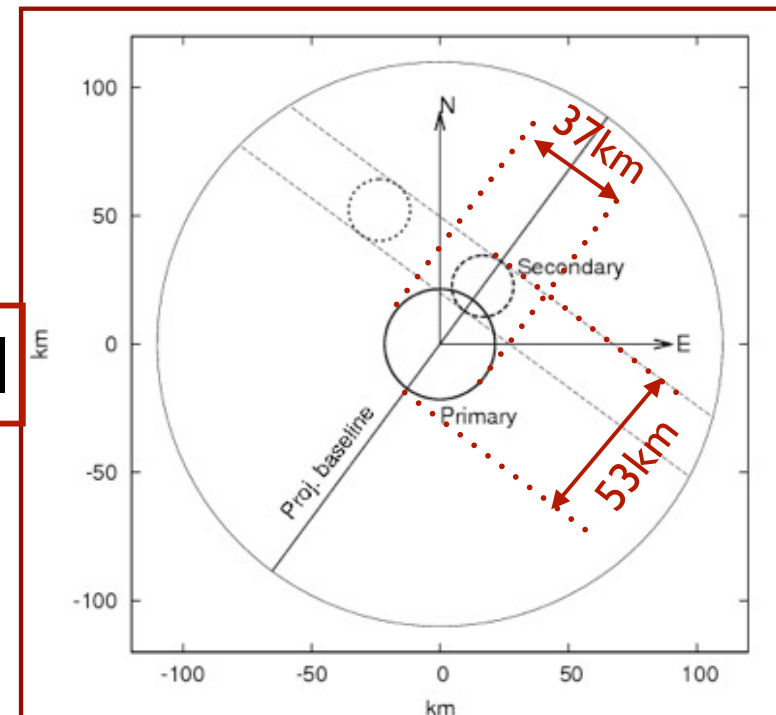
Results for Barbara: size and shape



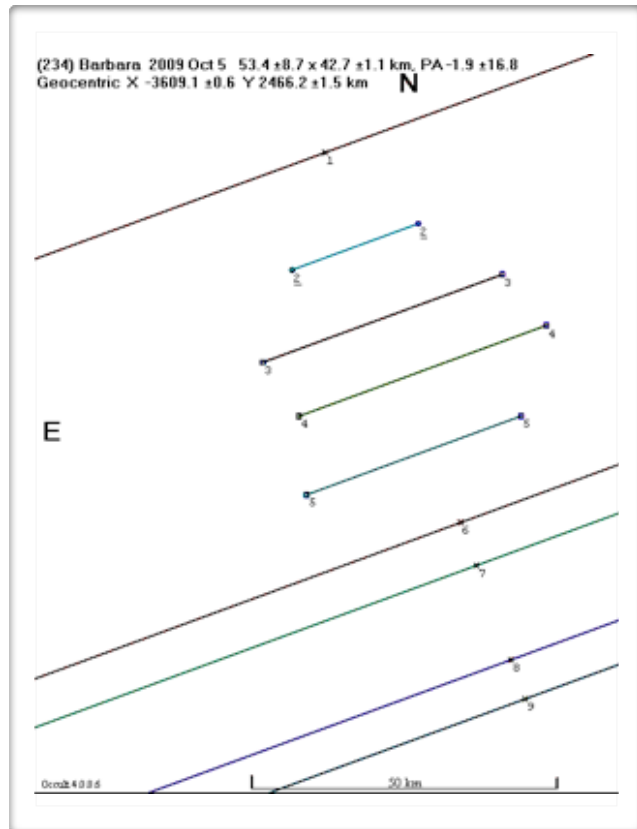
Asteroid	d (km)	Notes
Barbara	44.6 ± 0.3	poor fit
Barbara(1)	37.1 ± 0.5	primary
Barbara(2)	21.0 ± 0.2	satellite
	a (km)	
(1)–(2)	24.2 ± 0.2	separation

Note. Uncertainties are 1σ .

proposed geometric model



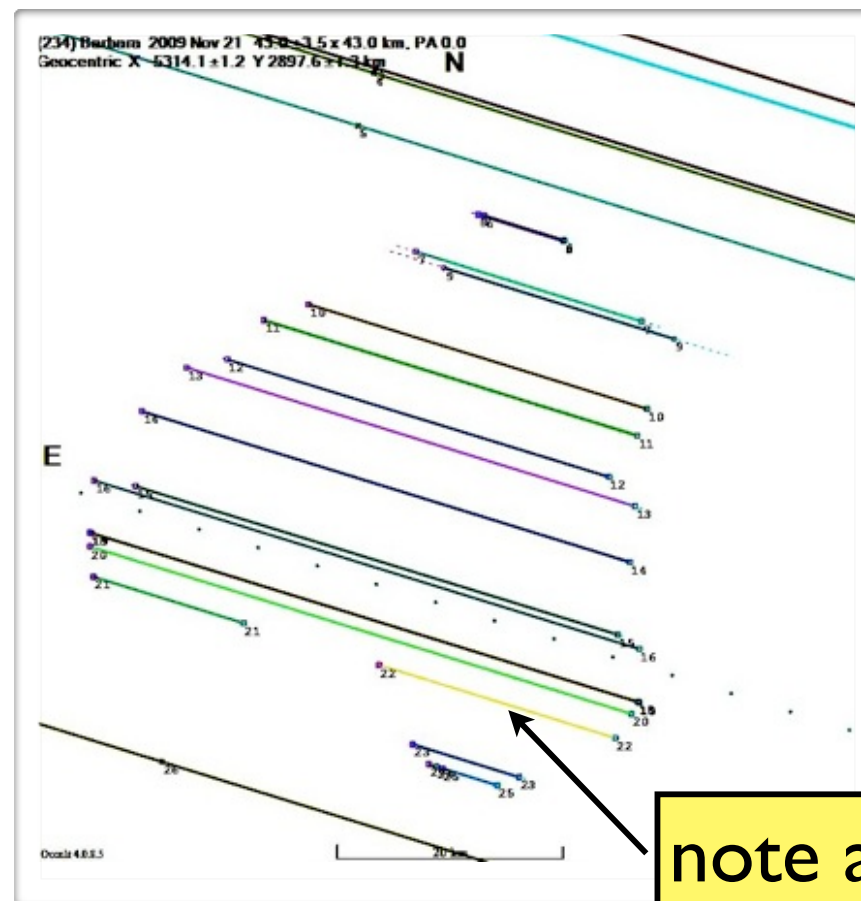
2009 occultation events



Stellar occultation 1

Oct 5, 2009
Ecliptic longitude, heliocentric: 77° ;
geocentric: 103°
Phase angle: 25°

(chord n. 2 is not precisely dated)
Source: http://www.euraster.net/results/2009/20091105-Barbara-crd_temp.gif



Stellar occultation 2

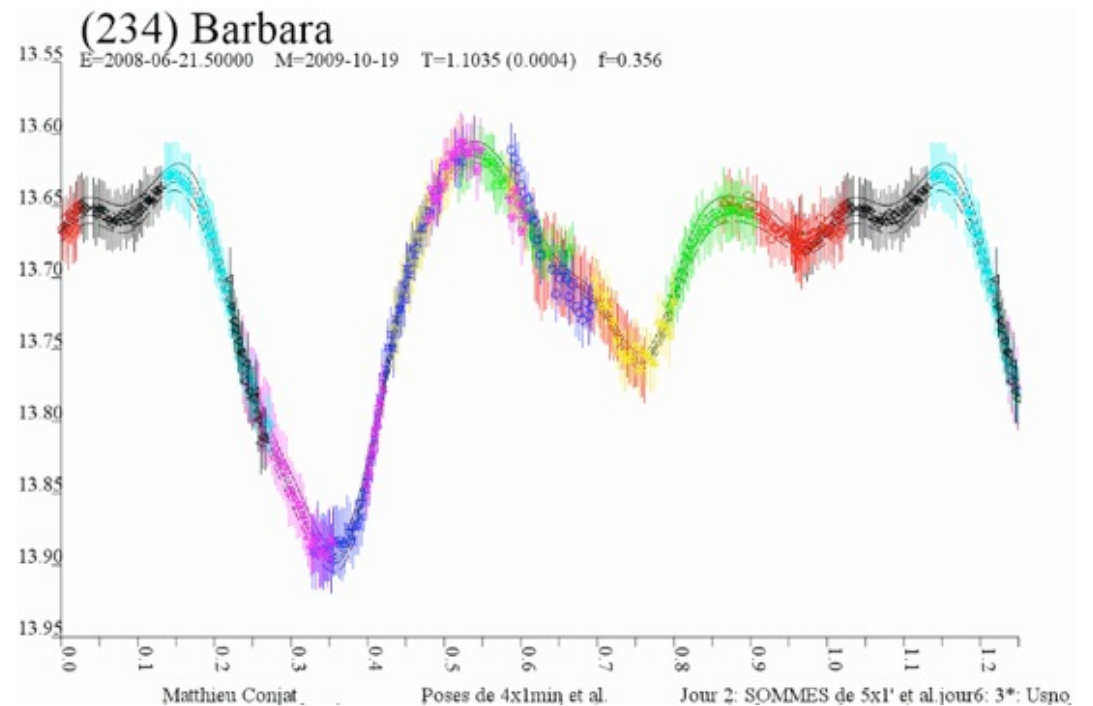
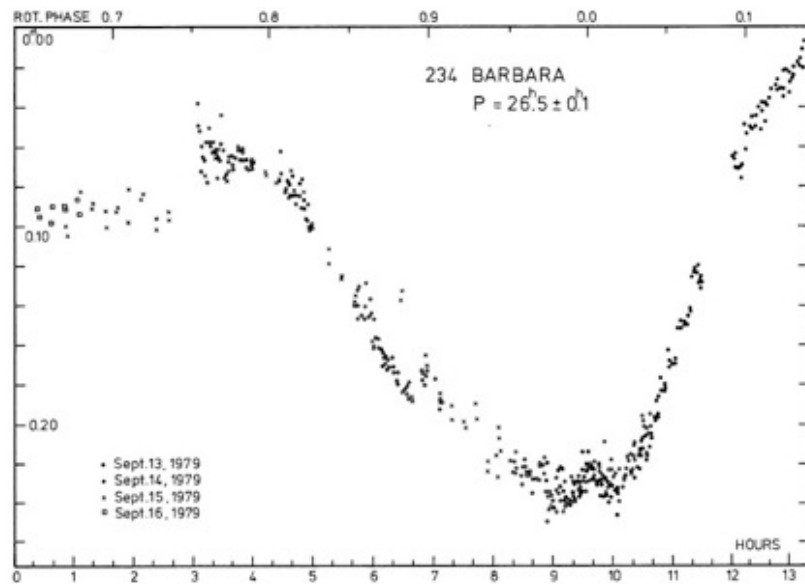
Nov 21, 2009
Ecliptic longitude, heliocentric: 89° ; geocentric: 107°
Phase angle: 18°

Source: <http://www.asteroidoccultation.com/observations/Results/>

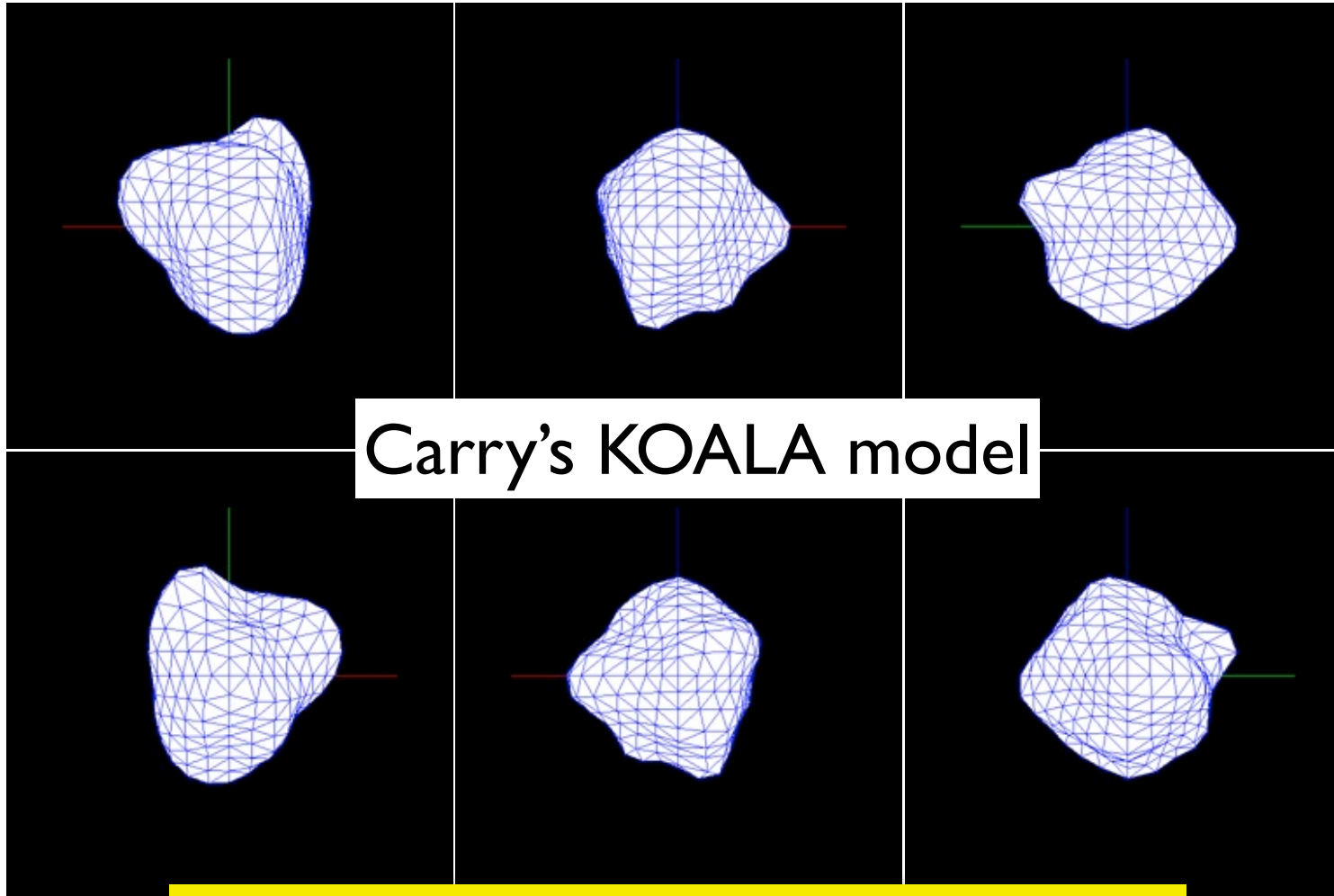
note also the
double coord

Size from the MIDI-VLTI observations confirmed

Barbara follow up: photometric lightcurves



KOALA shape model of Barbara from occultations and photometry

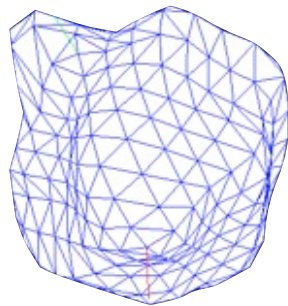


Tanga, Carry, Delbo et al, in preparation

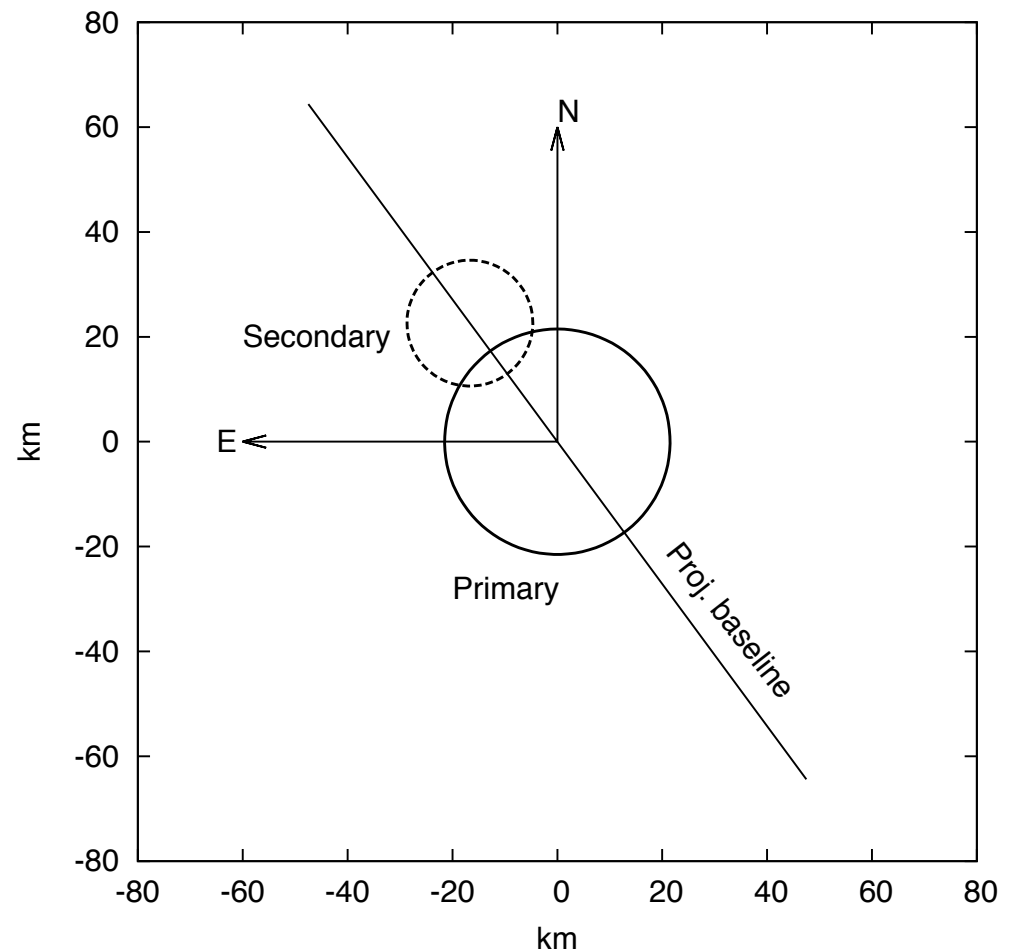
KOALA vs VLTI models

projected on the sky at the time of VLTI observations

KOALA model
from Tanga et al.



VLTI model
adapted from Delbo et al. 2009

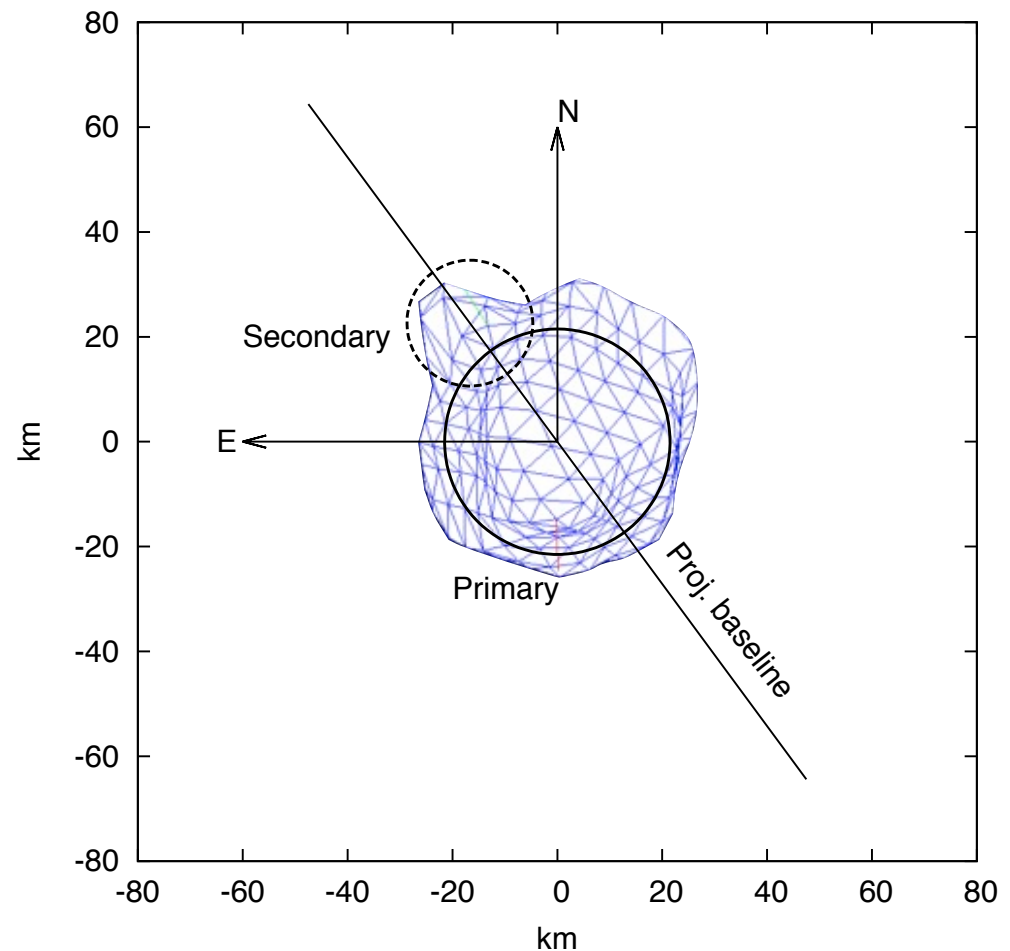


KOALA vs VLTI models

projected on the sky at the time of VLTI observations

KOALA model
from Tanga et al.

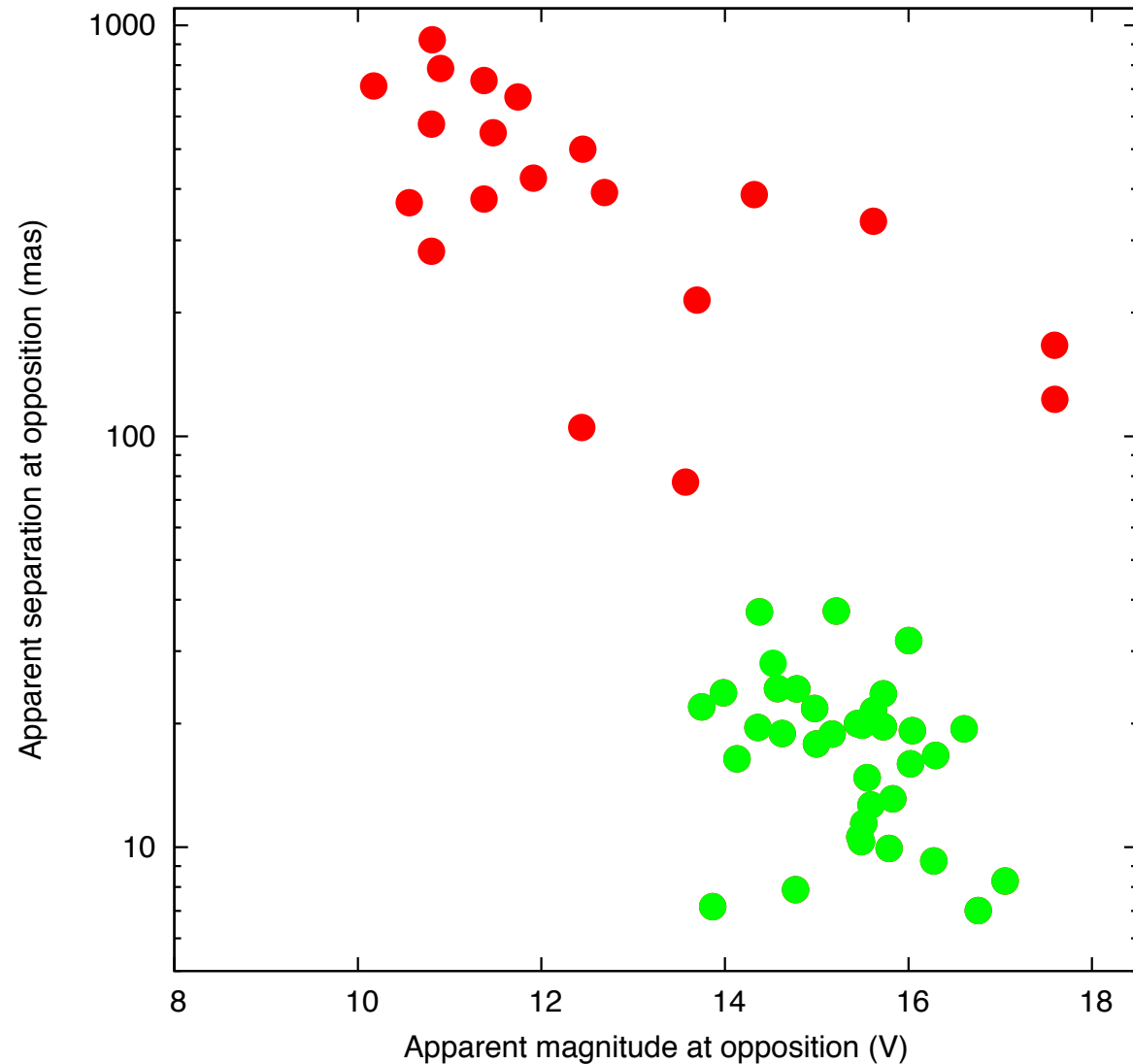
VLTI model
adapted from Delbo et al. 2009



Future projects

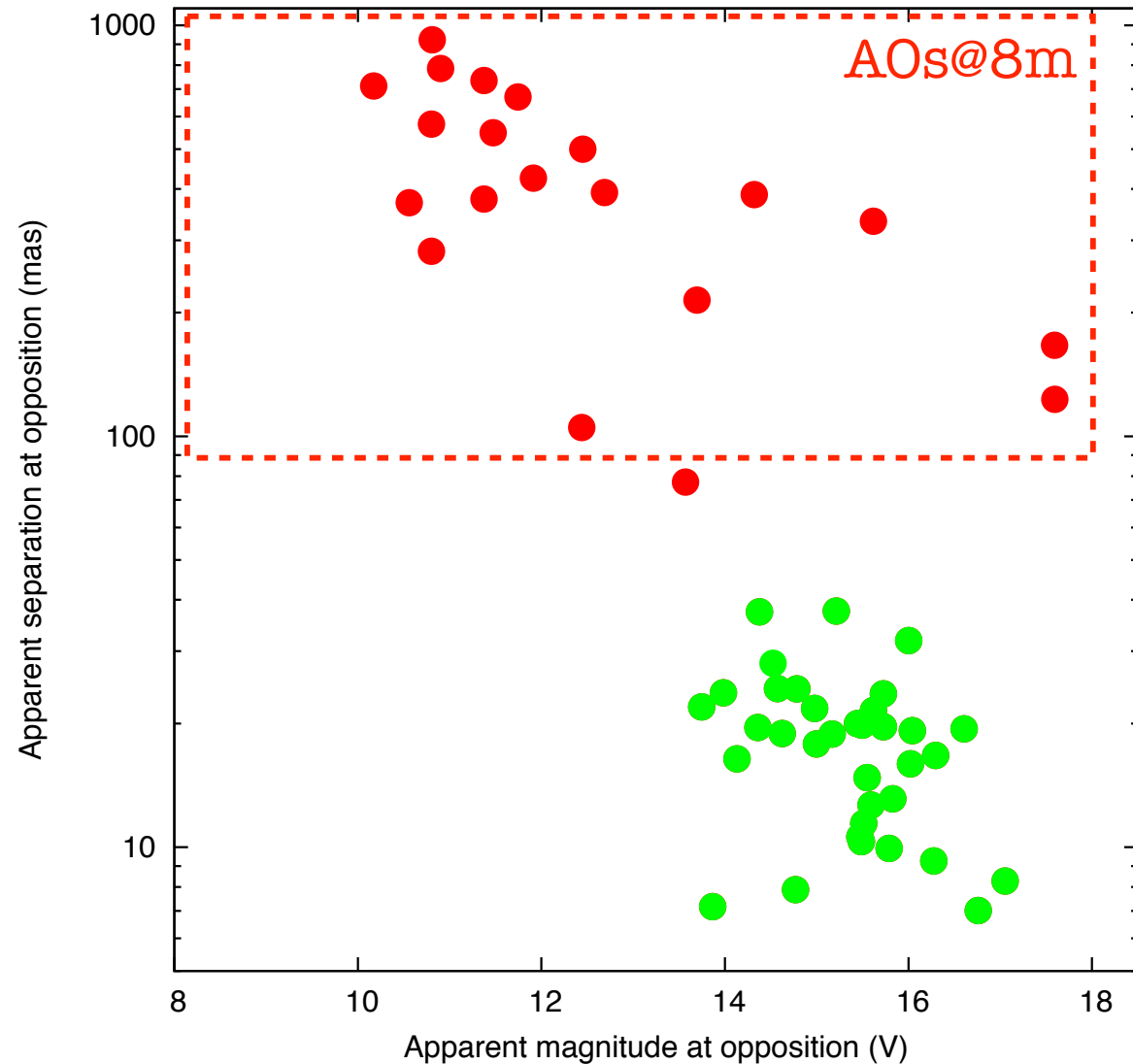
Asteroids with satellites

- discovered by AOs
- discovered by photometry: transits and eclipses



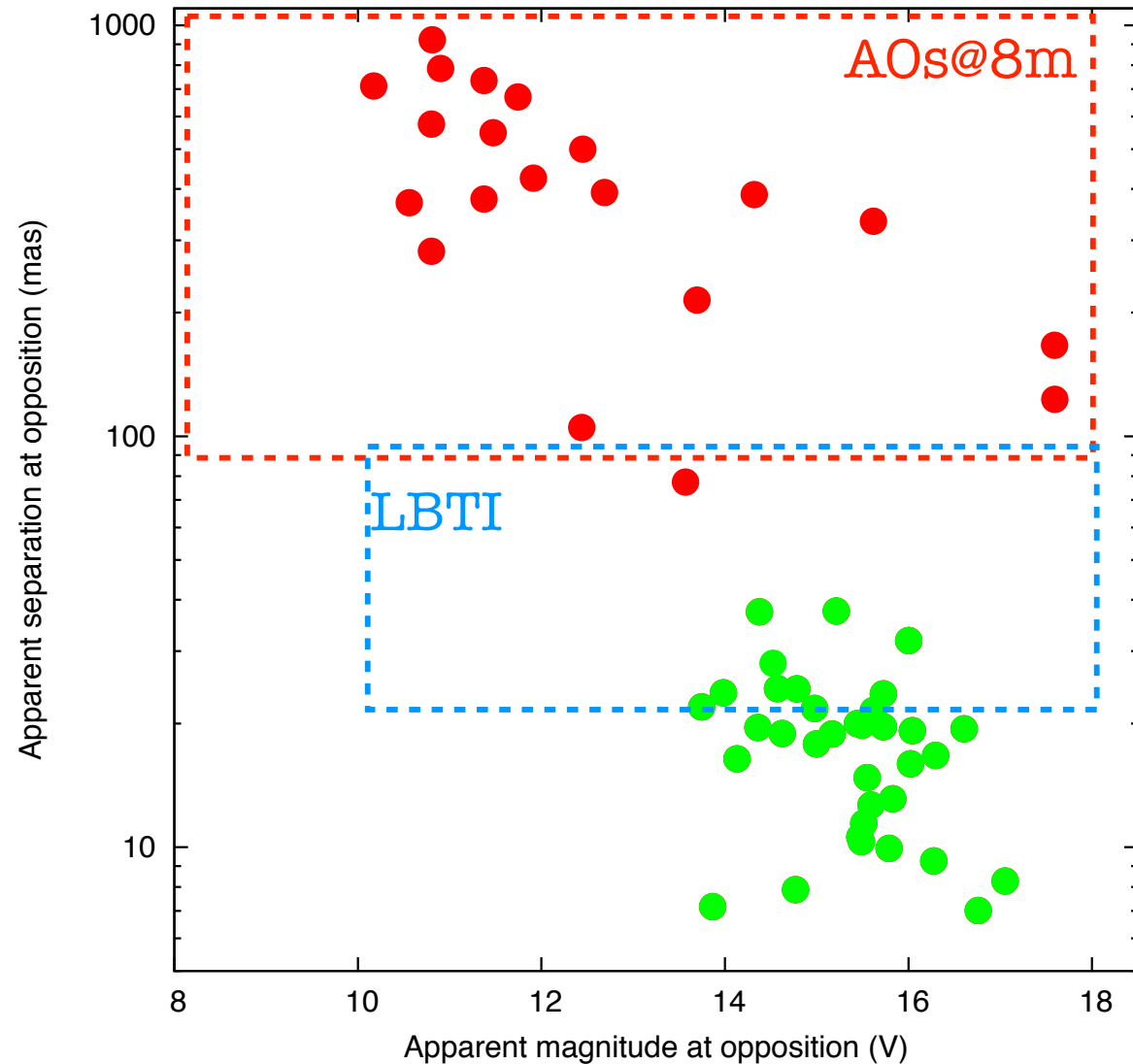
Asteroids with satellites

- discovered by AOs
- discovered by photometry: transits and eclipses



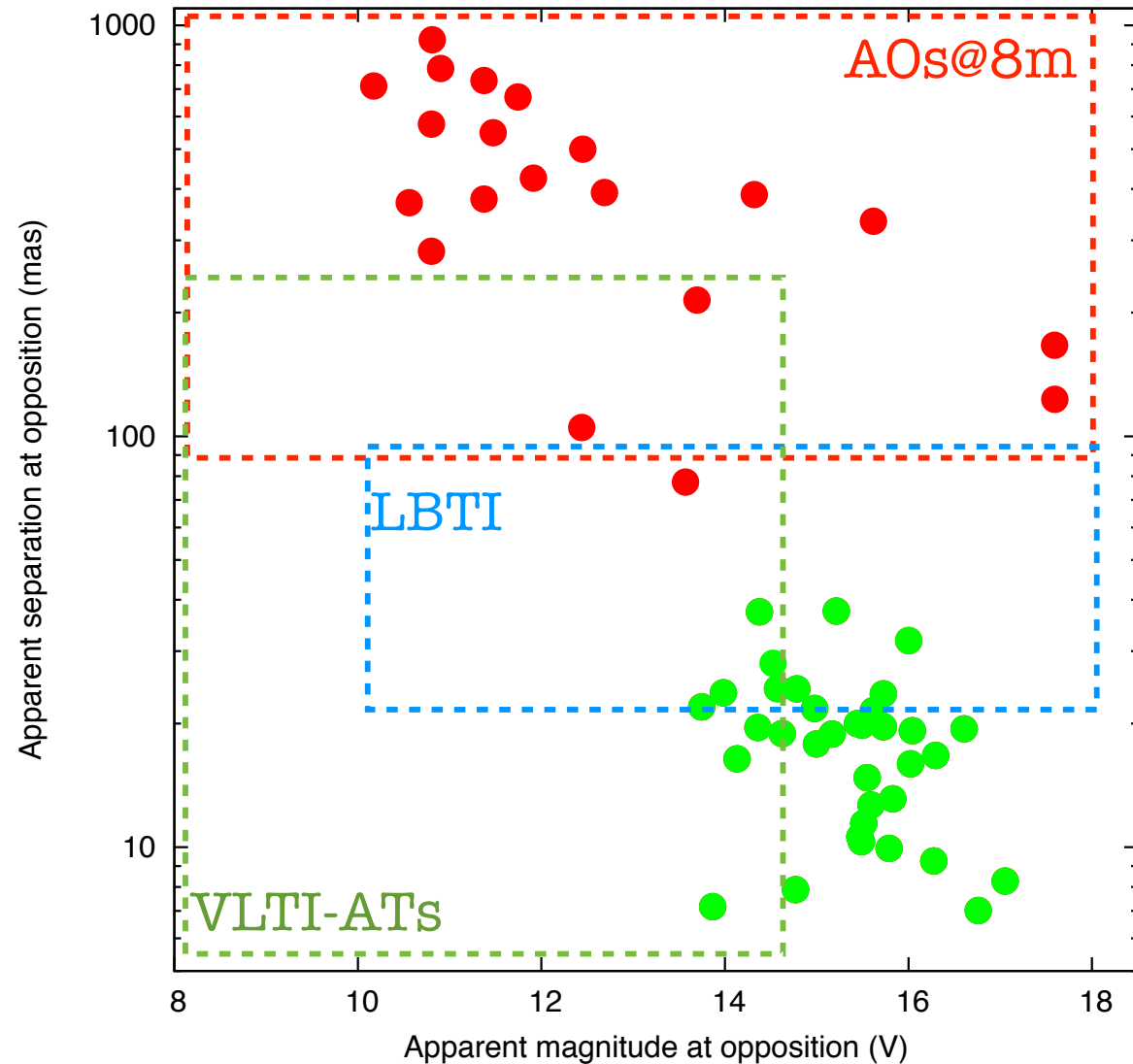
Asteroids with satellites

- discovered by AOs
- discovered by photometry: transits and eclipses



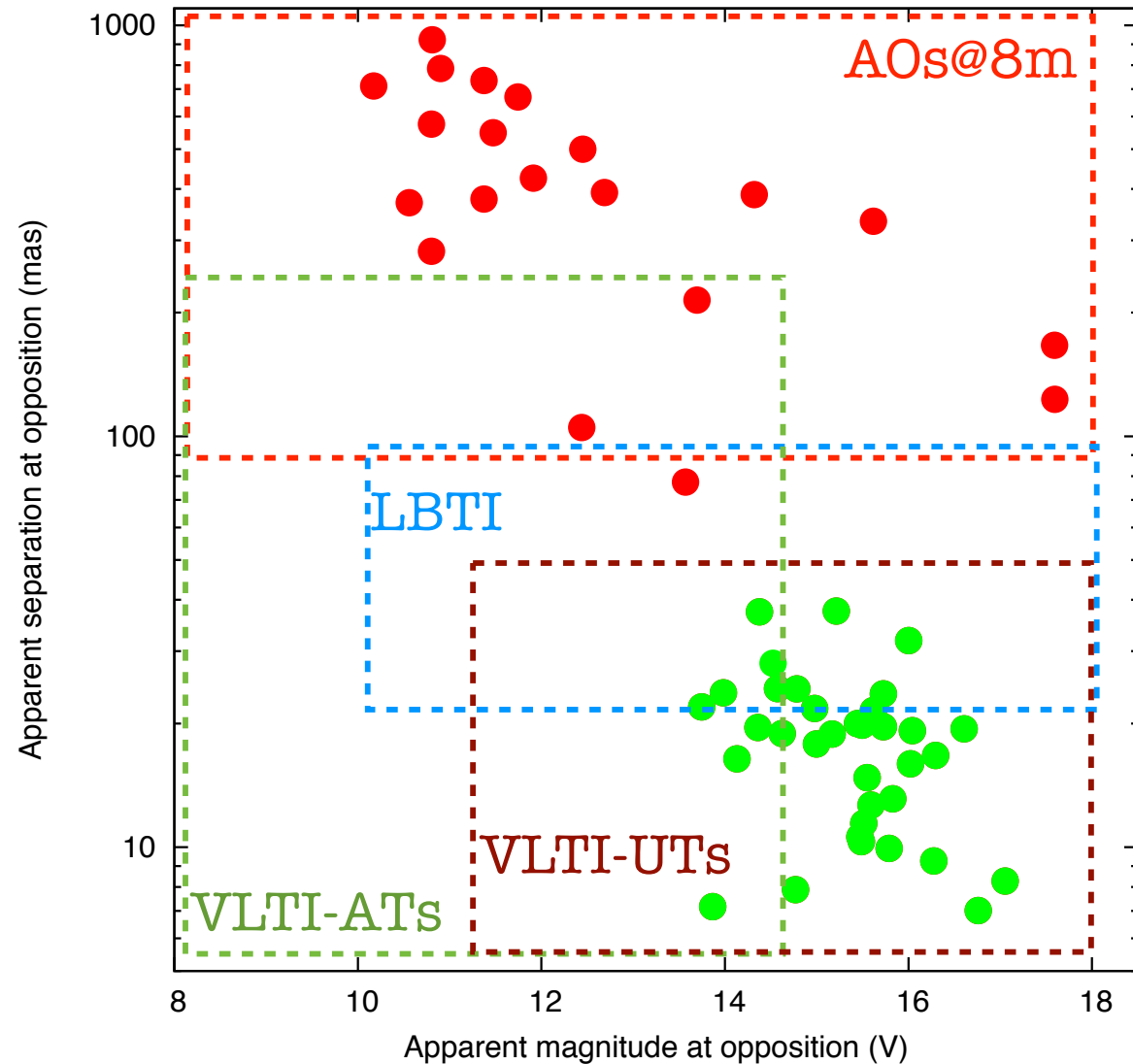
Asteroids with satellites

- discovered by AOs
- discovered by photometry: transits and eclipses

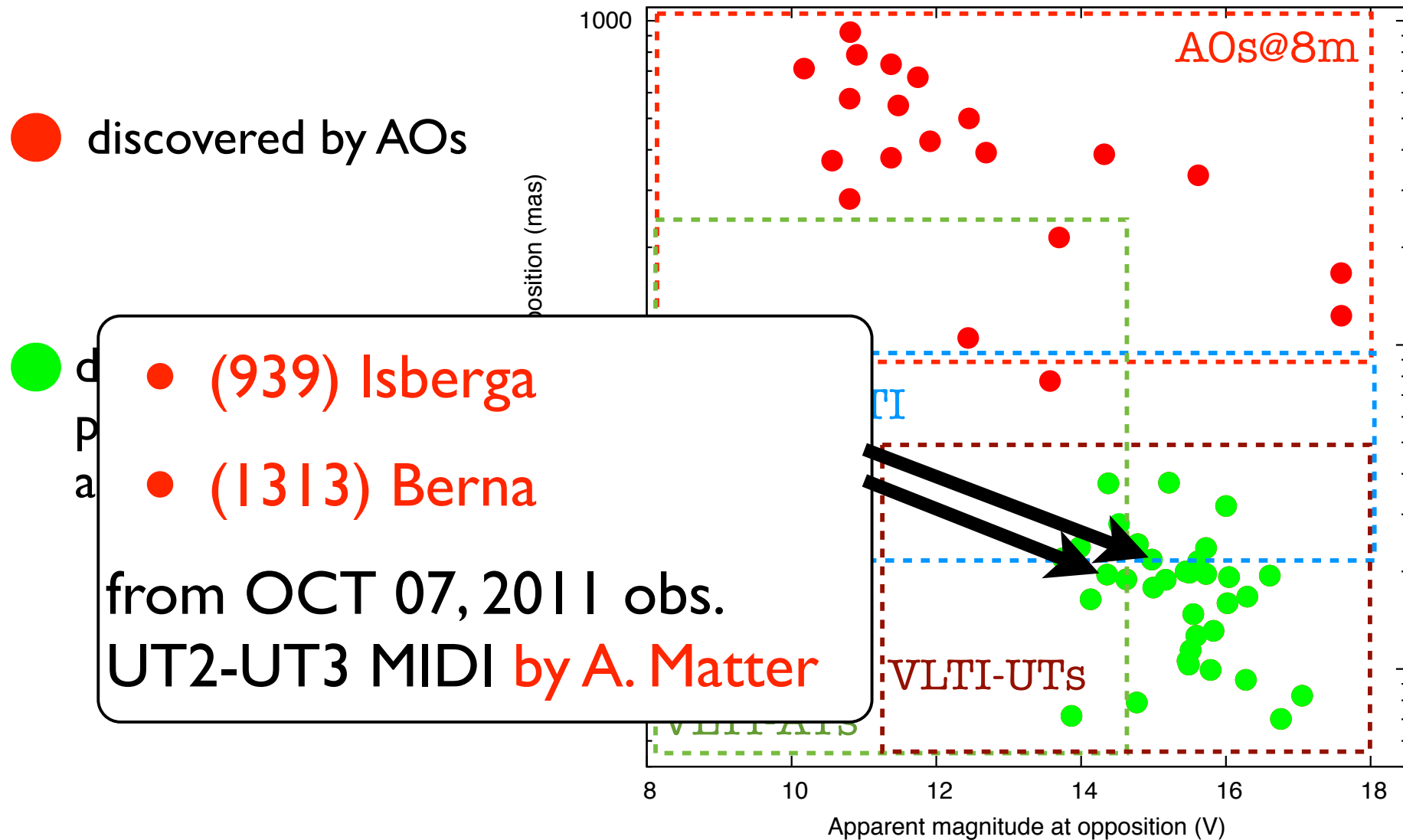


Asteroids with satellites

- discovered by AOs
- discovered by photometry: transits and eclipses



Asteroids with satellites



1. Title
Splitting photometric binary asteroids by interferometry

Category: **C-8**

3. Run	Period	Instrument	Time	Month	Moon	Seeing	Sky	Mode	Type
A	88	MIDI	1n	oct	n	n	THN	v	

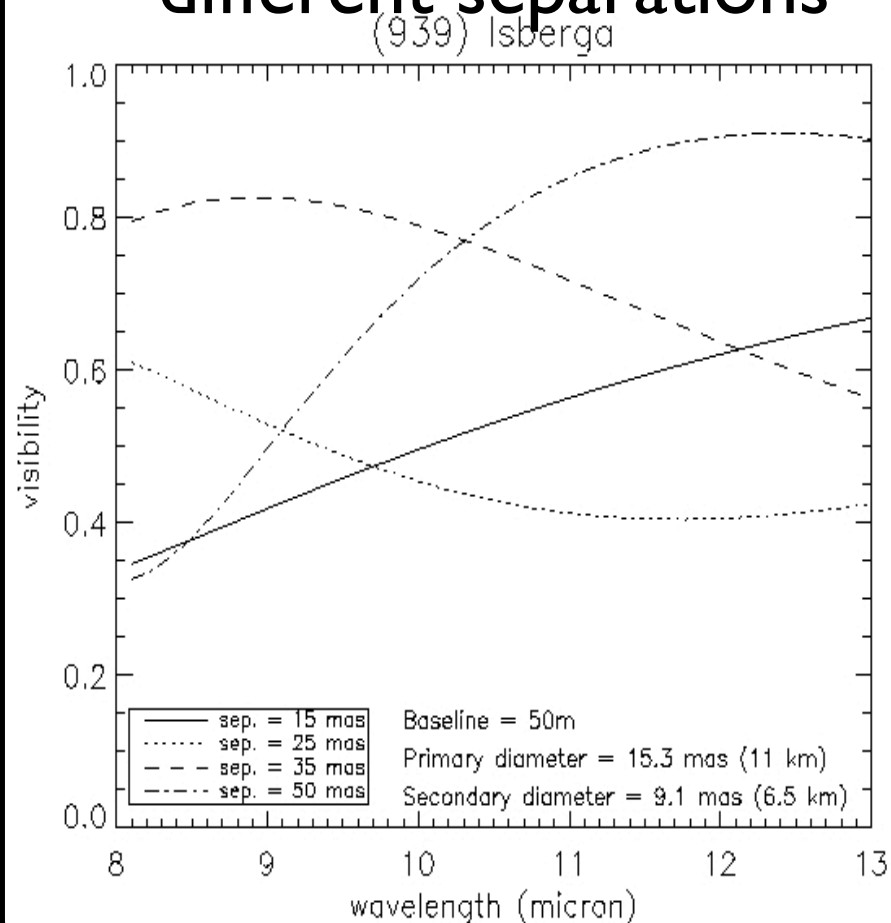
6. Principal Investigator: **BCARRY**

6a. Co-investigators:

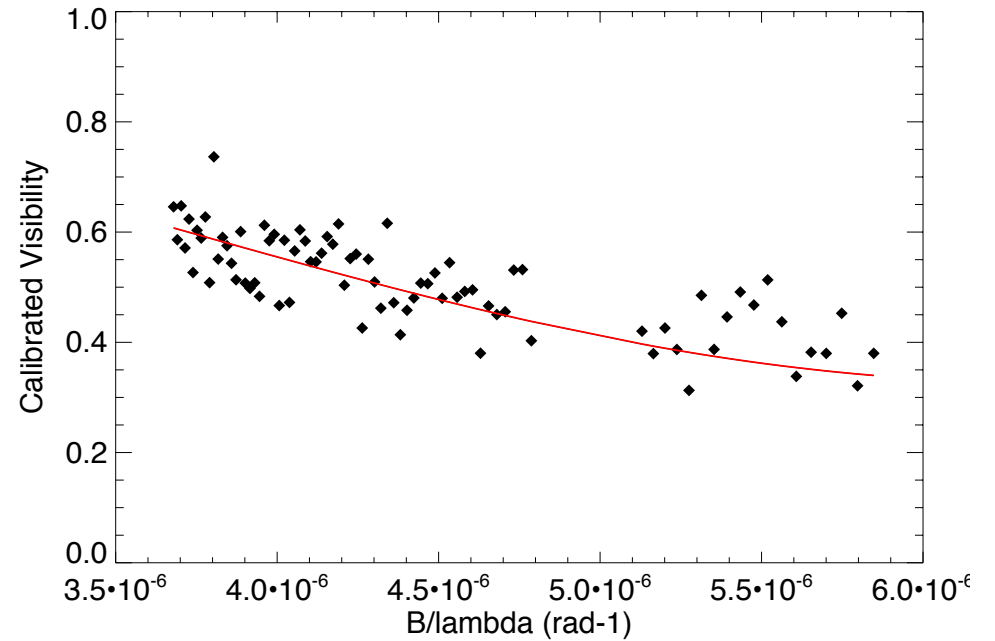
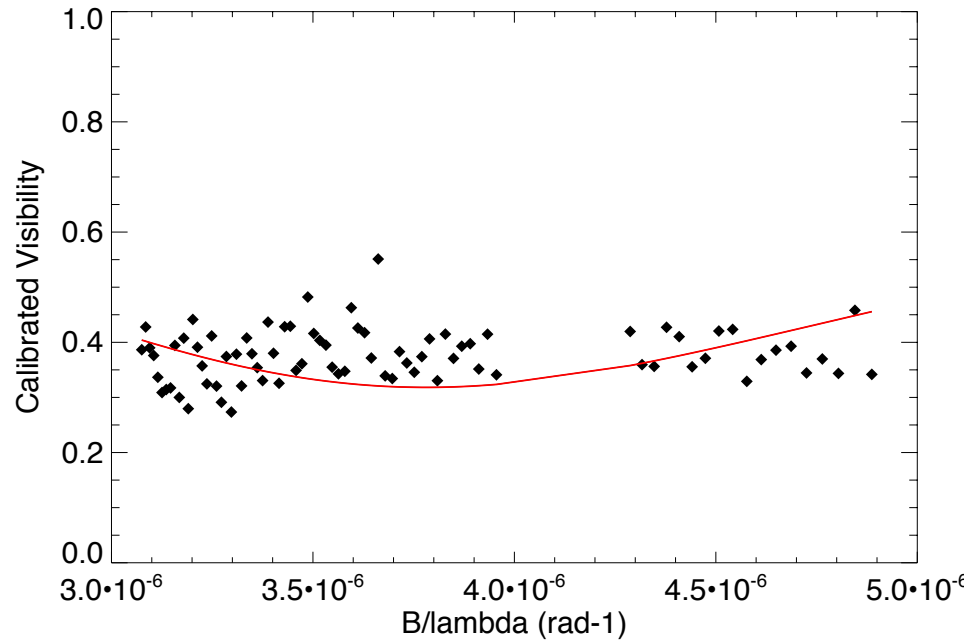
M.	Delbo	1591
W.	Merline	1694
A.	Matter	1591
P.	Tanga	1591
G.	van Belle	1258

Observations, data
reduction, modeling

Model of the visibility for different separations

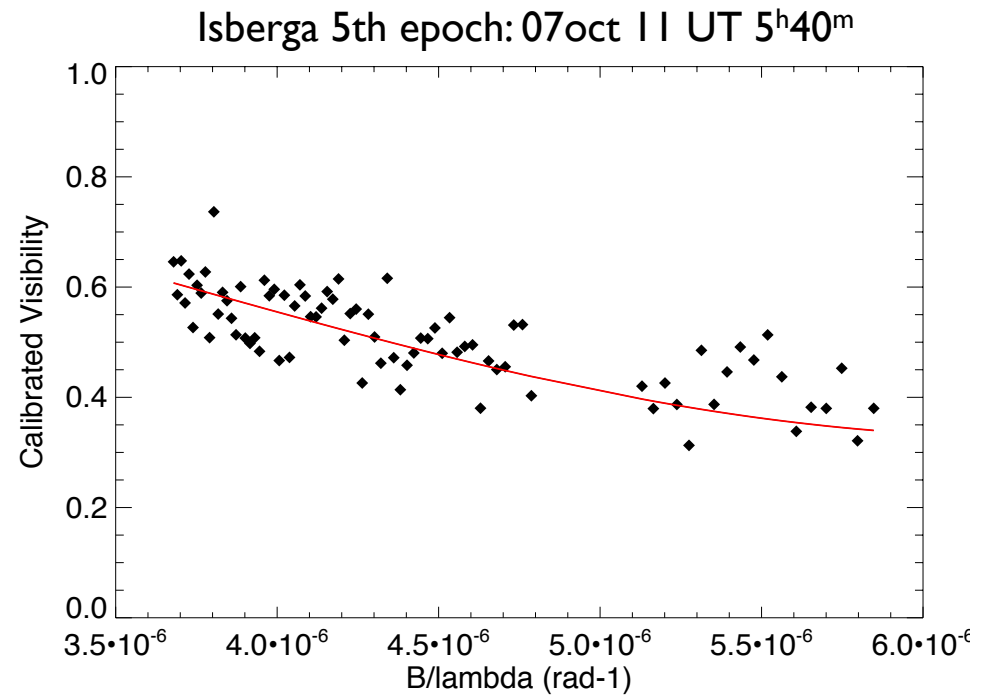
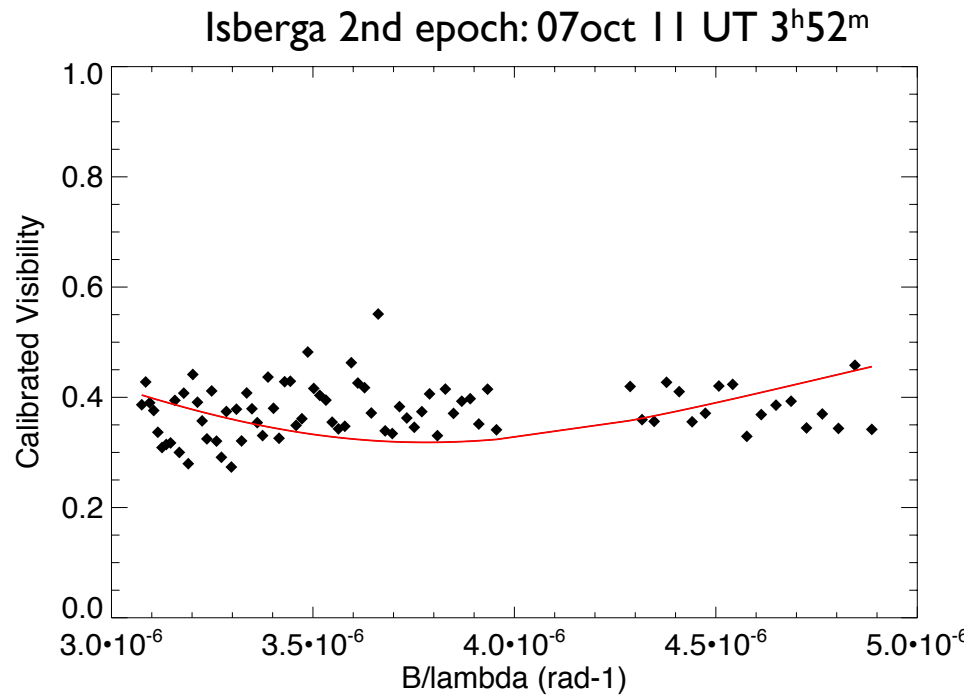


Best fit binary model



epoch	θ_1	θ_2	ρ	D_1	D_2	d
UT	mas	mas	mas	km	km	km
2 nd epoch: 3 ^h 52 ^m	13 ± 0.5	20 ± 0.3	28 ± 0.7	9 ± 0.3	14 ± 0.2	19 ± 0.5
5 th epoch: 5 ^h 40 ^m	10 ± 1	18 ± 2	19 ± 3	7 ± 0.7	13 ± 1	13 ± 2

Best fit binary model

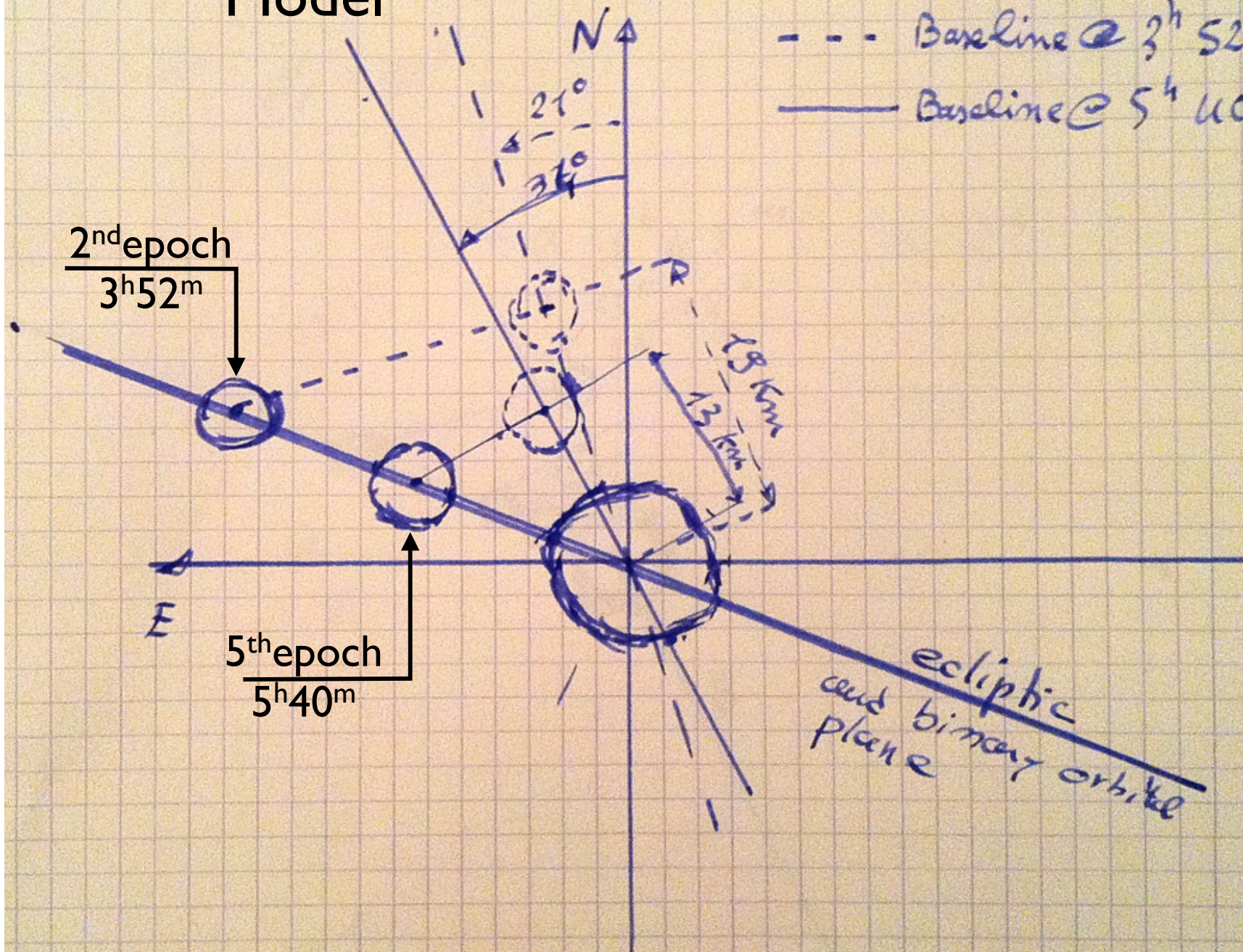


epoch UT	θ_1 mas	θ_2 mas	ρ mas	D_1 km	D_2 km	d km
2 nd epoch: 3 ^h 52 ^m	13±0.5	20±0.3	28±0.7	9±0.3	14±0.2	19±0.5
5 th epoch: 5 ^h 40 ^m	10±1	18±2	19±3	7±0.7	13±1	13±2

Very Preliminary Model

Observations 07 OCT 2011
UT

--- Baseline @ 3^h 52^m
— Baseline @ 5^h 40^m



Bibliography I



William F Bottke, Daniel D Durda, David Nesvorný, Robert Jedicke, Alessandro Morbidelli, David Vokrouhlický, and Hal Levison.

The fossilized size distribution of the main asteroid belt.

Icarus, 175:111, May 2005.



RP Binzel, A Morbidelli, S Merouane, FE DeMeo, M Birlan, P Vernazza, CA Thomas, AS Rivkin, SJ Bus, and AT Tokunaga.

Earth encounters as the origin of fresh surfaces on near-earth asteroids.

Nature, 463(7279):331–334, 2010.



F DeMeo, R Binzel, S Slivan, and S Bus.

An extension of the bus asteroid taxonomy into the near-infrared.

Icarus, Jan 2009.

Bibliography II



Marco Delbo', Aldo Dell'Oro, Alan W Harris, Stefano Mottola, and Michael Mueller.

Thermal inertia of near-earth asteroids and implications for the magnitude of the yarkovsky effect.

Icarus, 190:236, Sep 2007.

Elsevier Inc.



Marco Delbo'.

The nature of near-earth asteroids from the study of their thermal infrared emission.

PhD thesis - Freie Univesitaet Berlin, pages 1–210, Jun 2004.



Marco Delbó and Alan W Harris.

Physical properties of near-earth asteroids from thermal infrared observations and thermal modeling.

Meteoritics & Planetary Science, 37:1929, Dec 2002.

Bibliography III



Karri Muinonen, Irina N Belskaya, Alberto Cellino, Marco Delbò, Anny-Chantal Levasseur-Regourd, Antti Penttilä, and Edward F Tedesco.

A three-parameter magnitude phase function for asteroids.
Icarus, 209:542, Oct 2010.



S Opeil, S Consolmagno, and D Britt.

The thermal conductivity of meteorites: New measurements and analysis.
Icarus, Jan 2010.



J. R Spencer, L. A Lebofsky, and M. V Sykes.

Systematic biases in radiometric diameter determinations.
Icarus (ISSN 0019-1035), 78:337, Apr 1989.

Bibliography IV



Edward F Tedesco, Paul V Noah, Meg Noah, and Stephan D Price.

The supplemental iras minor planet survey.

The Astronomical Journal, 123:1056, Feb 2002.



C. A Thomas, D. E Trilling, J. P Emery, M Mueller, J. L Hora, L. A. M Benner, B Bhattacharya, W. F Bottke, S Chesley, M Delbó, G Fazio, A. W Harris, A Mainzer, M Mommert, A Morbidelli, B Penprase, H. A Smith, T. B Spahr, and J. A Stansberry.

Exploreneos. v. average albedo by taxonomic complex in the near-earth asteroid population.

The Astronomical Journal, 142:85, Sep 2011.



A. J Wesselink.

Heat conductivity and nature of the lunar surface material.

Bull. Astron. Inst. Neth., 10:351, Apr 1948.

Bibliography V



JR Zimbelman.

The role of porosity in thermal inertia variations on basaltic lavas.

Icarus, 68(2):366–369, 1986.